OAK RIDGE NATIONAL LABORATORY
operated by
UNION CARBIDE CORPORATION
NUCLEAR DIVISION
for the
U.S. ATOMIC ENERGY COMMISSION

ORNL - TM - 1570

1

FUELS AND MATERIALS DEVELOPMENT PROGRAM QUARTERLY PROGRESS REPORT FOR PERIOD ENDING JUNE 30, 1966

LEGAL NOTICE

ORNL-TM-1570

Contract No. W-7405-eng-26

FUELS AND MATERIALS DEVELOPMENT PROGRAM QUARTERLY PROGRESS REPORT FOR PERIOD ENDING JUNE 30, 1966

Compiled by

P. Patriarca

SEPTEMBER 1966

OAK RIDGE NATIONAL LABORATORY
Oak Ridge, Tennessee
operated by
UNION CARBIDE CORPORATION
for the
U.S. ATOMIC ENERGY COMMISSION

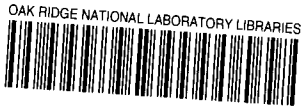

FOREWORD

This is the ninth quarterly progress report describing work performed at the Oak Ridge National Laboratory for the Fuels and Materials Branch, Division of Reactor Development and Technology, U.S. Atomic Energy Commission. A new program, Sintered Aluminum Products, was started during the past year and its progress is summarized in this report. The specific programs covered are as follows:

Part I. Metals and Ceramics Division

Program Title	Person in Charge	Principal Investigator(s)
Controlled Precipitation in Nuclear Materials	P. Patriarca W. O. Harms	J. L. Scott J. P. Hammond
Fuel Element Development	G. M. Adamson, Jr.	C. F. Leitten, Jr.
Mechanical Properties	C. J. McHargue D. A. Douglas, Jr.	J. R. Weir
Nondestructive Test Development	W. O. Harms D. A. Douglas, Jr.	R. W. McClung
Zirconium Metallurgy	C. J. McHargue	M. L. Picklesimer
Sintered Aluminum Products	G. M. Adamson, Jr. D. A. Douglas, Jr.	C. F. Leitten, Jr. D. G. Harman

Part II. Reactor Chemistry Division

Fission-Gas Release and Physical Properties of Fuel Materials During Irradiation	O. Sisman	R. M. Carroll J. G. Morgan

TABLE OF CONTENTS

SUMMARY

1. Controlled Precipitation in Nuclear Materials

We are studying controlled precipitation in UN as a possible way to improve its irradiation behavior. Both precipitation out of solid solution and internal oxidation techniques look promising. Of the systems studied to date. 0.1 wt % Mo in UN is preferred for precipitation out of supersaturated solid solution by controlled heat treatment. The internal oxidation of (U,Th)N by UO_2 also looks attractive.

2. Fuel Element Development

In the last quarter, it was shown that several thoria pellets could be coated simultaneously with UO_2 by direct conversion of UF_6. Fabrication of irradiation specimens from solid and powder products was not possible due to difficulties in obtaining materials. Additional experiments in adding nitrogen during reduction of UF_6 by lithium vapor show that uranium nitride may be obtained from the reaction. Thermodynamic calculations show that the conversion pf PuF_6 to PuO_2 should behave similarly to the conversion of UF_6 to UO_2; therefore, we have assembled the necessary experimental apparatus in alpha enclosures to demonstrate feasibility.

Scale-up of the coreduction of tungsten and rhenium hexafluorides by hydrogen to produce tungsten rhenium alloys for mechanical properties evaluation is under way.

We have obtained results from high-temperature high-burnup irradiation information on U_3O_8 and UO_2 dispersions in aluminum that indicate satisfactory performance.

3. Mechanical Properties

We have continued to investigate the elevated-temperature radiation-induced embrittlement of stainless steels. Our objectives in this part of the program are to determine the mechanism for the damage and to attempt to alleviate the problem by metallurgical treatment of the

alloys prior to irradiation. Another aspect of our program concerns the pronounced damage that occurs in stainless steels upon irradiation at temperatures around 200°C.

Postirradiation creep-rupture tests at 650°C of type 304 stainless steel given various heat treatments prior to irradiation are under way. The results show that both fine-grained and coarse-grained and aged structures produce significantly higher ductility than a coarse-grained structure. The properties of the coarse-grained and aged material are also superior from the strength viewpoint because the rupture life in addition to the ductility appears improved.

A temperature-controlled irradiation was conducted on stainless steel tensile and electron microscopy samples over the temperature range from 90 to 450°C. The results indicate that the structure produced by irradiation between 90 and 300°C consists of small black dots that have the characteristics of strain fields. The approximate size of these are 50 A at the lower temperatures and 200 A at the higher temperatures. The postirradiation yield stress is highest when the dots are approximately 200 A in diameter. At temperatures above 300°C a rapid coarsening of the structure occurs and the yield stress falls rapidly with increasing temperature.

4. Nondestructive Test Development

We are developing new techniques and equipment for the nondestructive evaluation of materials and components. The major emphasis has been on eddy-current, ultrasonic, and penetrating-radiation methods.

We have constructed a family of eddy-current coils and made a series of impedance measurements as a function of frequency and coil-to-specimen spacing. The agreement with calculated data is quite good. Improvements to the phase-sensitive eddy-current instrument now allow a greater range of sensitivity and lift-off compensation. A new portable phase-sensitive instrument has been constructed to operate at two frequencies.

In ultrasonics we have improved the replication techniques for accurate measurement of reference notches. The versatility of the

Schlieren system has been increased to allow observation of ultrasonic energy in transparent solids using polarized light.

In penetrating radiation we have achieved significant improvement in transmitting energy from a scintillation crystal to a photomultiplier tube by using a fiber optic light pipe.

5. Zirconium Metallurgy

Equipment has been built for placing a grid of oxide lines on the test sections of the Zircaloy-2 tubing being used in the study of biaxial stress behavior of highly textured anisotropic materials. The 200- to 300-A-thick oxide lines are produced by anodizing at low voltages through exposed and developed photoresist films. This will allow examination of the development and the uniformity of the strain pattern of the specimen during the test. Grain size measurements made on each of three surfaces of each of the six lots of Zircaloy tubing being used in the study have shown that in each case the grains are equiaxed and of essentially the same size but the size varies between the lots of materials. Knoop microhardness measurements have been used to determine approximately the uniaxial yield strengths in tension and compression in the tubing material. The yield strengths so predicted are in good agreement with those estimated from a knowledge of the texture present in each and the yield strengths of those textures as observed in sheet and plate material.

The procedure previously reported for characterizing the three-dimensional anisotropy of yield and flow in Zircaloy-2 from a single uniaxial test has been simplified to some extent by the development of an empirical equation relating the strain anisotropy constants in tension to those in compression along the same stress axis. Thus, these values can now be calculated rather than having to be obtained from a graph.

An approximate determination has been made of the orientation of the basal pole of zirconium grains, heavily deformed by shear, relative to the shear plane and shear direction. At large amounts of shear, the starting texture of the polycrystalline specimens relative to the

shear geometry had no effect on the final orientation of the grains deformed by shear.

The anisotropy of oxidation of single-crystal spheres of zirconium and hafnium has been examined in 500°C steam at 1 atm pressure. Both show essentially the same patterns of anisotropy as those reported previously for oxidation in air at 360°C. The oxidation of hafnium is considerably slower than that of zirconium under the same conditions.

Pustules have been observed to form over or on the thin uniform films of oxide on zirconium in steam, as has been reported by Wanklyn. The pustules have a regular external habit which is a function of the crystallographic orientation of the underlying metal. The shape varies from hexagonal columns near the basal pole, to square near $\{11\bar{2}0\}$, to trapezoidal to kidney-shaped in between. Pustule formation was also observed to occur where hydrides had been located in polycrystalline zirconium hydrided to 1000 ppm H_2 and oxidized in 500°C steam.

The oxidation behavior of zone-refined high-purity zirconium strips in steam at 500°C was compared to the behavior of the crystal-bar starting stock. The high-purity strips showed white oxide (indicating poor corrosion resistance) present under the same conditions where the starting stock showed the blue-black "protective" oxide film.

6. Sintered Aluminum Products Development

A program has been undertaken at ORNL directed toward developing processes, and, ultimately, specifications for the fabrication of aluminum-oxide-strengthened wrought aluminum products. Sintered aluminum products containing 2 to 10% oxide as a fine dispersion retain strength at high temperatures, thus making them attractive for 450°C service as pressure tubes and fuel cladding in organic-cooled or desalination reactors.

We have approached the problem by thoroughly characterizing commercially available aluminum powder products and studying means for specific oxide additions. Fabrication and testing of the materials thus developed have shown that in comparison to previously available

commercially sintered aluminum materials significant improvement of homogeneity and uniform strength properties may be attained.

Characterization of various forms of aluminum powder has revealed that use of metal flakes within a controlled size range produces a stronger and more homogeneous final product. The oxide morphology can be controlled and agglomeration prevented by vacuum treating at 600°C. A process flowsheet has been developed, and process variables are being investigated at each important step.

Electron microscopy studies indicate that strengthening in sintered aluminum products is not related to stabilization of a cold-worked structure at high temperatures. The as-milled flake is completely recrystallized with a very low dislocation density. Hot working of SAP compacts significantly improves the rupture strength of the material. Nondestructive quality control techniques are under investigation to monitor the product at selected stages of fabrication. Fractograph studies have revealed that sintered aluminum products fail in a ductile manner at low strain rates above 400°C, even though total uniform elongation is less than 0.5%.

7. Fission-Gas Release and Physical Properties of Fuel Materials During Irradiation

A hollow-cylinder specimen of single-crystal UO_2 is being irradiated for the purpose of measuring thermal conductivity and fission-gas release during irradiation. In these experiments the specimen is oscillated sinusoidally in the reactor so as to oscillate the neutron flux and thus oscillate the fission rate in the specimen in a sinusoidal manner. The specimen temperature, measured by axial thermocouples, will also oscillate in response to the changing fission power. The base specimen temperature can be controlled by air-cooling the outside of the specimen capsule.

The response of the specimen temperature will not be instantaneous with change of fission power, but will have a time lag depending on the specific heat, thermal conductivity, and emissivity of the specimen. The amplitude of the temperature oscillations will depend upon the amplitude of the fission-rate oscillations and the frequency of the

oscillations. From measurements of phase shift and temperature amplitude as a function of frequency and amplitude of fission-rate oscillations, the thermal conductivity of the specimen can be calculated. By changing the axis of fission-rate oscillations and the air-cooling rate, the change of thermal conductivity as a function of fission rate and temperature can be measured.

An inconclusive attempt was made to measure the effect of electrical fields on fission-gas migration, but some mysterious and unexpected feedback results occurred that warrant further study. An experimental method was found to determine the response of thermocouples to changing temperatures and how to apply the response correction to our thermal measurements. Fission-gas waves change their appearance during the time the sweep gas requires to move them out of the reactor. We have found a method to correct for the mixing caused by the system and thus arrive at the wave form in which the fission gas was emitted.

[redacted]

PART I.

METALS AND CERAMICS DIVISION

[redacted]

1. CONTROLLED PRECIPITATION IN NUCLEAR MATERIALS

J. L. Scott J. P. Hammond

The purpose of this program is to develop means for improving the performance properties of both fissionable and nonfissionable materials by optimizing the microstructure through controlled precipitation of stable dispersed phases. Work during the present report period was limited to studies on uranium nitride fuel.

Production of Precipitates in Uranium Nitride

T. G. Godfrey J. M. Leitnaker
R. A. Potter

Finely divided precipitates offer the possibility of reducing fuel swelling in uranium nitride by providing "pinning sites" for small fission-gas bubbles. Accordingly, we are investigating methods of producing small precipitates (approx 200 A in diameter) in uranium nitride. Second-phase materials under study include tungsten, molybdenum, uranium dioxide, and thorium dioxide. An important aspect of this work is the synthesis of high-purity uranium nitride powder of closely controlled composition. Also inherent in this investigation is the study of techniques that might be used to determine the presence of fine precipitates and their effects on the properties of the nitride.

Two different methods are being investigated for production of fine precipitates. The first involves use of an additive whose solubility in UN increases with increasing temperature. One then seeks cooling rates that allow the additive to precipitate as finely-dispersed particles. This procedure is being used in the Mo, W, and UO_2 investigations.

The second approach involves internal oxidation of mixed thorium-uranium nitride to produce fine ThO_2 precipitates in (U,Th)N. We hope to obtain the proper precipitate distribution by controlling the oxidation process or by heat treatment after oxidation.

Observational Techniques

In addition to the customary techniques of optical metallography and chemical analysis, we are making extensive use of x-ray lattice parameter determinations and a growing use of the electron microscope. A computer program written by Vogel and Kempter[1] for lattice-parameter evaluation has been modified for use with the ORNL computer facilities. With the aid of this tool, we are able to calculate precise lattice parameters on uranium nitride and hence observe small changes caused by the effects of various additions. Independent readings by three persons on each of 12 different Debye-Scherrer x-ray films indicate agreement among the three of less than ±0.0002 A in the average value. This result corresponds well with the typical computed standard deviation of ±0.0001 A.

The technique of strain measurements through x-ray line broadening is being investigated. We anticipate that very small precipitates of UO_2 or ThO_2 will have some degree of coherency with the UN lattice and some lattice strain will thus occur. Measurement of this strain might yield information about the degree of coherency of the precipitates and how it changes with heat treatment and coalescence.

Electron microscopy is another key method of evaluation. Since our specimens are pressed and sintered compacts that contain 5 to 10% porosity, preparation of thin sections for transmission electron microscopy has not been possible to date. Some of our examinations have been made on replicas of fractured surfaces, but this technique is often subject to uncertainty because of artifacts that may arise during replication. Therefore, we are attempting variation in techniques, such as fracturing the sample under a liquid that is subsequently removed in the vacuum prior to shadowing and replicating.

Additional techniques being considered are room-temperature and hot-hardness measurements and high-temperature compressive creep.

---

[1]R. E. Vogel and C. P. Kempter, Acta Cryst. 14, 1130 (1961).

Godfrey and Hallerman[2] have shown previously that microhardness values reflect compositional variations in UN, although the relationships are not straightforward. Compressive creep may be a more meaningful test since it is essentially a test of the bulk material and is not so dependent on localized variations.

Tungsten and Molybdenum Additions

Both tungsten and molybdenum have been considered as additives to UN. Samples of UN containing approximately 10 wt % W had a major phase lattice parameter of 4.8889 ± 0.0002 A after annealing at 2300°C and furnace cooling. Samples of UN containing approximately 1 wt % Mo after a similar treatment had a lattice parameter of 4.8874 ± 0.0002 A. (The lattice parameter of our pure UN specimens has usually been 4.8890 ± 0.0002 A.) We concluded on the basis of these lattice parameter measurements that molybdenum was considerably more soluble than tungsten. In addition, since molybdenum was observed in the microstructure, it was estimated that the solubility of molybdenum in UN was less than 1 wt % under the condition of the experiment.

Tungsten was abandoned temporarily, based on these experiments, and molybdenum was examined more carefully. Samples of UN containing 0.1 wt % Mo were prepared by blending the powders, pressing, and sintering at 2300°C under 1 atm N_2 in a tungsten resistance furnace. Three sets of pellets were subsequently annealed under nitrogen in an induction furnace at 2300, 2500, and 2625°C for times from 30 to 60 min followed by a fast cooling to 1500°C at which time the nitrogen was pumped out to approximately 1×10^{-5} torr and the furnace power cut off. The observed lattice parameters, 4.8882 ± 0.0002 A, were independent of the annealing temperature, but as shown in Fig. 1.1, the 2300°C sample contained massive inclusions of molybdenum whereas the 2625°C sample contained none. Though it is not apparent in these photomicrographs, the

---

[2]T. G. Godfrey and G. Hallerman, Metals and Ceramics Div. Ann. Progr. Rept. June 30, 1965, ORNL-3870, pp. 166–68.

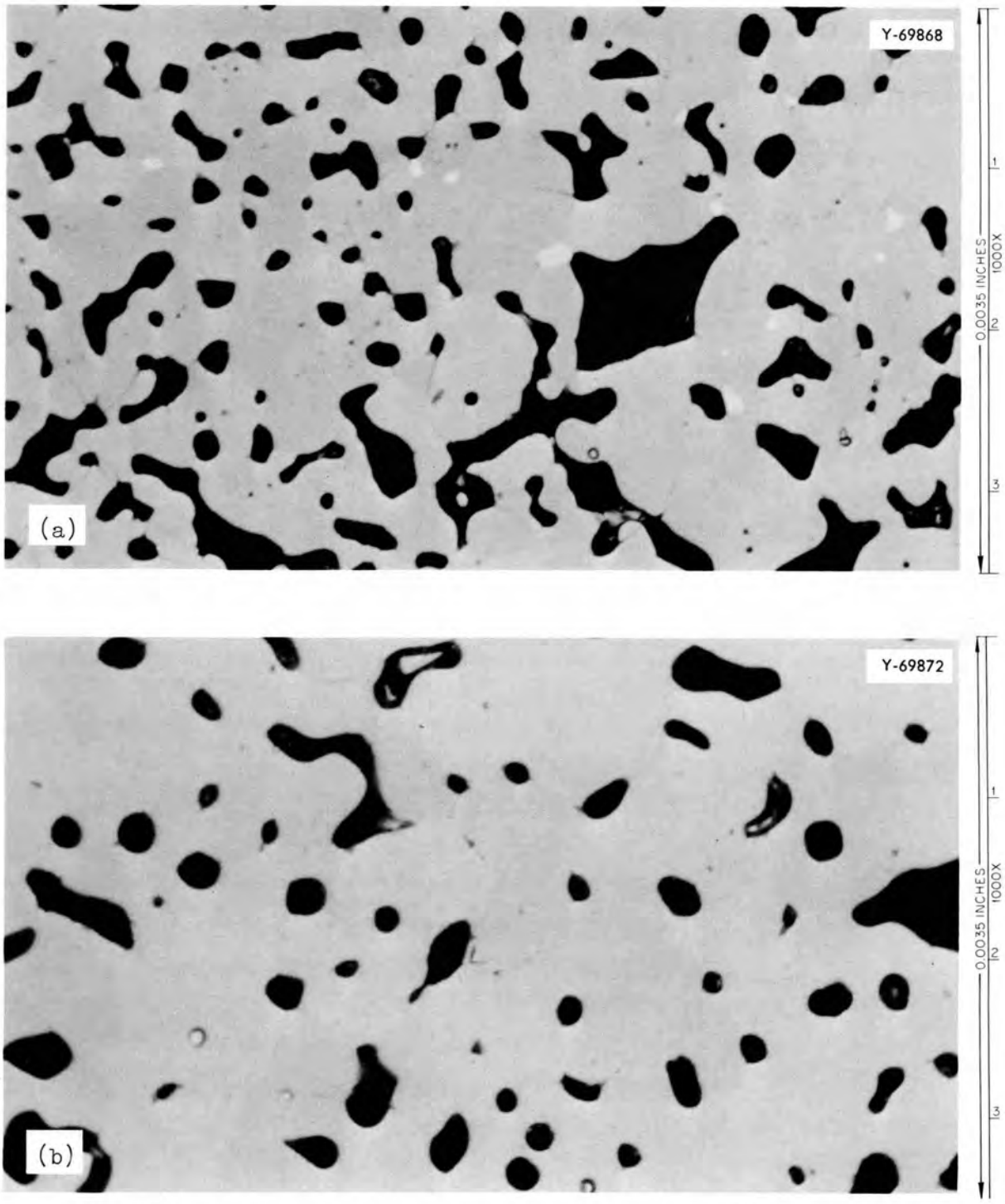

Fig. 1.1. Effect of Annealing Temperature on the Microstructure of 0.1 wt % Mo in UN. (a) After 60 min at 2300°C and (b) after 30 min at 2625°C. The matrix is UN and the angular white areas are molybdenum. Small spherical bright spots are reflections from smooth pores. As polished.

2625°C sample showed less UO_2 second phase. Chemical analysis indicated that some molybdenum may have been lost from the 2625°C sample, possibly via an oxide vaporization mechanism. However, an electron microscopy examination of a replicated fracture surface clearly showed the presence of fine precipitates in the 2625°C sample. The precipitates, as seen in Fig. 1.2a are not uniformly distributed and are rather large (approx 1000 A). Figure 1.2b illustrates the structure of a control sample with no molybdenum. From these results we conclude that the solubility of molybdenum in UN is significantly greater at 2625°C than at 2300°C, and that it readily precipitates during rapid cooling.

A second series of these 0.1 wt % Mo—UN specimens was heated at 2600°C for 30 min and subsequently annealed at 1800°C for times from 1 to 4 hr followed by rapid cooling. One specimen was similarly annealed at 1900°C for 1 hr. The lattice parameters of all specimens were again constant at 4.8882 ± 0.0002 A. Metallography showed that after 2 hr at 1800°C or 1 hr at 1900°C, molybdenum was again visible in the specimen, indicating coalescence of the fine precipitates. Also, the 1900°C anneal produced a more perfect and/or strain-free UN lattice as evidenced by the relative sharpness of the x-ray pattern.

It is apparent that more precise data will be necessary in order to fully understand the above results. The effect of oxygen impurity on the lattice parameter and on the solubility of molybdenum is unknown as are the solubility limits of molybdenum as a function of temperature. We have secured 3 kg of very pure uranium metal, and we are doping it with various levels of molybdenum through arc-melting in order to prepare homogeneous, clean material for powder synthesis and further experiments.

Thorium, Oxygen, and Carbon Additions

One of the requirements for a "successful" precipitate is that it remain dispersed at the operating temperature. Godfrey and Stiegler[3]

[3]T. G. Godfrey and J. O. Stiegler, Metals and Ceramics Div. Ann. Progr. Rept. June 30, 1965, ORNL-3870, pp. 168–69.

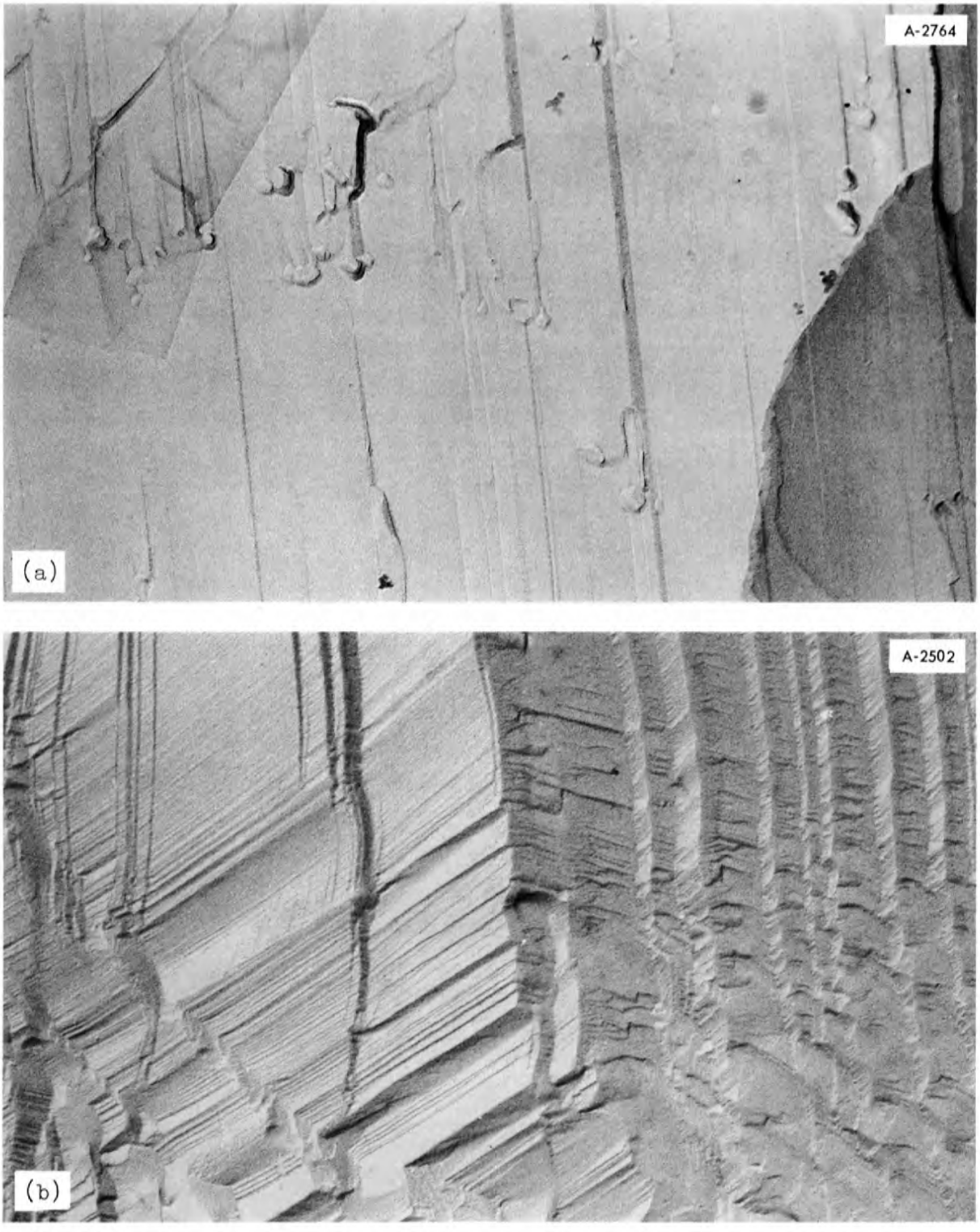

Fig. 1.2. Electron Micrograph of Replicated Fracture Surface of (a) UN–0.1 wt % Mo Annealed 30 min at 2625°C and (b) Pure UN Annealed at 2300°C. The presence of precipitates in (a) is shown by the blocky particles that decorate the fracture steps. 25,000×.

have previously discussed the formation of UO_2 precipitates in UN and developed a hypothesis to explain their presence based on solubility limits of UO_2 in UN as a function of temperature and carbon content. Since ThO_2 and UO_2 are structurally similar, we feel that the same reasoning would apply to the formation of ThO_2 precipitates in UN. Precipitates of ThO_2 should be more thermally stable since the coalescence of ThO_2 would involve simultaneous diffusion of two ion species through the UN matrix rather than only one as in the case of UO_2.

We have tried two different methods of incorporating ThO_2 in UN. The first method involved the addition of 1 wt % ThO_2 to UN powder. Specimens were prepared and sintered at 2300°C as described previously for the molybdenum specimens. They were subsequently annealed at 2300, 2500, and 2625°C for 60, 60, and 30 min, respectively. Metallographic examination revealed a small amount of oxide second phase, primarily located at grain boundaries. Lattice parameters for all specimens were 4.8915 ± 0.0003 A. A sample containing 5 wt % ThO_2, heated to 2000°C, gave the same lattice parameter.

We feel that ThO_2 reacted slightly with UN according to the reactions

$$\underline{\text{Th}} \text{ (oxide phase)} \rightleftharpoons \underline{\text{Th}} \text{ (nitride phase)} \qquad (1)$$

and

$$\underline{\text{U}} \text{ (oxide phase)} \rightleftharpoons \underline{\text{U}} \text{ (nitride phase)}. \qquad (2)$$

Assuming that the system obeys Vegard's law, we calculate from x-ray lattice parameters that approximately 0.8 mole % ThN is dissolved in UN. The oxide phase in the 5 wt % ThO_2 specimen gave a lattice parameter suggestive of a solution of UO_2 in ThO_2.

The second method of introducing ThO_2 into a UN matrix involved the preparation of uranium alloys containing 2 and 5 wt % Th by arc-melting. A solid-solution nitride powder was synthesized from the alloy by a hydride-nitride scheme. Samples prepared from this material and sintered at 2300°C gave a sharp, single-phase x-ray diffraction pattern with lattice parameters that obeyed Vegard's law for ThN levels to 5%. A number of samples were prepared from admixtures of this (U,Th)N and UO_2, with and without additions of carbon in the form of

graphite flour, and were sintered at 2300°C. X-ray analysis showed that additions of UO_2 lowered the lattice parameter of the nitride phase, indicating the removal of thorium. Metallographic examination revealed that an oxide phase had formed within the nitride grains while the grain boundaries were essentially free of oxide. The conclusion is, therefore, that the oxygen supplied by the UO_2 internally oxidized the thorium nitride preferentially with subsequent precipitation of $(Th,U)O_2$ *in situ*. The addition of carbon caused a decrease in oxygen content, as shown by chemistry and metallography, but also caused an increase in the solubility limit of oxygen in the nitride phase. This increase was evidenced by the lack of a second phase visible by optical metallography in high-carbon specimens which still contained significant amounts of oxygen. We conclude from this result that oxygen is either dissolved in the (U,Th)N or was in solution at high temperature and precipitated as a submicroscopic phase upon cooling. Electron metallography has not been completed on these specimens so the issue is not resolved.

Of the two methods described, it appears that supplying oxygen as UO_2 for a (U,Th)N solution holds considerably more promise of leading to fine-scale precipitates in UN. When ThO_2 was added to UN no gross redistribution of phases occurred, but when UO_2 was added to (U,Th)N the oxide was redistributed from coarse precipitates at grain boundaries to fine precipitates within the grains. We must further define the role of carbon in the process and determine the kinetics of the reactions so that heat treatments can be selected to produce the desired dispersion of precipitates.

2. FUEL ELEMENT DEVELOPMENT

G. M. Adamson, Jr.

Fabrication studies of refractory metals, alloys, and ceramic fuel compounds by thermochemical deposition have been continued. Preparation of irradiation specimens as fully enriched coatings of UO_2 on thoria and as partially enriched powders for fabrication of cold-pressed and sintered pellets has been held up due to difficulties in obtaining enriched UF_6. It has been proven, however, that in the system currently in use for solid deposits of UO_2 several pellets may be coated simultaneously. Further experiments in lithium reduction of UF_6 have shown that uranium nitride may be obtained when nitrogen is added to the system. Additional problems remain in obtaining a clean separation of uranium nitride from the by-product, lithium fluoride.

An apparatus is nearing completion for experiments to demonstrate the feasibility of the direct conversion of PuF_6 to PuO_2 powder by thermochemical deposition. Plutonium tetrafluoride was obtained for conversion to PuF_6 for feed material for the process. We are presently awaiting approval of various safeguards committees before starting the experiments.

Homogeneous internal deposits of tungsten-rhenium alloys have been obtained by use of an improved fluoride injector system. With this development, preparation of materials for mechanical properties evaluation has been started.

Results have been obtained on the influence of high-temperature irradiation and burnup on the stability of U_3O_8 and UO_2 dispersions in aluminum.

Deposition of Tungsten Alloys

J. I. Federer C. F. Leitten, Jr.

Improvements in compositional uniformity of tungsten-rhenium deposits through the use of a WF_6-ReF_6 injector were reported

previously.[1] The water-cooled injector introduced a severe temperature gradient into the reaction zone and caused hydrogen reduction of the fluorides to occur at lower than optimum temperatures for homogeneity. During the past quarter, the reaction-zone temperature was smoothed and increased by changing the injector design. Subsequently, deposits containing nominally 5, 25, and 90% Re were prepared using the new injector in a moving hot zone.

Noncooled injectors of nickel, type 304 stainless steel, and plain carbon steel were first tried in order to avoid the temperature gradient caused by a water-cooled injector. These injectors were either corroded in the fluoride atmosphere or plugged with deposit at temperatures in the range 800 to 1000°C. A water-cooled design was eventually adopted in which the water flow is minimized and the coolant passages extend completely through the furnace. Cooling of the WF_6-ReF_6 orifice is obtained with only 1 to 2 gal/hr of water and the furnace gradient is not significantly affected. For example, the mandrel surface temperature was 900 ± 10% over the 3-in. interval measured from the WF_6-ReF_6 orifice, the zone wherein most of the reduction reaction occurs.

Using the new injector in a moving hot zone, deposits were prepared at a hydrogen-to-WF_6 + ReF_6 ratio of 15:1 and at a pressure of 2 to 4 torr. The deposition temperature was 700°C for alloys containing nominally 5% Re and 900°C for alloys containing 25 and 90% Re. The resulting deposits had smooth surface textures, but the 90% Re alloy contained porosity. The microstructure of the 25% Re alloy indicated radial uniformity of composition. An electron probe analysis across the thickness of the sample is being performed, however, to determine whether slight banding indicates compositional variations. The 5% Re alloy is now being examined and analyzed.

The results that have been obtained using the WF_6-ReF_6 injector in a moving hot zone at higher deposition temperatures indicate that homogeneous tungsten-rhenium alloys can be prepared by this technique.

---

[1]J. I. Federer and C. F. Leitten, Jr., Fuels and Materials Development Program Quart. Progr. Rept. Mar. 31, 1965, ORNL-TM-1100, pp. 7–9.

Deposition of sufficient material for mechanical properties evaluation is now in progress.

Deposition of rhenium-rich alloys have also continued in the external coating apparatus.[2] Experiments were conducted at a hydrogen-to-WF_6 + ReF_6 ratio of 20:1, pressures of 4 and 10 torr, and temperatures of 500 to 650°C. Only thin dark coatings were obtained at 500, 550, and 600°C, but smooth-textured metallic deposits were obtained at 650°C. These deposits (tubular) usually had a single longitudinal crack and were separated from the tungsten-coated stainless steel mandrel. This behavior is attributed to differences in coefficients of expansion and to the grain orientation of the deposits. X-ray diffraction has shown a preferred orientation in unalloyed rhenium deposits in which (0002) and $(10\bar{1}1)$ are parallel to the substrate, an orientation which probably allows much less circumferential expansion in the deposit than in the mandrel. Another mandrel material, having a coefficient of expansion more closely matching that of the deposit will be used in future experiments. In spite of the deposit separation problem, the results of these experiments were encouraging because smooth, metallic, high-rhenium deposits were prepared for the first time in the external coating apparatus.

Deposition of Uranium Dioxide by Hydroreduction of Uranium Hexafluoride

R. L. Heestand C. F. Leitten, Jr.

Modifications to existing apparatus were completed to deposit enriched solid coatings of UO_2 onto thoria pellets by hydroreduction of UF_6. Whereas single pellets were coated previously, it was found that thickness uniformity could be controlled on five pellets simultaneously, in the apparatus available. Due to the small size of the hot zone, additional pellets in the gas stream give nonuniform coatings.

---

[2]J. I. Federer and C. F. Leitten, Jr., Fuels and Materials Development Program Quart. Progr. Rept. Dec. 31, 1965, ORNL-TM-1400, pp. 19–20.

An apparatus described below for investigating the feasibility of conversion of PuF_6 to PuO_2 will be checked out by preparing powder from 2.5% enriched UF_6 for irradiation experiment pellets.

Since the fully enriched UF_6 for the solid coatings and the 2.5% enriched material for conversion to UO_2 powder was not received until late this quarter, no radiation specimens have been prepared. Difficulties in obtaining the thoria pellets to be coated have also caused delay; however, these are expected early in the next quarter.

Preparation of PuO_2 Powder from PuF_6 by Thermochemical Reduction

R. L. Heestand W. C. Robinson
C. F. Leitten, Jr.

A process for the vapor phase formation of PuO_2 powder has been examined from a thermodynamic standpoint and appears feasible. The process involves the vapor phase reaction of PuF_6, H_2O, and H_2 according to the equation

$$PuF_{6(g)} + 2H_2O_{(g)} + H_{2(g)} \rightarrow PuO_{2(s)} + 6HF_{(g)} \quad .$$

The resulting PuO_2 powder will be formed in a heated alumina tube and subsequently collected in traps. The apparatus assembly is nearing completion and is being installed in alpha containment boxes. The apparatus is similar to that used for conversion of UF_6 to UO_2 powder and will be checked by producing a quantity of UO_2 powder prior to transfer to the Building 3019 alpha facility.

One difficulty encountered was the inability to obtain fluorinated plutonium compounds. After considerable time was spent in trying to obtain PuF_6, it was found that only PuF_4 was available. We ordered 2 kg of PuF_4 which was eventually received and transferred into 200-g batches. An additional step has been placed in the system for fluorinating the PuF_4 to PuF_6, and we are currently awaiting approval from the Radiochemical Plant Committee to proceed with the experiments.

Deposition of Uranium Compounds by Lithium Vapor Reduction of Uranium Hexafluoride

W. C. Robinson C. F. Leitten, Jr.

Previous work[3] has established the feasibility of the reaction

$$UF_{6(g)} + 6Li_{(g)} \rightarrow U_{(s)} + 6\ LiF_{(g)} .$$

During this period, nitrogen gas was introduced into the reaction chamber in the expectation that it would react with the uranium metal powder product of the above reaction to form uranium nitride.

The results of these experiments were solid deposits composed of uranium metal, uranium nitride (both UN and UN_2), and various lithium-uranium compounds including $Li_7U_6F_3$ and Li_3UF_7. In one experiment, a fine powder was obtained in the cold trap. This powder ignited when exposed to air. X-ray analysis of the residue indicated a mixture of UN_2 and UO_2.

Attempts will be made to separate the uranium nitride solid product from the LiF and other lithium-uranium compounds by heating the chamber, after reaction, to 1250°C under vacuum in an effort to remove the more volatile compounds from the deposit.

Irradiation Testing of Aluminum-Base Miniature Fuel Plates

M. M. Martin A. E. Richt

In cooperation with the Phillips Petroleum Company, a series of aluminum-base miniature test plates were fabricated for determining the influence of high-temperature irradiations to high burnups on the dimensional and chemical stability of U_3O_8 and UO_2 dispersions. The fissile materials were particles of U_3O_8 and niobium-coated UO_2–15 wt % ZrO_2 dispersed in a matrix of X8001 aluminum and roll bonded at 500°C with Alclad 6061 aluminum. The design of the miniatures, which included instrumented as well as standard plates, and the fabrication results were previously reported.[4]

---

[3]W. C. Robinson and C. F. Leitten, Jr., Fuels and Materials Development Program Quart. Progr. Rept. Mar. 31, 1966, ORNL-TM-1500, pp. 11–12.

[4]M. M. Martin, W. J. Werner, and C. F. Leitten, Jr., Fabrication of Aluminum-Base Irradiation Test Plates, ORNL-TM-1377 (February 1966).

Testing of the fuel specimens began in the latter part of 1964 and was completed by mid-1965. The miniatures received maximum burnups in the range of 16 to 17 $\times 10^{20}$ fissions/cm^3 at cladding-film interface temperatures of 238 to 265°C without indication of failure.

Examination of the U_3O_8-bearing fuel specimens (the reference HFIR and ATR fuel material) revealed no evidence of unexpected microstructural changes. Reaction between the U_3O_8 fuel particles and the aluminum matrix was apparent in all specimens; however, the extent of reaction appeared to be primarily a function of the irradiation temperature, not fuel burnup. This effect is clearly shown in Fig. 2.1, where a specimen irradiated to 6.3 $\times 10^{20}$ fissions/cm^3 at 110°C reacted less than an identical specimen irradiated to 3.9 $\times 10^{20}$ fissions/cm^3 at 165°C. Significantly greater reaction occurred in a specimen irradiated to 9.4 $\times 10^{20}$ fissions/cm^3 at 182°C, and complete reaction between the U_3O_8 and the matrix had occurred after 16.1 $\times 10^{20}$ fissions/cm^3 at 238°C, as shown in Fig. 2.2. The burnup level and test temperature achieved by this test specimen without evidence of gross failure are both significantly higher than the maximum conditions expected in the HFIR.

The specimens fueled with the niobium-coated UO_2-ZrO_2 fuel particles exhibited a number of interesting microstructural damages. Figure 2.3 shows that the niobium coating successfully prevented reaction between the fuel particles and the aluminum matrix during irradiation. The extent of fission-gas porosity in the fuel particles was found to be directly proportional to the fuel burnup. Some reaction between the niobium coating and the aluminum matrix was evident in the higher performance specimens; however, this effect is attributed to the higher irradiation temperatures and not to a burnup effect. Measurements of the fuel particle diameter showed that the UO_2-ZrO_2 fuel particles swelled at a rate of 1.3% volume change per atom percent ^{235}U fissioned The particles did retain the fission products and their spherical shape with this degree of severe swelling, but offer no major advantage over the reference fuel. Its fabrication costs compared to other fuels also makes its use unattractive.

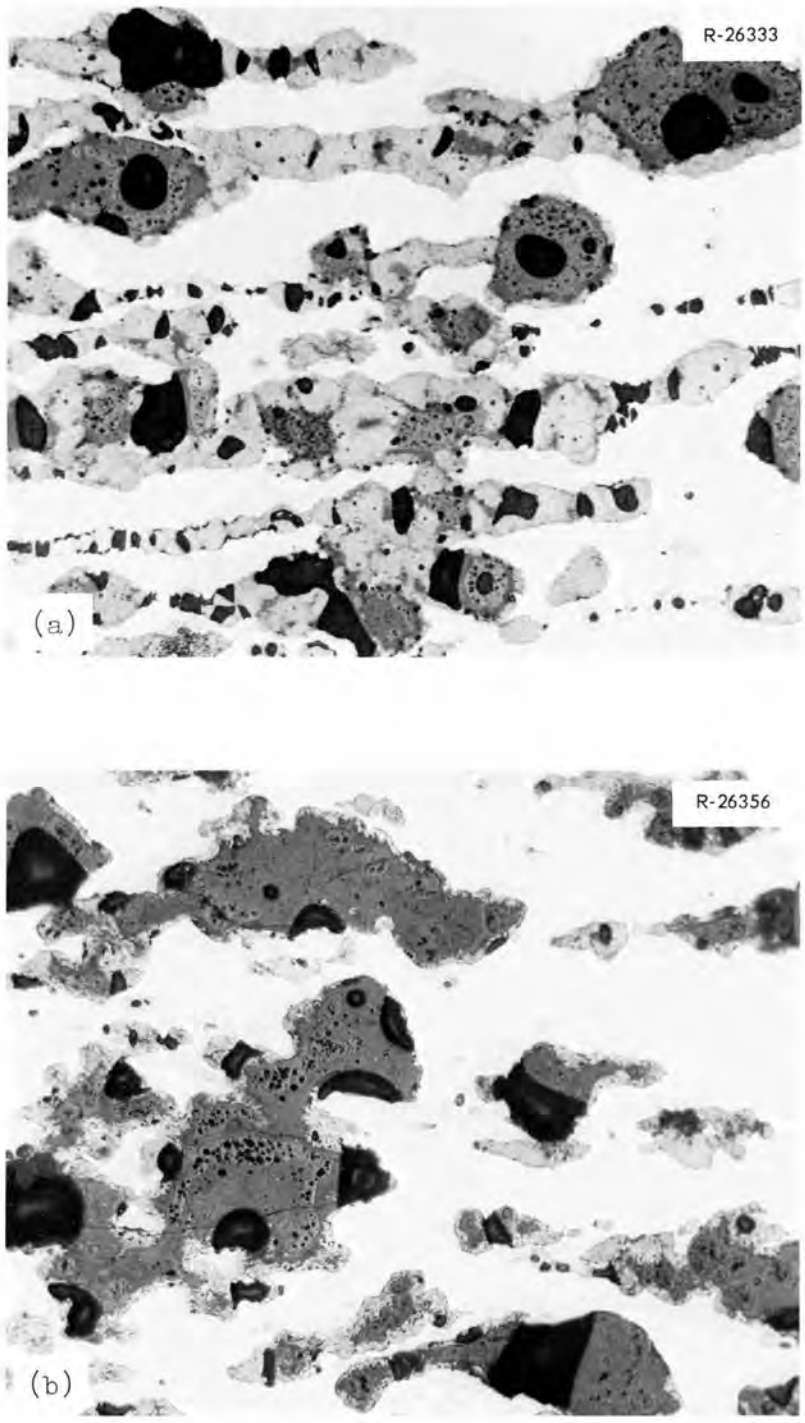

Fig. 2.1. Effect of Temperature Upon the Reaction of U_3O_8 with Aluminum During Irradiation. As polished. 250X. (a) Irradiated to 3.9×10^{20} fissions/cm^3 at 165°C; (b) irradiated to 6.3×10^{20} fissions/cm^3 at 110°C.

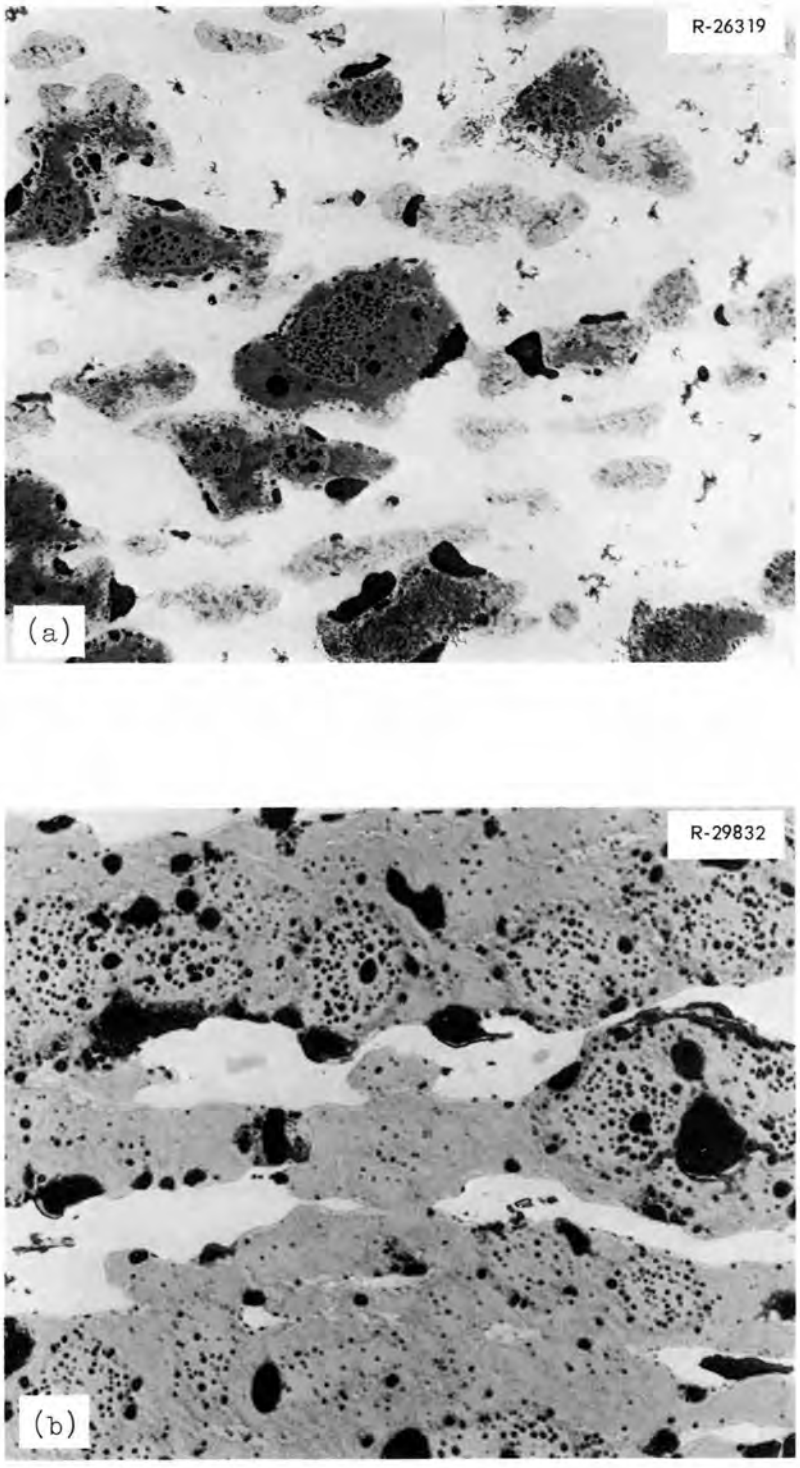

Fig. 2.2. Microstructure of Al–41 wt % U_3O_8 Fuel Specimen after Irradiation. As polished. 250×. (a) Irradiated to 9.4×10^{20} fissions/cm^3 at 182°C; (b) irradiated to 16.1×10^{20} fissions/cm^3 at 238°C.

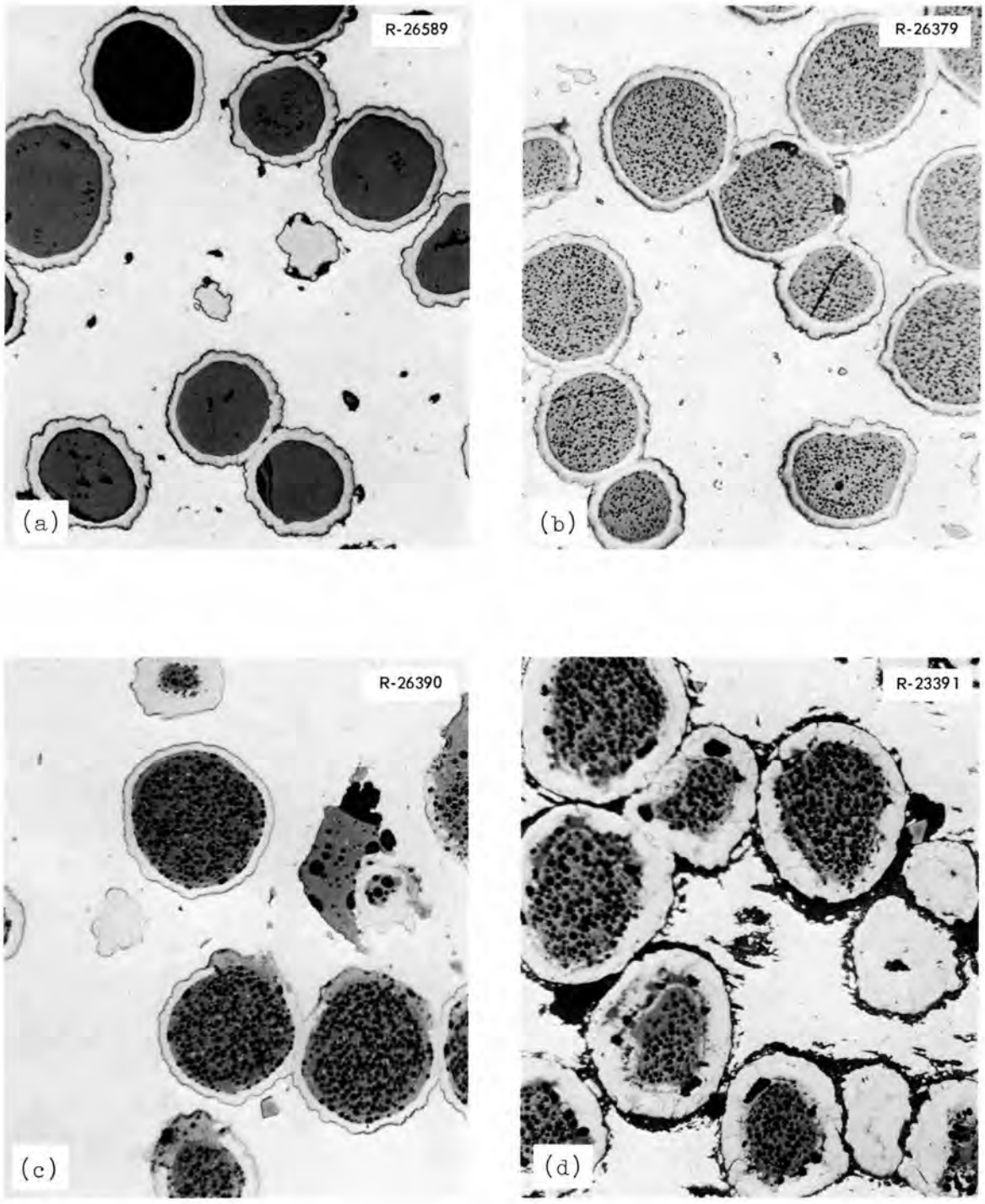

Fig. 2.3. Typical Appearance of Niobium-Coated UO_2-ZrO_2 Fuel Particles in HFIR Irradiation Test Plates. (a) As fabricated; (b) after 6.9×10^{20} fissions/cm^3 at 216°C; (c) after 8.8×10^{20} fissions/cm^3 at 199°C; (d) after 17.0×10^{20} fissions/cm^3 at 268°C. As polished. 250×.

3. MECHANICAL PROPERTIES

J. R. Weir, Jr.

One objective of this program is to determine the effect of irradiation on the mechanical properties of alloys of interest as fuel cladding and to find a metallurgical condition for the alloys that produces the least effect of subsequent irradiation on the mechanical properties. To accomplish this, our study concerns the interaction of radiation-induced defects and the substructure of the alloys, the effect of irradiation temperature, postirradiation test variables, and neutron dosimetry in the facilities used in the irradiations. The material selected for initial study is type 304 stainless steel.

Postirradiation and Stress Rupture of Type 304 Stainless Steel

W. R. Martin J. R. Weir

In order to improve the stress-rupture properties of irradiated type 304 stainless steel at 650°C, we are investigating the effect of preirradiation heat treatments. From the early work on tensile ductility of irradiated stainless steel, a small grain size or aged structure improves the ductility. The aging treatment consists of producing a desirable form of grain-boundary carbides.

Garofalo[1] has enumerated the conditions for which grain boundary precipitation can be beneficial. These are:

1. high cohesion between particle and matrix,
2. interparticle spacing of 1 or 2 μ to allow grain-boundary migration,
3. particles that are rounded and have high shear strength.

In the case of stainless steels, the rupture life in the 500 to 700°C temperature range is greatly affected by the morphology of grain-boundary carbides. A fine dendritic structure is often seen which

[1]Frank Garofalo, Fundamentals of Creep and Creep-Rupture in Metals, Macmillan and Company, New York, 1965.

occupies a large fraction of the grain-boundary surface and the interfacial strength between the matrix and this precipitate is very low. Thus, Garofalo aged stainless steel at 815°C to spheroidize carbides and improved the stress-rupture life at 593°C. In this case the spheroidization of grain-boundary carbides did not affect the strain-time relationship in creep, but the higher ductility resulted in an increase in the rupture life. The improved ductility was attributed to (1) high adherence between matrix and particles or (2) suppression of crack formation by grain-boundary migration.

While this aging treatment does not affect the creep relationship, a reduction in grain size will result in a higher creep rate. Thus, if one selected a coarse-grain size to lower the creep rate and produced the desired form of grain-boundary precipitation to improve ductility, the stress rupture and creep properties of the alloy would be optimum.

We have produced fine-grain size (ASTM 9) and coarse-grain size (ASTM 5) samples from the same heat. The coarse-grain size material was given an aging treatment of 100 hr at 800°C following the 1036°C solution anneal. The postirradiation stress-rupture properties at 650°C are given in Table 3.1 for these three treatments. As can be noted, the ductilities of the fine-grain size and the aged, coarse-grain size material are superior to that of the coarse-grain size material. The rupture life of the aged, coarse-grain material is superior to the fine grain because of the lower creep rate. This is illustrated in Fig. 3.1.

Photomicrographs of the fractured area for each of three types of treatments are also given in Fig. 3.1 for tests at 20,000 psi. It is noted that intergranular fracture is evident in all three samples. The principal difference between the aged and unaged coarse-grain material is associated with crack widening. Thus, the role of these carbides in improving ductility is probably associated with crack propagation. The carbide distribution along these boundaries after specimen fracture at 20,000 psi are given in Fig. 3.2. In general, the precipitates in the aged samples are larger and perhaps have a larger interparticle spacing. Differences in shape are not resolvable at 1000X in terms of roundness, but the precipitates in the aged samples appear more elongated.

Table 3.1. Stress Rupture and Ductility of Irradiated Type 304 Stainless Steel at 650°C Per Pretest Heat Treatment

Stress (psi)	Time to Rupture, hr			Total Elongation at Fracture, %		
	Fine Grain	Coarse Grain	Aged, Coarse Grain	Fine Grain	Coarse Grain	Aged, Coarse Grain
$\times 10^3$						
30	11.3	1.5	14.8	44.0	11.4	24.2
25	79.0	5.5	50.8	29.5	9.0	25.1
20	191.0	109.5	664.1	17.2	3.8	14.3
15	514.4	194.4	3638.0	9.2	3.5	7.8

ORNL-DWG 66-4971

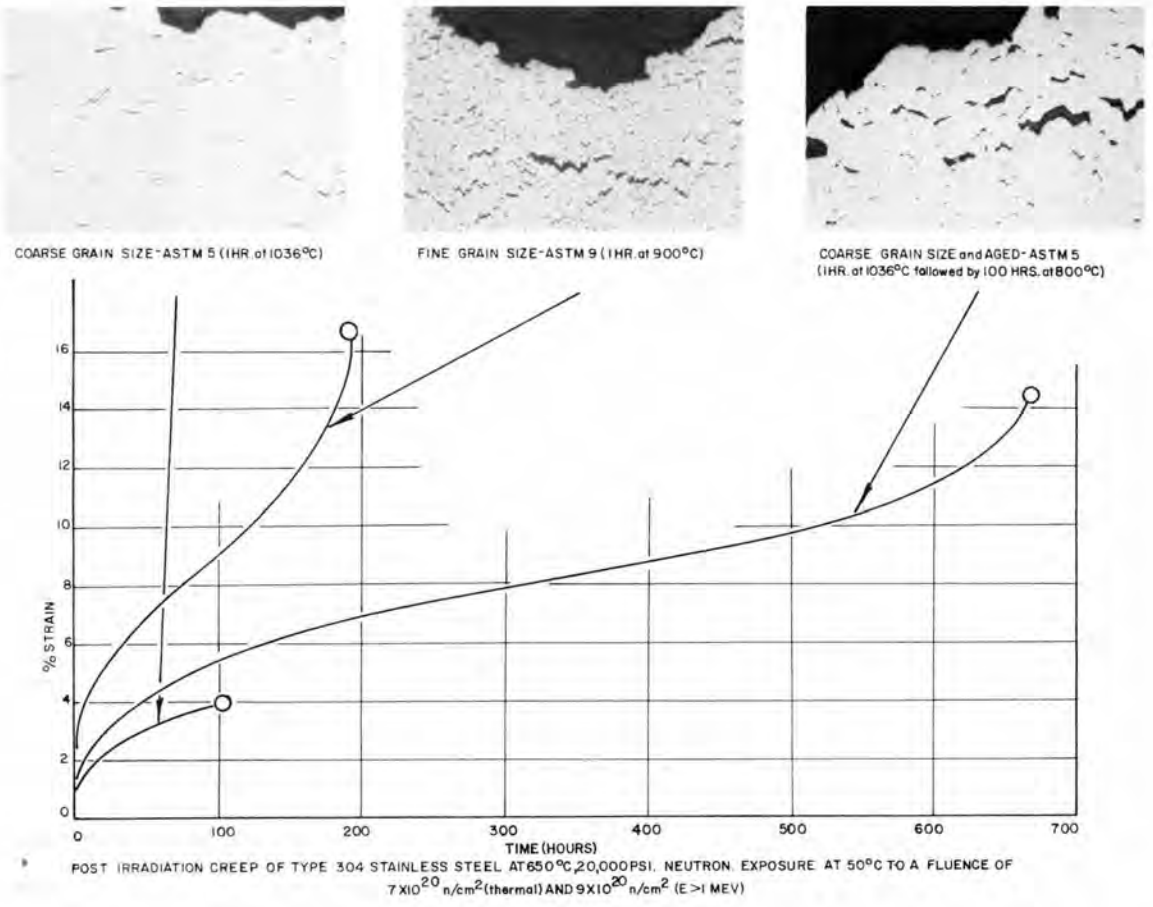

Fig. 3.1. Postirradiation Creep of Type 304 Stainless Steel at 650°C, 20,000 psi, Neutron Exposure at 50°C to a Dose of 7×10^{20} neutrons/cm^2 (Thermal) and 9×10^{20} neutrons/cm^2 (E > 1 Mev).

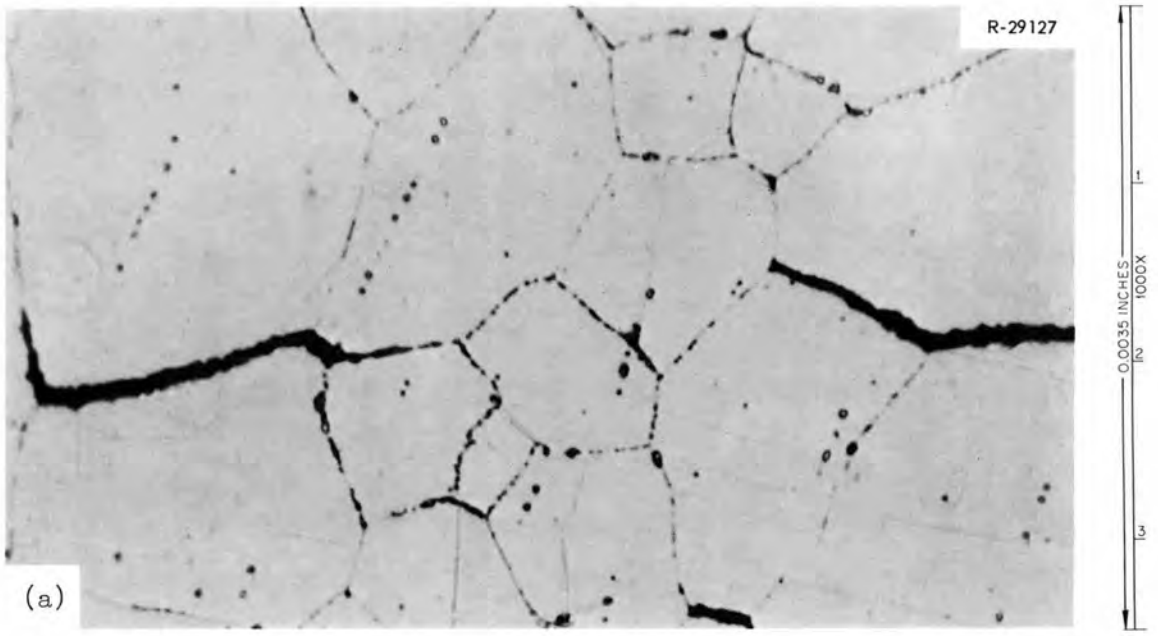

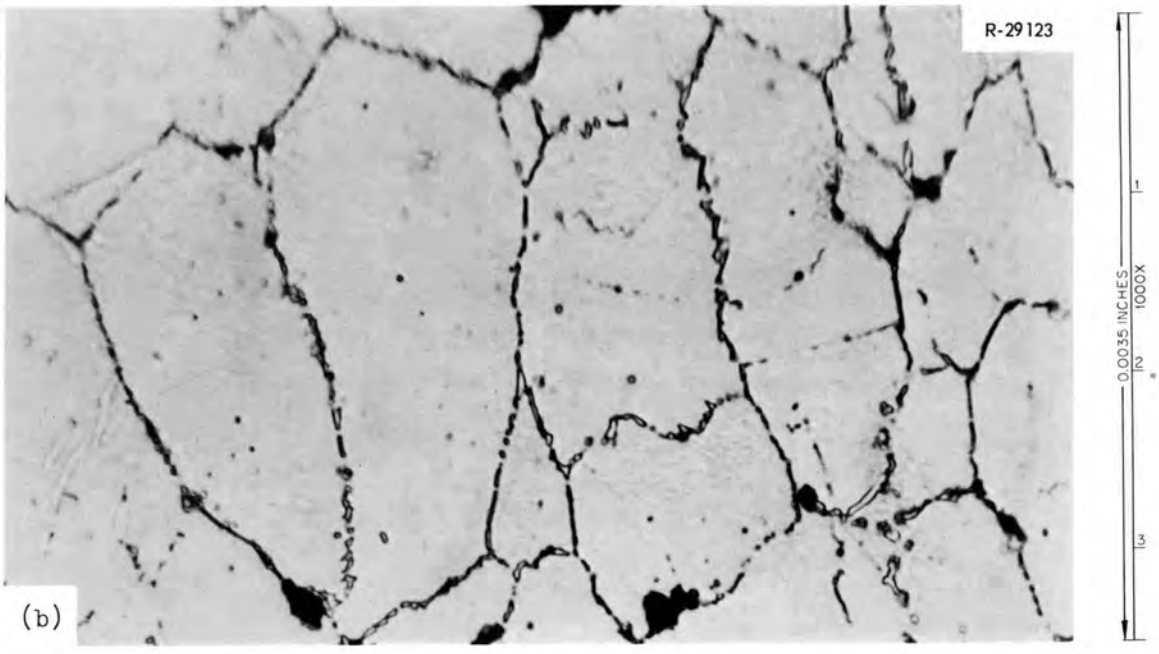

Fig. 3.2. Precipitate in the Boundaries of Pretest Unaged and Aged, Coarse-Grain Size Material. (a) Unaged, coarse-grain size. (b) Aged, coarse-grain size. Etchant: Glyceria regia.

Effects of Irradiation Temperature On the Properties and Structure of Austenitic Stainless Steel

E. E. Bloom J. O. Stiegler
W. R. Martin J. R. Weir

An investigation of the effects of irradiation temperature upon mechanical properties of austenitic stainless steel is continuing. Annealed type 304 stainless steel tensile specimens along with small sheet specimens for transmission electron microscopy studies have been irradiated at temperatures between 93 and 454°C to a total fast neutron exposure of 7×10^{20} neutrons/cm^2. After irradiation, the specimens were tested at room temperature and at an engineering strain rate of 0.02 min^{-1}. Tensile data are given in Table 3.2. Both the room-temperature yield stress and ultimate tensile strength have a maximum value at 150°C. Transmission electron microscopy reveals that a high density of black dots, approximately 50 A in diameter, are present at 93°C. For irradiation temperatures between 121 and 300°C, the dots are 100 to 200 A in diameter. As the irradiation temperature is increased the density of dots decreases slightly, for temperatures up to 300°C. Electron microscopy results indicate that the dots are strain fields present in the lattice. They are probably caused by clustering of vacancies or interstitials that result from fast neutron bombardment. At 371°C no dot defects are present. The sharp decrease in dot density between 300 and 371°C corresponds to the drop in room-temperature yield stress from 90,000 to 40,000 psi. It is thus concluded that the strengthening that occurs after irradiation at temperatures below 300°C is a result of defect clusters that are formed and that the maximum at 150°C is a result of a critical size and/or density of the defects. At 371, 398, and 454°C disk-shaped precipitates form within the grains.

Preliminary results indicate that deformation in a specimen containing the fine dotlike structure is concentrated in narrow slip bands with little or no deformation occurring between the bands. Specimens irradiated at higher temperatures (such that the dotlike defects are not formed) deform homogeneously.

This work is continuing at the present time and a detailed report will be issued shortly.

Table 3.2. Room-Temperature Tensile Properties of Irradiated Type 304 Stainless Steel

Irradiation Temperature (°C)	Yield Stress (psi × 10^3)			Ultimate Tensile Strength (psi × 10^3)		Fracture Stress (psi × 10^3)	True Strain, %		Elongation at Fracture (%)
	0.2% Offset	Upper	Lower	Engineering	True		Uniform	Fracture	
93	86.6	90.7	85.4	112.2	170.9	288.2	42.0	141.0	58.8
121	94.3	96.7	90.2	115.5	169.3	246.0	38.2	119.5	52.8
149	99.2	100.8	93.5	118.9	171.8	228.4	36.8	111.0	50.4
176	95.1	96.7	92.3	113.8	169.1	247.0	39.6	122.0	54.4
300	91.5			113.8	147.5	296.7	25.9	139.0	36.5
343	51.2			99.2	133.0	230.0	29.4	134.0	40.4
371	40.7			97.7	142.5	283.8	37.7	154.0	52.0
398	45.5			95.9	150.0	245.0	44.6	141.0	63.0
454	43.5			96.8					66.6

4. NONDESTRUCTIVE TEST DEVELOPMENT

R. W. McClung

Our program is intended to develop new and improved methods of evaluating reactor materials and components. To achieve this we are studying various physical phenomena, developing instrumentation and other equipment, devising application techniques, and designing and fabricating reference standards. Among the methods being actively pursued are electromagnetics (with major emphasis on eddy currents), ultrasonics, and penetrating radiation. In addition to our programs oriented toward the development of methods, we are studying these and other methods for remote inspection.

Electromagnetic Test Methods

C. V. Dodd

Analytical Studies

We have continued research and development on electromagnetic phenomena on both an analytical and empirical basis. As part of our program, we are studying the mathematical determination of electromagnetic phenomena of a coil as a function of coil dimensions, frequency, specimen conductivity and permeability, and coil-to-specimen spacing. We have constructed a family of four coils of the same shape but different sizes and made a series of impedance measurements as a function of frequency and "lift-off" (coil-to-metal spacing). A composite plot of the coil impedance for various frequencies and lift-off values is shown in Fig. 4.1. The experimental points are a standard deviation weighted average of measurements from each of the four coils. The calculated points were determined by our relaxation program. The agreement is quite good, especially in the conductivity. The error in lift-off is due to the fact that our relaxation program only defines the location of the coil within one-half a lattice spacing. The error in lift-off is within this range and could be decreased further with a finer lattice but at an increased computer cost.

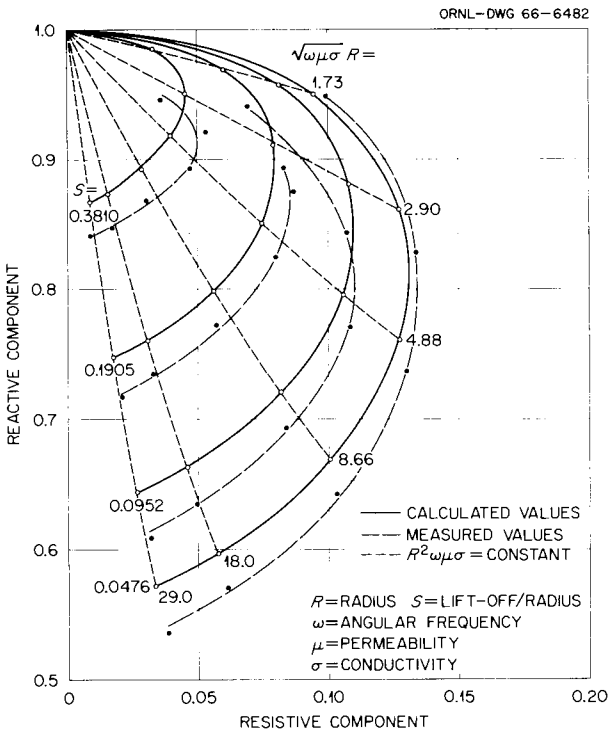

Fig. 4.1. Calculated and Measured Values of Coil Impedance.

Phase-Sensitive Eddy-Current Instrument

Further improvements have been made on the phase-sensitive eddy-current instrument. An effort has been made to decrease the amount of "apparent" phase shift due to the signal amplitude variation. This apparent or erroneous phase shift occurs due to the base current loading of the discriminator transistors and the addition of an "out-of-phase" null voltage to the signal voltage. By using high gain transistors in the discriminator circuit, decreasing the resistance in the base current bias network of the discriminator transistors and decreasing the null voltage, we have decreased the "apparent" phase shift by a factor of 10. This improvement will allow a greater range of allowable lift-off with the same measurement sensitivity or a greater range of measurements with the same lift-off insensitivity.

A new portable phase sensitive instrument (Fig. 4.2) has been constructed. The instrument operates at frequencies of 50 and 500 kc and may be used for conductivity, cladding and thickness measurements, and other eddy-current test applications.

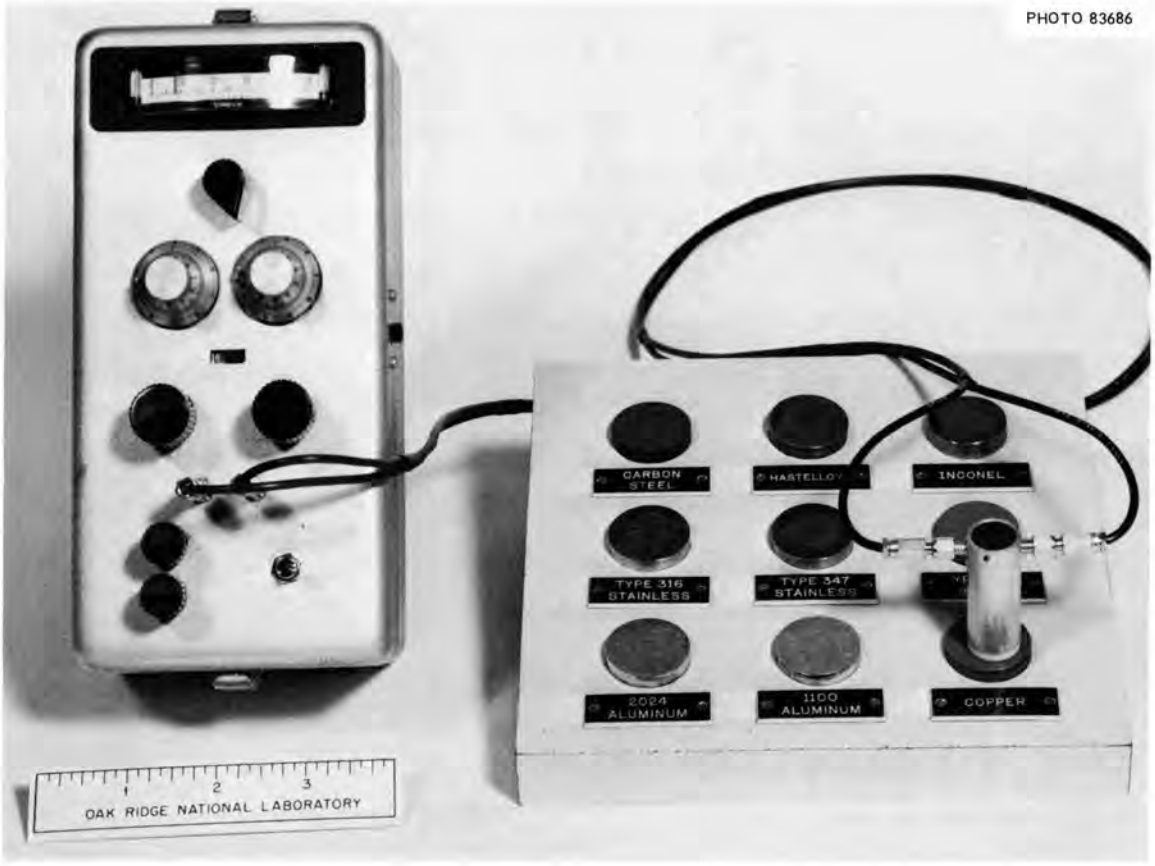

Fig. 4.2. Prototype Portable Phase-Sensitive Eddy-Current Instrument.

Ultrasonic Test Methods

K. V. Cook

Tubing Inspection

We are continuing to work on the problems encountered in tubing inspection. A major problem is the establishment of realistic reference notch standards for calibration. Electro-discharge machining appears to be a reliable method for making both outer- and inner-surface notches, and we are continuing to use this technique for our studies. Recently, we have machined EDM notches in areas of poor accessibility where notch replications could not be made with RTV-60 silicone rubber without diluting it. Since dilution of RTV-60 causes shrinkage and becomes excessive if a large percentage of diluent is required, a

lower viscosity rubber (RTV-11) was substituted. When RTV-11 is used, a small amount of RTV-60 is added to color the replica so the differential focusing technique can be applied. Shrinkage is in the order of 0.5% for either (nondiluted) rubber. Metallographic sections of both notches and their replicas have been taken and correlation between the two are excellent. Figure 4.3a shows in cross section an approximate center position of an outer-surface notch, 0.0032 in. deep, 0.002 in. wide, and 1/2 in. long. The differential focusing technique was used to measure the depth of this notch before sectioning. The apparent average depth as measured by this technique was 0.0032 in. (±0.00008 in.). As is evident from the photomicrograph, the depth was confirmed. Figure 4.3b is a cross section of the replica of the notch in the same general area. Again the depth was confirmed.

Optical Systems

We have increased the versatility of our optical system (Schlieren) so that we can view pulses of ultrasound in transparent solids with a method involving the photo-elastic effect. With the aid of polarized light, interference patterns generated by ultrasonic energy propagating through transparent epoxy sheets (cast from Araldite 502)[1] have been observed. This will now allow us to observe the behavior and interactions of sound within solids.

Penetrating Radiation

B. E. Foster S. D. Snyder

Gaging Probes for Hollow Cylindrical Specimens

During a literature survey concerning the use of various light transmitting materials for light pipes, our attention was focused on the use of fiber optics for this application. We purchased a 1/4-in.-diam, 36-in.-long commercial fiber-optics bundle and used it to

[1]CIBA Products Company, Fair Lawn, New Jersey.

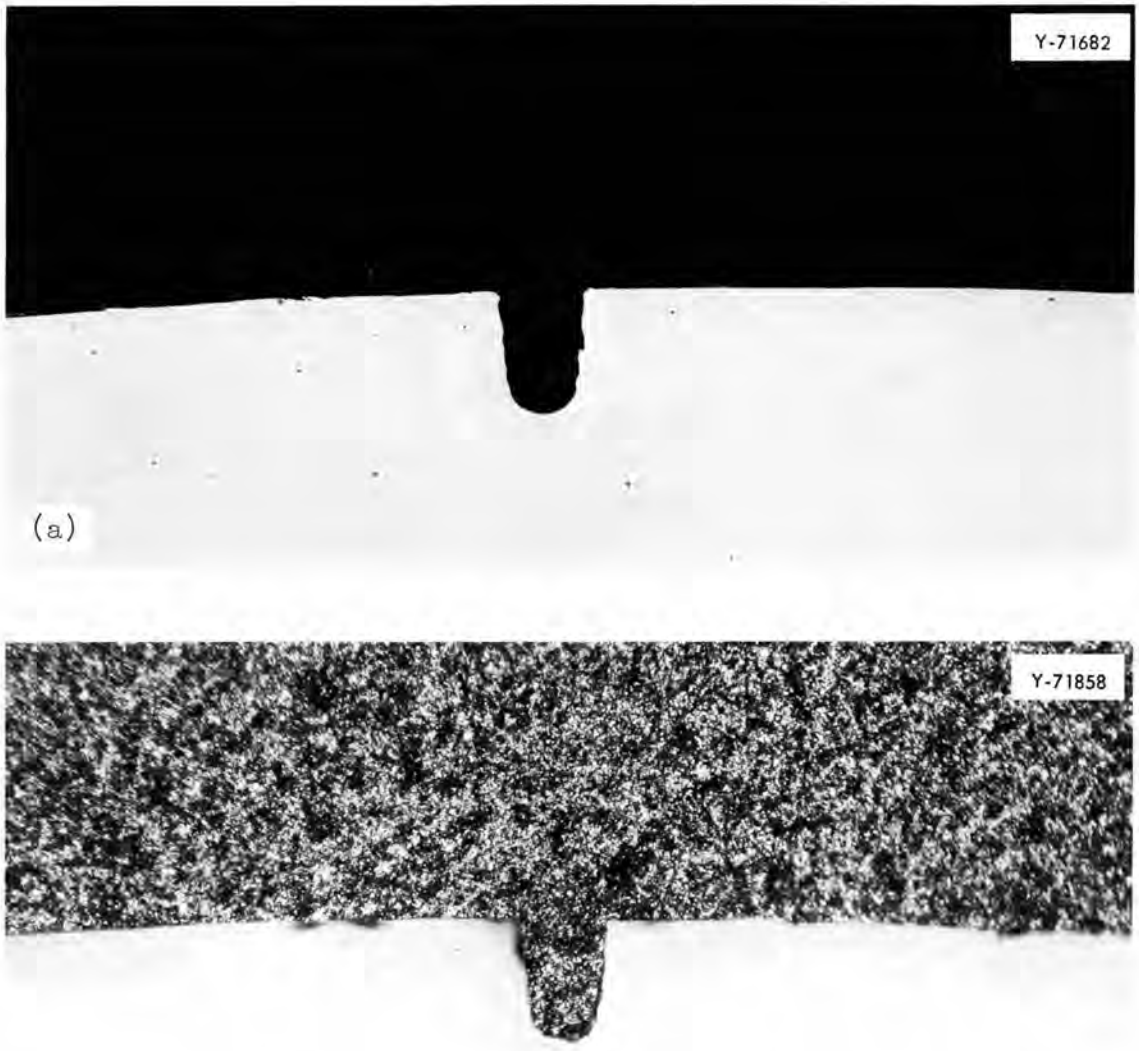

Fig. 4.3. Comparison of Electro-Discharge Machined Notch and the Silicone Rubber Replica. As polished. 200×. (a) Notch; (b) replica.

transmit the light produced by a scintillated 1/4-in.-diam, 1/2-in.-long NaI(Tl) crystal to an RCA 6342A photomultiplier.

We compared the performance of the fiber optics bundle with a similar length and diameter of Lucite, using the photomultiplier output signal as indicated by a digital voltmeter. Signals were compared for both light pipe materials with 6061 aluminum attenuating a

50 KVCP, 0.078-in.-diam collimated x-ray beam. The fiber optics bundle produced a much greater sensitivity to aluminum thickness changes than did the Lucite.

We have used this same fiber optics bundle, NaI(Tl) crystal, and photomultiplier combination to measure the tungsten coating thickness of vapor deposited tungsten on the inside wall of copper tubing. This was done for the HTM Project.

5. ZIRCONIUM METALLURGY

M. L. Picklesimer

We are conducting research along several lines on zirconium-base alloys of potential use as structural materials for water-cooled and/or moderated reactor systems. The principal projects are: (1) studies of the physical metallurgy, including transformation kinetics and morphologies, mechanical properties, phase diagrams, and heat-treatment response; (2) the development, evaluation, and utilization of preferred orientation and strain anisotropy in α-zirconium alloys during fabrication, and the use of yield stress anisotropy in increasing maximum permissible design stresses in structures; (3) the determination of the effects of composition, temperature, and environment on the oxidation-corrosion rates in the thin film stage of oxide growth; (4) a study of the effects of alloy composition and oxidation environment on the structural properties of thin oxide films in situ; and (5) investigation of stress orientation of hydrides in Zircaloy-2.

Anisotropy in Zircaloy-2 and Zircaloy-4

P. L. Rittenhouse M. L. Picklesimer

Zircaloy Tubing

The torsion testing of the six lots of Zircaloy tubing[1] was begun but could not be completed due to the failure of the internal expanding mandrel for the 1/2-in.-OD tubing during a test. A commercially available expanding mandrel has been obtained as a replacement. Testing of the 3/4-in.-OD tubing was also stopped until new instrumentation could be installed for better programming of the torsion tests. The torsion testing program has been resumed.

---

[1]P. L. Rittenhouse and M. L. Picklesimer, Fuels and Materials Development Program Quart. Progr. Rept. Mar. 31, 1965, ORNL-TM-1500, pp. 26–28.

One of the problems encountered in the testing of tubing in biaxial stress is that of determining the uniformity of strain throughout the gage section of the specimens. During an earlier study of strain patterns in sheet-type tensile specimens,[2] a grid of lines was placed on the specimen by anodizing through an exposed and developed photoresist film. The grid lines consisted of oxide films only 200 to 300 A in thickness and did not interfere with the deformation of the specimen. A cylindrical light source has been obtained for applying the photoresist grids to the tubular specimens, and anodized grids will be applied to all test specimens in the future. The grid pattern on each specimen will be photographed on Polaroid transparencies before, at several stages during, and after each test. The uniformity and development of the strain pattern during the test can be examined and followed by intercomparison of the grid distortions.

Short lengths of each of the six lots of Zircaloy tubing were examined metallographically on surfaces perpendicular to the axial, radial, and tangential directions. Grain size measurements were made on each surface of each lot of tubing. In each material, the grains were found to be equiaxed and essentially the same size. The grain size, however, varied considerably between materials. The data are presented in Table 5.1. The range of grain sizes observed in the Zircaloy-2 specimens, ASTM 7-10, is not unusual. Those found in the Zircaloy-4 specimens are larger. It is not known whether the larger grain size is typical of Zircaloy-4 material or whether it is peculiar to these specific lots.

Yield Surfaces

The method of determination of the yield surface from Knoop microhardness measurements[3] has been used to predict the uniaxial yield

---

[2]P. L. Rittenhouse and M. L. Picklesimer, Strain Behavior in Zircaloy-2 Sheet-Type Tensile Specimens, ORNL-TM-1226 (September 1965).

[3]P. L. Rittenhouse and M. L. Picklesimer, Fuels and Materials Development Program Quart. Progr. Rept. Mar. 31, 1966, ORNL-TM-1500, pp. 28–38.

Table 5.1. Grain Size in Zircaloy Tubing

Material Code	Material Description	Grain Size Number Designation	Average Area per Grain (mm^2)
			$\times 10^{-4}$
A	3/4-in.-OD Zircaloy-2	9–10	2
B	1/2-in.-OD Zircaloy-2	8–9	4
C	3/4-in.-OD Zircaloy-2	7	10
D	1/2-in.-OD Zircaloy-2	8	5
E	3/4-in.-OD Zircaloy-4	5–6	29
F	1/2-in.-OD Zircaloy-4	5–6	29

strengths along the principal fabrication directions of the six lots of Zircaloy tubing. In each case, the experimentally determined value of the compression yield strength in the axial direction was equated to the intersection of the yield locus with the compression axis in both the Z,θ(axial, tangential) and Z,R(axial, radial) stress planes. The experimental value used is given in Table 5.2 along with the predicted tensile and compressive yield strengths for the radial and tangential directions and the experimental and predicted yield strengths in the axial directions. The predicted yield strengths are in good agreement with those estimated on the basis of the preferred orientation existing in the tubing and the related uniaxial tensile and compressive yield strengths known in sheet and plate material.

Yield and Flow in Uniaxial Tension and Compression

The recent progress in the characterization of the three-dimensional anisotropy of yielding and flow in Zircaloy-2 from a single uniaxial test was summarized in the last progress report.[4] One simplification

[4]P. L. Rittenhouse and M. L. Picklesimer, Fuels and Materials Development Quart. Progr. Rept. Mar. 31, 1966, ORNL-TM-1500, pp. 38–43.

Table 5.2. Yield Strength of Zircaloy Tubing

Material Code	Yield Strength, psi						
	Axial Direction			Radial Direction		Tangential Direction	
	Compression[a]	Tension[a]	Tension[b]	Compression[b]	Tension[b]	Compression[b]	Tension[b]
	$\times 10^3$	$\times 10^3$	$\times 10^3$	$\times 10^3$	$\times 10^3$	$\times 10^3$	$\times 10^3$
A	71.0	61.0	61.0	90.0	80.5	84.0	76.5
B	61.0	56.5	55.0	67.0	59.0	66.0	60.0
C	64.5	52.5	51.0	70.0	61.0	81.0	77.0
D	54.5	49.0	47.5	65.5	59.5	59.0	55.0
E	68.0	56.5	56.5	78.0	72.0	75.0	73.0
F	65.0	60.0	59.0	81.0	72.0	76.0	72.0

[a]Value determined by experiment.

[b]Predicted value.

of the procedure described previously has been found. By inspection of the plot of the strain anisotropy constants in tension vs those in compression, it was found that the ratio of the complementary k values in tension (k_{ij}/k_{ik}) was equal to some power of the ratio of the complementary k values in compression (k_{-ij}/k_{-ik}) along the same stress axis. The best fit with the experimental data is obtained when the power exponent is equal to 2.1 or 2.2. However, a value of 2.0 was selected for the power exponent since the calculation required is simpler, and the error resulting is insignificant compared to the spread in experimental values.

From such a relationship,

$$k_{ij}/k_{ik} = (k_{-ij}/k_{-ik})^2 \qquad (1)$$

and

$$k_{\pm ij} + k_{\pm ik} = -1 \quad , \qquad (2)$$

it is easy to show that

$$k_{-ij} = -(k_{ij}/k_{ik})^{1/2}/[1 + (k_{ij}/k_{ik})^{1/2}] \qquad (3)$$

and

$$k_{ij} = -(k_{-ij}/k_{-ik})^{1/2}/[1 + (k_{-ij}/k_{-ik})^{1/2}] \quad , \qquad (4)$$

thus allowing calculation of values of k in tension from those in compression, and vice versa.

Values of the strain anisotropy constants so calculated are compared in Table 5.3 with experimentally determined values for eight lots of Zircaloy-2 sheet material. In two cases, the fit between experimental and calculated values in tension was poor. By selecting either the transverse or normal directions rather than the rolling direction as the starting point for the calculation, it can be shown that the experimental value in both cases is suspect. An experimental redetermination of the suspect values has since shown that the experimental values reported in Table 5.3 are incorrect, probably due to a mix-up in specimen orientation at the time of the original test. The calculated values are essentially correct.

Table 5.3. Experimental and Calculated Strain Anisotropy Constants

Schedule	Given Experimental Value		Calculated and Experimental Values											
	$\lvert k_{-xy} \rvert$	$\lvert k_{xy} \rvert$	$\lvert k_{-xy} \rvert$		$\lvert k_{xy} \rvert$		$\lvert k_{-yx} \rvert$		$\lvert k_{yx} \rvert$		$\lvert k_{-zx} \rvert$		$\lvert k_{zx} \rvert$	
			exp[a]	cal[b]	exp[a]	cal[b]	exp[a]	cal[b]	exp[a]	cal[b]	exp[a]	cal[b]	exp[c]	cal[b]
6	0.658		0.658	0.628	0.739	0.786	0.674	0.670	0.812	0.805	0.513	0.515	0.604	0.530
		0.739					0.674	0.667	0.812	0.799	0.513	0.530	0.604	0.560
8	0.714		0.714	0.735	0.885	0.862	0.701	0.707	0.884	0.853	0.488	0.492	0.498	0.484
		0.885					0.701	0.730	0.884	0.880	0.488	0.495	0.498	0.490
10	0.579		0.579	0.592	0.678	0.654	0.622	0.617	0.784	0.722	0.551	0.540	0.633	0.579
		0.678					0.622	0.645	0.784	0.773	0.551	0.558	0.633	0.614
13	0.610		0.610	0.625	0.735	0.710	0.630	0.636	0.741	0.753	0.512	0.522	0.508	0.544
		0.735					0.630	0.638	0.741	0.756	0.512	0.514	0.508	0.528
16	0.565		0.565	0.569	0.634	0.628	0.600	0.609	0.695	0.708	0.530	0.530	0.568	0.560
		0.634					0.600	0.622	0.695	0.730	0.530	0.556	0.568	0.610
18	0.485		0.485	0.484	0.469	0.470	0.534	0.545	0.693[d]	0.590	0.558	0.560	0.719	0.626
		0.469					0.534	0.552	0.693[d]	0.605	0.558	0.568	0.719	0.632
62	0.527		0.527	0.519	0.585	0.553	0.570	0.577	0.689	0.650	0.550	0.550	0.611	0.598
		0.585					0.570	0.585	0.689	0.666	0.550	0.519	0.611	0.585
J	0.450		0.450	0.415	0.330[d]	0.400	0.520	0.540	0.575	0.575	0.600	0.569	0.733	0.635
		0.330[d]					0.520	0.500	0.575	0.500	0.600	0.588	0.733	0.670

[a]Values determined by experiment.

[b]Values calculated by characterization procedure.

[c]Calculated from experimental values for k_{xy}, k_{xz}, k_{yx}, and k_{yz}.

[d]Suspect values.

Stress Orientation of Hydrides in Zircaloy

P. L. Rittenhouse

Studies of the effects of preferred orientation (crystallographic), stress, hydrogen content, and the number of thermal cycles under stress on the directional precipitation of hydrides in Zircaloy-2 plate and sheet have been reported previously.[5–7]

The effect of cooling rate during the precipitation of hydrides is now being studied in material containing 140 ppm H_2. A stress of 20,000 psi is being used at cooling rates of 4, 12, and 170°C/min. Most of the specimens have been prepared and hydride pole figures are now being determined.

Studies of the precipitation of hydrides in the experimental lots of Zircaloy tubing being used in the biaxial stress program are under way. Specimens have been hydrided to nominal contents of 150 ppm H_2. Hydride pole figures are now being determined for those specimens allowed to cool without applied stress. Stress orientation tests are being conducted with various stress levels and states, several hydrogen concentrations, and at several cooling rates.

Studies of Zirconium Alloys in Shear

D. O. Hobson

Our investigation of the development of texture in polycrystalline α-zirconium alloys during shear[8] is being continued. Polycrystalline

---

[5]P. L. Rittenhouse and M. L. Picklesimer, The Effect of Preferred Orientation and Stress on the Directional Precipitation of Hydrides in Zircaloy-2, ORNL-TM-844 (June 1964).

[6]P. L. Rittenhouse and M. L. Picklesimer, Precipitation of Hydrides in Zircaloy-2 as Affected by Preferred Orientation, Elastic Stress, and Hydrogen Content, ORNL-TM-1239 (September 1965).

[7]P. L. Rittenhouse and M. L. Picklesimer, Fuels and Materials Development Program Quart. Progr. Rept. Sept. 30, 1965, ORNL-TM-1270, pp. 26–28.

[8]D. O. Hobson and M. L. Picklesimer, Fuels and Materials Development Program Quart. Progr. Rept. Mar. 31, 1966, ORNL-TM-1500, pp. 43–48.

specimens of zirconium, cut from the same rolled sheet but with different shear plane orientations, have been sheared various amounts and the texture produced in the shear zone examined. The four different shear orientations used are shown in Fig. 5.1 relative to the sheet texture. The nomenclature for the shear specimens uses the first letter (barred) to designate the direction to which the shear plane is perpendicular and the second letter to designate the shear direction. For example, the specimen $\overline{R}N$ was sheared on the plane perpendicular to the rolling direction in the direction parallel to the normal direction of the sheet.

In every specimen, the basal planes of the grains in the shear zone rotated so that the basal plane traces approached the plane of shear of the specimen. The starting texture of the specimen influenced the shear texture only in the amount of shear required to reach a given stage of development. The development of the shear texture as a function of the amount of shear is shown in Fig. 5.2 for a typical set of specimens. The shear direction was the normal direction of the sheet and the shear plane was perpendicular to the rolling direction. The average basal plane trace angles were determined in the center of the shear zone by polarized light microscopy using a sensitive tint plate. The average basal pole positions in the same region were determined by the polarized light method reported previously.[9]

Since the starting texture of the specimen had no effect on the final texture in the shear zone at large shears, it is difficult to postulate deformation systems that could have allowed the plastic flow to take place as it did. The orientation of the basal pole relative to the shear plane and direction, as shown in Fig. 5.2, shows conclusively that neither basal plane slip nor prism slip could have been the principal deformation system operating. Similarly, twinning on any known system or by any combination of systems could not have produced the large amounts of strain observed.

---

[9]L. T. Larson and M. L. Picklesimer, Fuels and Materials Development Program Quart. Progr. Rept. June 30, 1965, ORNL-TM-1200, pp. 36–39.

ORNL-DWG-66-6962

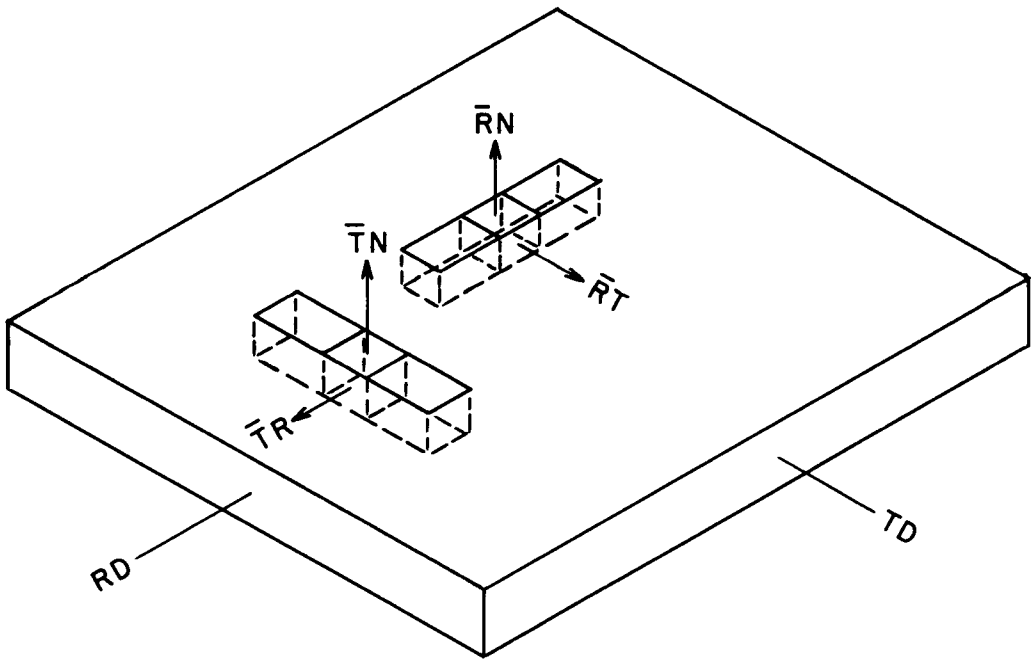

Fig. 5.1. Schematic Drawing Showing the Shear Specimen Orientations Relative to the Shear System and the Rolled Sheet. Shear system $\bar{R}N$ has the shear plane perpendicular to the rolling direction (RD) and the shear direction parallel to the normal direction (ND) of the sheet.

Since the polarized light methods can give only the orientation of the basal pole of the deformed material in the shear zone, we are modifying an x-ray procedure to give more information on the crystallographic orientations in the shear zone. The geometry of the specimen and x-ray beam in the technique are shown in Fig. 5.3. The sheared specimen will be ground flat through the two shear zones. The specimen and counter tube will be set to appropriate 2θ values and the specimen will be translated in longitudinal increments. At each longitudinal position, the specimen will be rotated in both ϕ and ω to obtain maximum diffraction intensity. This method will yield the complete crystallographic orientation of the material in the shear zone, not just the orientation of the basal pole.

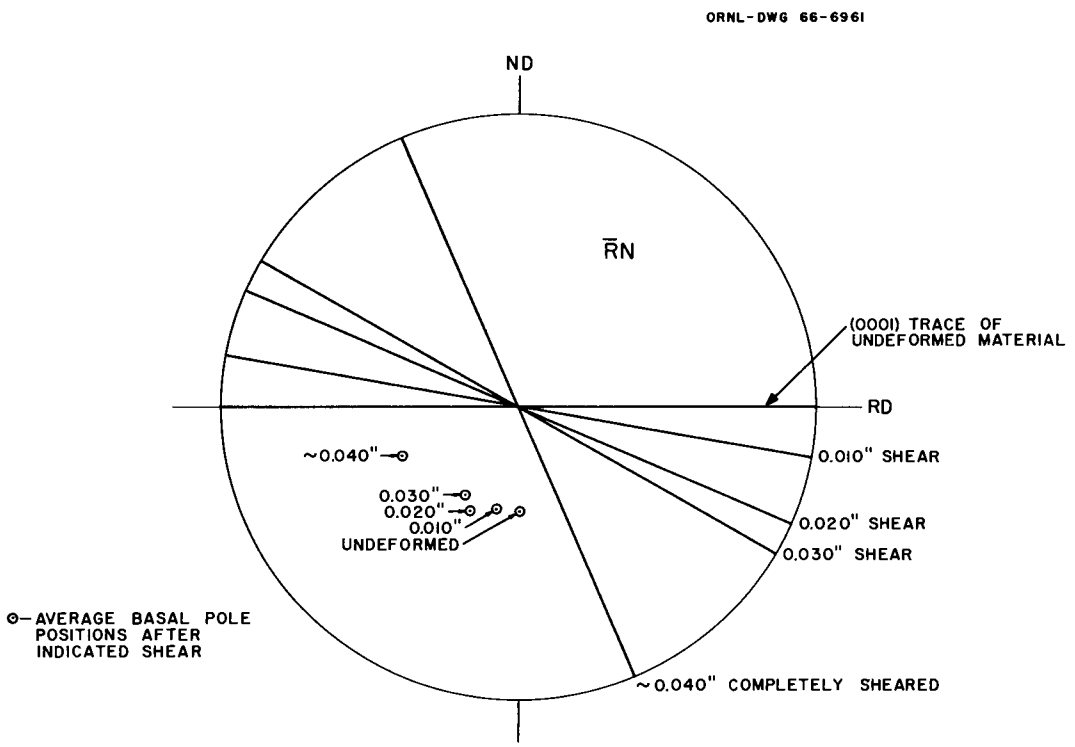

Fig. 5.2. Average Basal Plane Traces and Basal Pole Tilts for Specimens Sheared $\bar{R}N$.

Properties of High-Purity Zirconium

J. C. Wilson

Anisotropy of Oxidation of Zirconium

We are studying the anisotropy of oxidation in zirconium and hafnium as the first step in a detailed investigation of the oxidation characteristics of these metals in the high purity to ultrahigh purity state. Later investigations will include the addition of small amounts of "impurity" elements to determine their effects.

Although it has long been known that the oxidation rates of zirconium were a function of the crystallographic orientation, there are few data available on the specific orientations that produce the maximum or minimum rates of oxidation. Film thicknesses (or weight gain) have been measured as functions of crystallographic orientation by Pemsler[10] in oxygen at

[10]J. P. Pemsler, J. Electrochem. Soc. 105, 315 (1958).

ORNL-DWG 66-6963

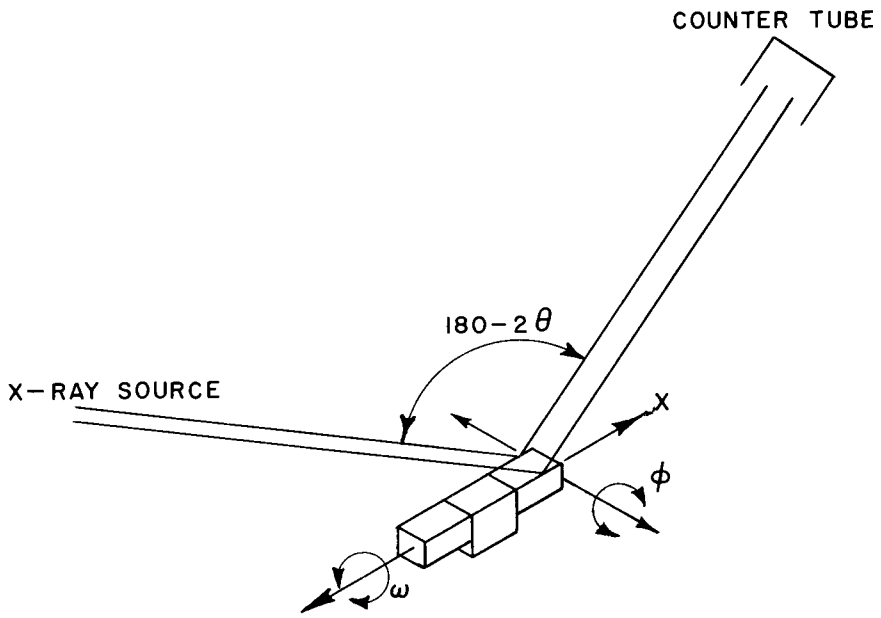

Fig. 5.3. Schematic Drawing Showing the Geometry of the X-Ray Apparatus used for Determining Crystallographic Orientations in the Shear Zone. The top portion of the specimen has been removed by grinding and polishing.

400°C, by Wanklyn[11] in 500°C steam at 1 atm pressure, and by Bibb and Fascia[12] in water at 360°C. These investigators were handicapped by problems in growing the needed crystals and only a few orientations were studied.

Single-crystal spheres allow all possible crystallographic orientations to be studied in one specimen. Using such spheres, we have shown[13] that the regions of greatest (or fastest) oxidation in zirconium can be described as bands connecting (0001) with $\langle 11\bar{2}2\rangle$, $\langle 11\bar{2}2\rangle$ with $\langle 31\bar{4}4\rangle$,

---

[11]J. N. Wanklyn, Am. Soc. Testing Mater. Spec. Tech. Publ. 358, 58 (1964).

[12]A. E. Bibb and J. R. Fascia, Trans. Met. Soc. AIME 230, 415 (1964).

[13]J. C. Wilson, Fuels and Materials Development Program Quart. Progr. Rept. Mar. 31, 1966, ORNL-TM-1500, pp. 55–57.

and $\langle 31\bar{4}4 \rangle$ with $\langle 10\bar{1}0 \rangle$ when the specimen is oxidized in air at 360 to 400°C for times up to 200 hr. These conditions correspond with those of Pemsler's experiments.

We have now obtained oxidation data on a single-crystal sphere of zirconium in 1 atm pressure steam at 500°C to supplement Wanklyn's results.[11] The regions of thicker oxide (faster oxidation rate) follow the pattern of the air oxidation results given above. After a few hours, the regions of higher oxidation rate become too dark to permit visual estimation of the thickness of oxide film from interference colors. Quantitative data must await weight gain measurements or thickness measurements by infrared spectrometry. After 20 hr, all orientations are very dark in color, but several orders of dull interference colors can be seen where the oxide film is thinnest, as shown in Fig. 5.4.

Wanklyn[11] reported that micron-size "pustules" of oxide grew on zirconium grains oriented to give low oxidation rates. He also stated that the pustules accounted for an increasing part of the weight gain after a few hours exposure at 500°C and that the grains that oxidize most rapidly at the outset apparently contribute less to the weight gain at the longer times of oxidation. Since the pustules are quite thick relative to the uniform interference color film on which they grow, the grain orientations that initially oxidize slowest contribute most to the incremental weight gain in the later stages of corrosion.

We have observed pustule formation after a few hours in steam at 500°C, as Wanklyn reported. Since our specimens are single-crystal spheres, we were able to see that the pustules have a regular external habit which is a function of the orientation of the underlying metal. Near (0001), the pustules are roughly hexagonal columns, near $\langle 11\bar{2}0 \rangle$ they are square or rectangular, and going from $\langle 11\bar{2}0 \rangle$ toward (0001) they first become trapezoidal and than kindey-shaped in cross section. The cross-sectional area of an individual pustule varies in a manner that suggests that the growth was not continuous.

Pustule formation was also observed in coarse-grained, hydrided (1000 ppm H_2) crystal-bar zirconium that was slowly cooled from the

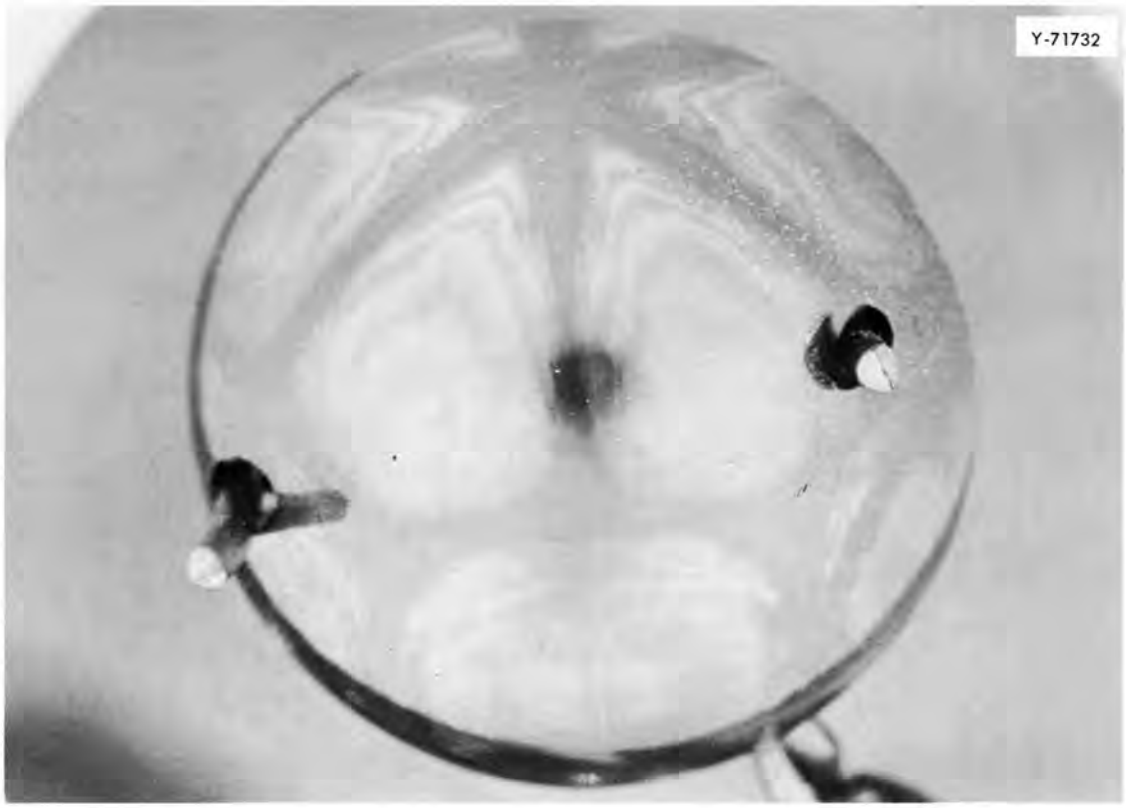

Fig. 5.4. Single-Crystal Hemisphere of Zirconium Oxidized at 500°C in 1 atm Steam. The sphere appears almost black to the eye, but several orders of dull interference colors are faintly visible as patterns in the light colored areas. The oxide pustules observed (see text) are found in the same areas. Sphere diameter is 1/2 in.

hydriding temperature. The oxide was observed to thicken where hydrides had been located prior to the oxidation. The local thickening at the hydride positions closely resembled the growth of pustules, but was on a larger scale.

Effects of Purity on the Oxidation of High-Purity Zirconium

In the first series of experiments to determine the effects of purity on the oxidation of zirconium, we have oxidized strip specimens prepared from four different regions of the same zone-refined crystal bar. The strip was recrystallized at 550°C to produce grain sizes ranging from 0.006 to 0.03 mm in diameter. All specimens were oxidized at the same time in steam at 500°C. After 24 hr., all zone-refined

specimens showed the whitish oxide that is usually associated with poor corrosion resistance. Under the same conditions, the strip from the unrefined portion of the crystal bar showed the usual blue-black "protective" oxide. Periodic observations of the specimens during steam oxidation showed that the slower oxidizing grains were eventually covered by a thicker oxide growing inward from grain boundaries or adjacent grains. Coarser grained specimens are being oxidized in steam to study the extent of this apparent lateral growth of the oxide.

Anisotropy of Oxidation in Hafnium

The first data on the anisotropy of oxidation of hafnium in air at 360°C was reported earlier.[13] The oxidation pattern on a single-crystal sphere was found to be similar to that on zirconium with the addition of two other, large, fast-oxidizing regions near $\langle 10\bar{1}2 \rangle$ and $\langle 31\bar{4}0 \rangle$ orientations. The pattern observed on a single-crystal sphere of hafnium oxidized in steam at 500°C was found to be quite similar to that in air. The pattern observed after 20 hr at 500°C in steam is shown in Fig. 5.5. If the color-film thickness relationship for hafnium oxide can be assumed to be approximately the same as that for zirconium, then the thickest film on the specimen shown in Fig. 5.5 is about 2500 A thick and the thinnest is about 1000 A thick. In contrast, the oxide film near (0001) in zirconium is approximately 2700 A thick after only 50 min in the same environment.

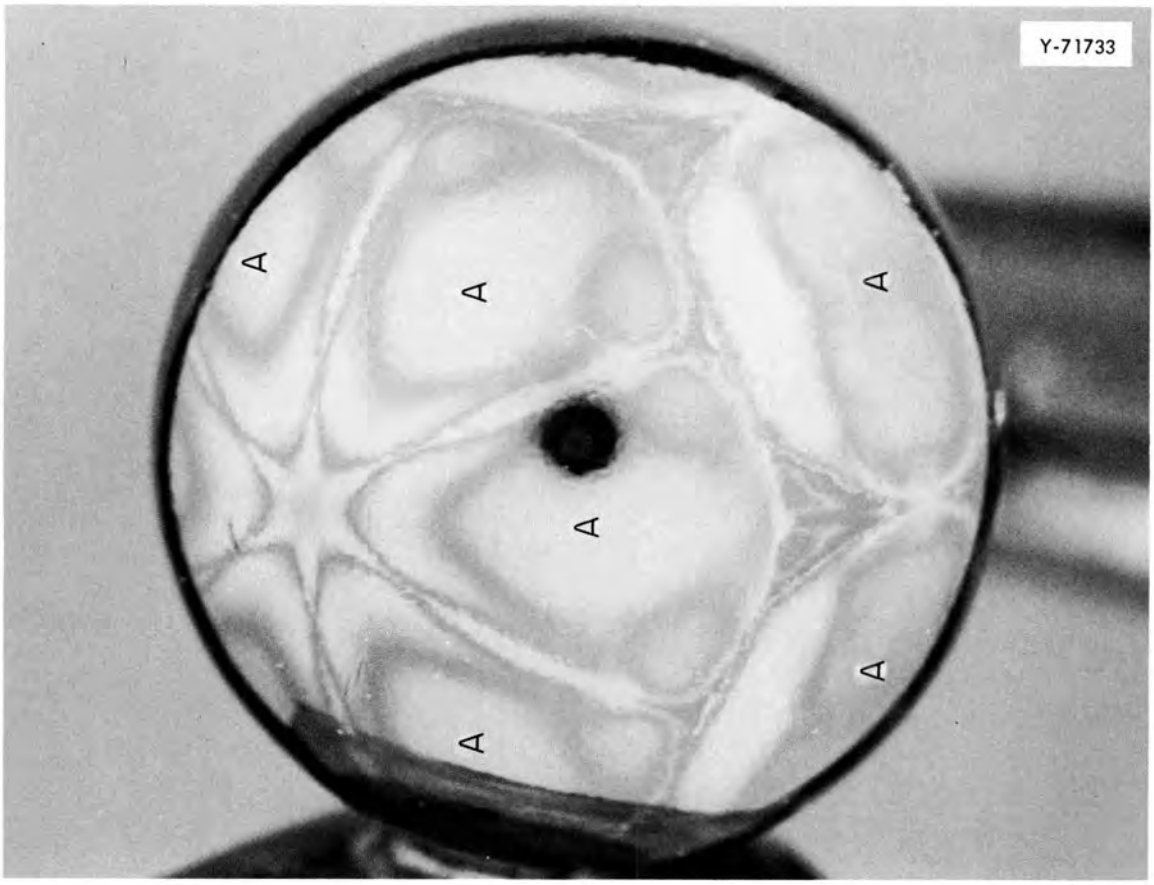

Fig. 5.5. Single-Crystal Sphere of Hafnium Oxidized 20 hr in 1 atm Steam at 500°C. The areas marked "A" are regions of more rapid oxidation that are not observed in zirconium. The "arms" radiating from the basal pole (center of six-pointed start) become progressively narrower about 20° from the basal pole; this does not happen in zirconium. Sphere diameter is 0.4 in.

6. SINTERED ALUMINUM PRODUCTS DEVELOPMENT

G. M. Adamson, Jr. D. A. Douglas, Jr.

Sintered aluminum products (SAP) material is the prime candidate construction material for the fuel rods and pressure tubes of the Heavy-Water Organic-Cooled Reactor (HWOCR). Previously available SAP exhibit erratic behavior in the form of poor process yield, structural inhomogeneity, gas fissuring and blistering, anisotropic properties, premature fracture, and low creep ductility. Since most of the erratic behavior is either process or material related, a thorough study is being conducted to determine the material and processing parameters necessary to produce a desired end product consistently and economically.

The material that follows is a brief summary of the progress on this program during the past year. In the future, this work will be reported quarterly.

Powder Characterization

R. S. Mateer[1] W. C. Robinson
W. J. Werner D. S. Cowgill[2]
C. F. Leitten, Jr.

The dual purpose of powder characterization is to develop specifications that will assure a uniform reproducible starting material and to determine powder characteristics that affect fabricability or final properties. We characterized 13 commercially available aluminum powders according to size, shape, surface area, topography, density, composition, and microstructure. The characteristics of the initial powders used in SAP were parameters usually ignored by previous researchers with the exception of Herenguel,[3] who related the subsequent SAP mechanical properties to the initial powder thickness.

---

[1]Consultant from University of Kentucky.

[2]On loan from Atomics International.

[3]J. Herenguel and J. Boghen, "Propriétés des demi-produits en aluminum Fritté," pp. 341–46 in Congrès International de L'Aluminum, VI, Paris, June 14–19, 1954, Malescherbes, Paris, 1955.

Atomized powders have the characteristics of chill castings of very fine structure, while the flake materials have a highly recovered or recrystallized structure with low dislocation density. Both flake and atomized powder show unusual resistance to softening (measured by microhardness), and these powder characteristics may be directly related to the elevated-temperature behavior of wrought SAP. None of the powders examined has been specifically treated by the manufacturers for the purpose of fabricating SAP. Therefore, a prime objective of the SAP program is to determine optimum methods for increasing the oxide content and controlling morphology.

Fabrication steps employed following material characterization are delineated in the flowsheet shown in Fig. 6.1. Operations performed in each step are covered in the following sections.

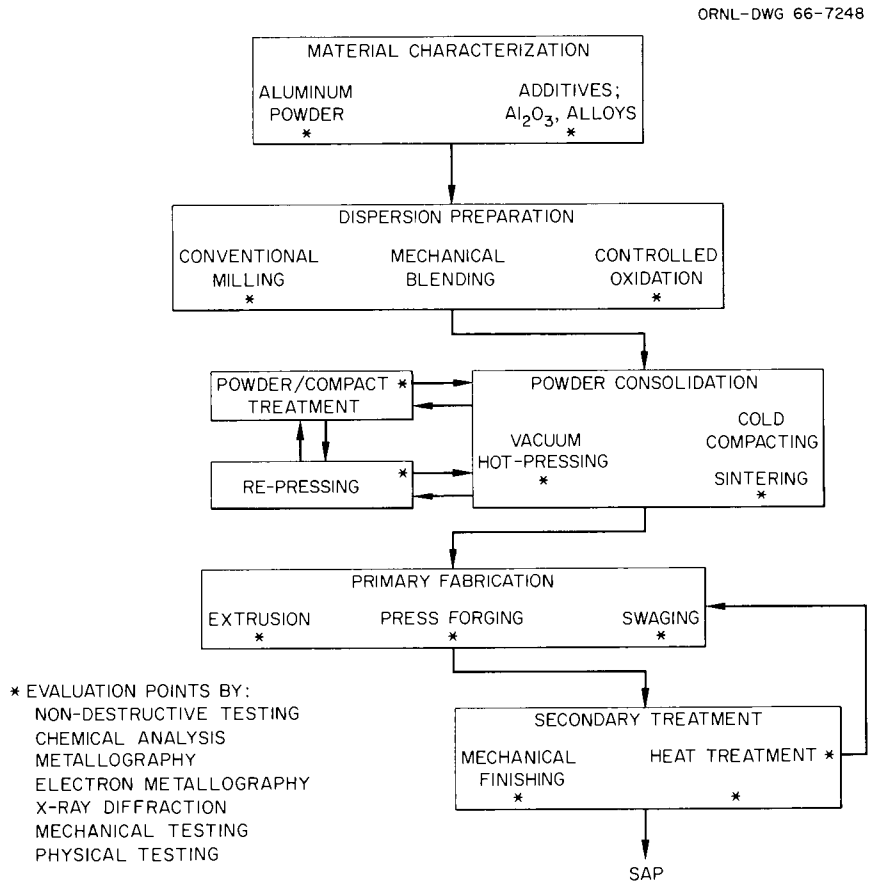

Fig. 6.1. Flowsheet for Sintered Aluminum Products.

Dispersion Preparation

G. L. Copeland R. L. Heestand
W. J. Werner C. F. Leitten, Jr.

We are seeking a procedure that will produce a flake product of controlled oxide content and thickness with a minimum of contamination. Starting materials have been commercial high-purity partially spherical atomized powders with nominal sizes of 3 to 15 μ. Aluminum and stainless steel mills have been used with aluminum or stainless steel balls with and without internal lifter bars. Lubricants have been stearic acid, oleic acid, and dimethyl silicone fluid with Varsol as the milling vehicle; a wide range of proportions and amounts of these materials has been studied. All milling has been done in air with no attempt to control temperature (< 35°C). Milling times ranged from 5 to 72 hr and milling speeds from approximately 30 to 100% of the speed of maximum energy input (just short of centrifuging). Milling conditions of some typical batches are given in Table 6.1.

Internal lifter bars increase the reproducibility of the process and increase the milling action, thus decreasing the time required to produce a given oxide content. The use of stainless steel rather than aluminum balls required approximately one-third less time and gave a more reproducible product. Under constant milling conditions, the reproducibility of the oxide contents produced with steel balls and internal lifter bars was within the reproducibility of the chemical analysis for oxide content. Spectrographic analysis indicated no additional iron contamination from the use of type 302 stainless steel mills and balls over that from the use of an all-aluminum mill.

Stearic acid appears to be preferable to oleic acid in that it produced a lower oxide content for a given surface area (and flake thickness), thus giving a closer interparticle spacing for a given oxide content. The flake powders produced with these lubricants contained around 1% C with 2 to 3% total organic material and produced extruded rods with less than 0.5% C. The silicone fluid produced a still lower oxide content for a given flake thickness, but the silicone is more difficult to remove from the powders. Typical batches contained

Table 6.1. Conditions of Typical Ball-Milling Experiments

Grinding Medium	Lubricant Type	Lubricant Amount (% of powder)	Amount of Varsol (ml)	Milling Time (hr)	Product Analysis, % Al_2O_3[b]	Product Analysis, % Carbon[c]
Stainless Steel	Stearic Acid	3	500	9	9.33	1.4
Stainless Steel	Stearic Acid	3	500	7	8.73	
Stainless Steel	Stearic Acid	3	500	6	7.49	
Stainless Steel	Oleic Acid	3	500	7	9.77	1.3
Stainless Steel	Silicone Fluid	63	None	7	6.90	8.2
Stainless Steel	Silicone Fluid	63	300	7	12.8	
Stainless Steel	Stearic Acid	1.25	375	7	6.92	1.8
Aluminum	Stearic Acid	1.25	375	7	2.76	0.9
Aluminum	Stearic Acid	3	500	7	2.25	0.8

[a] For 300 g powder.

[b] Average of several batches in most cases.

[c] These powders after vacuum treatment produce extruded rods containing 0.1–0.5% C.

approximately 2% C with approximately 4% total organic. Chemical analysis results of these powders after vacuum compacting and extrusion are not available at this time.

Two distinct types of inclusions have been noted in rods produced from commercial ball-milled flake powder; one is metallic or alloy-like in appearance and the other is ceramic-like in appearance. Microprobe analysis indicated that the "metallic" inclusions consist of iron, iron-aluminum, or iron-aluminum-oxygen. The ceramic inclusions seem to be aluminum carbide, probably Al_4C_3. The particles of almost pure iron indicate a pickup during commercial ball milling in steel mills. Some small iron-containing inclusions are present in atomized powder. The carbide is probably a result of carbon pickup from the milling. Rod produced from ORNL ball-milled flake showed considerably fewer and smaller metallic inclusions than commercial alloys.

Aside from the reduction in the metallic inclusions, the ORNL flake appears similar to commercial products. Nominal flake is produced with thicknesses near 0.5 μ and oxide contents from 1 to 35%. Transmission electron microscopy reveals a recrystallized structure in the flake immediately after ball milling with no evidence of tangled dislocation cells but consisting of well-defined grains with a diameter of approximately 0.5 μ.

It would be desirable to obtain the desired oxide content by blending to avoid contamination during milling. Materials used thus far have been Linde B (0.05-μ γ-alumina) blended with commercial high-purity atomized aluminum powder in the nominal size range 3 to 10 μ. In all tests to date, the oxide has been agglomerated, producing an inhomogeneous mixture. Additional studies on dispersing oxides are under way.

A limited amount of effort was devoted to controlled oxidation of spherical aluminum powders by reaction with water, using both large quantities of distilled water and limiting the time of exposure to control oxide content and by adding small quantities of water to yield a high moisture content before reaction. The latter method offered more successful control with levels up to 6% oxide; however, the alpha monohydrate is in the form of fanlike crystals, and smaller aluminum

particles are completely consumed to oxide. As an alternate route, we are studying high-temperature oxidation, wherein gamma oxide may be formed directly by exposure of the powder to oxygen at low pressures.

Powder Consolidation

G. L. Copeland D. L. Cowgill[4]
C. F. Leitten, Jr.

A second major deviation from past practice in the manufacture of SAP is our substitution of vacuum for air during the conversion of the oxide hydrate to anhydrous oxide. We felt that the use of flake powders and a vacuum out-gassing treatment would prevent the formation of large oxide agglomerates in the consolidated product. Our studies show that both are essential and serve to provide a homogeneous distribution of fine stable oxide particles.

Vacuum hot pressing has been done in graphite dies at pressures from 1.6 to 2.6 tsi. The procedure includes holding the powder at 600°C for 2 hr under vacuum, then pressing for 30 min at 600°C under vacuum. This procedure produces compacts with density greater than 95% of theoretical. The final density is independent of pressing load in the range tested. This procedure is sometimes followed by coining at 50 tsi at room temperature, which yields close to theoretical density.

Compacts have been cold pressed at pressures of 20 to 45 tsi. This is followed by a vacuum anneal at 600°C for 20 hr. The compacts are then coined at room temperature at 50 tsi. Final density, generally 94 to 99% of theoretical, does not depend on the initial pressing pressure in this pressure range.

There has been considerable controversy whether the oxide phase was continuous or discontinuous. The morphology of the oxide phase can be varied from a continuous oxide network in the aluminum matrix to discrete oxide particles in the metal matrix by proper selection of outgassing and compaction parameters. A 20-hr vacuum anneal at 600°C, whether of the powder or of the compact after pressing, is sufficient

---

[4]On loan from Atomics International.

to stabilize 6 to 9% oxide and prevent agglomeration during extrusion. The 2.5-hr anneal during vacuum hot pressing is insufficient to prevent agglomeration of the oxide during extrusion. Further work in this area is in progress.

Fabrication

G. L. Copeland
D. S. Cowgill[4]
W. J. Werner
C. F. Leitten, Jr.

The prepared SAP powder is being fabricated by swaging and extrusion to determine the effects of working on the material and to provide specimens for mechanical property measurement, nondestructive testing, and physical metallurgical evaluation.

Swaging

Some XAP-001 rods were hot swaged at 500°C for subsequent tensile tests. Creep-rupture strength appears to be improved by hot swaging.

Hot swaging was used to fabricate 20 compacts including flake, spherical, and blended powders. All swaging was done at 500°C starting temperature, and the first 10% reduction was in Inconel sheathing to provide suitable size for swaging and to prevent spalling from the compacts. Some tests were made using aluminum sheathing, but the sheathing ruptured before sufficient reduction was obtained. All swaged rods attained greater than 98% of theoretical density and showed no strong orientation metallographically. X-ray diffraction, however, revealed distinct ⟨100⟩ and ⟨111⟩ fiber texture of the aluminum.

Cold swaging and wire drawing were used to produce 0.010-in.-diam wire for x-ray analyses. In 1% oxide material no intermediate annealing was required, but in 6% oxide material several intermediate anneals were required. In 6% oxide dispersions 0.030-in.-diam wire could be cold drawn.

Extrusion

Several compacts were extruded as the cores of type 6061 aluminum billets. Extrusion at ratios of 10, 20, and 30 at 500°C was used to

evaluate the effects of starting density and reduction ratio on final density and to provide material for mechanical testing and annealing studies.

Primarily compacts were extruded bare, using shear dies in the 500-ton laboratory extrusion press. Reduction ratios of 10, 20, and 30 at 400, 500, and 600°C were used to prepare samples for mechanical testing. Even though all extruded rods were greater than 99% of theoretical density, some increase in tensile ductility and strength was found with increasing reduction ratio. Temperature effects have not yet been defined.

Extrusion experiments indicated that density is an inadequate measure of primary fabrication effectiveness, since essentially full density is achieved when reduction ratio is 10 or greater, starting density is 70% or greater, and temperature is 400°C or greater. Also, SAP rod is readily extruded with 80 to 90% recovery with standard tooling and fairly low loads.

Evaluation of Materials

All of the standard evaluation techniques were applied to the SAP produced and procured by ORNL. These techniques include metallography, electron microscopy, x-ray diffraction, radiography, microprobe analysis, chemical analysis, and mechanical properties evaluation.

X-Ray Diffraction (W. C. Robinson, J. E. Spruiell,[5] R. S. Mateer,[6] and C. F. Leitten, Jr.)

The x-ray diffraction line-broadening technique was used to determine grain size in the initial powders and the fiber textures of both swaged and extruded SAP rods. The reduction ratios were 15.7 for the swaged rods and 20 for the extruded rods. The swaged SAP rods

---

[5]Consultant from the University of Tennessee.

[6]Consultant from the University of Kentucky.

had a duplex aluminum fiber texture consisting of ⟨111⟩ and ⟨100⟩ components, while extruded flake material had only a ⟨111⟩ component. The texture of extruded rods is much stronger than that of swaged rods.

X-ray diffraction also has been applied in the determination of the type of oxide present in the fabricated SAP rods and on the powder after various processing steps. The problem is particularly difficult because of the existence of numerous oxides and hydrates, the small amount of oxide present in most SAP materials, and the extremely fine size and homogeneous distribution of the oxide particles. It has not been possible to identify with certainty the oxide species present in the SAP materials. The difficulty appears to be due to the simultaneous existence of several oxide species and small amounts of aluminum carbide.

Metallography and Electron Microscopy (W. C. Robinson, K. Farrell, and G. L. Copeland)

Metallographic examination of commercial SAP reveals oxide agglomerates arranged in "stringers," which run parallel to the extrusion direction. Electron photomicrographs revealed that these oxide agglomerates were as large as 4 μ in diameter and bordered areas of oxide-free aluminum. Light microscopy is insufficient to resolve the oxide phase in SAP prepared directly from ORNL flake, from nontreated atomized powder, or in XAP-005, an Alcoa product. The difference in the type of oxide dispersions obtained by these products and other commercial materials is illustrated in Fig. 6.2 which shows electron micrographs of an ORNL SAP and SAP-ISML 930.

The agglomeration of oxide that occurred during blending studies at ORNL could be observed by metallographic examination. Metallographic examination was used also to check for macroscopic porosity and to observe inclusions, which were subsequently examined by microprobe analysis.

Electron microscopy was used to examine flake powders in the initial powder characterization and later to examine flake prepared at ORNL. Flakes stored in liquid nitrogen immediately after milling had well-defined grains with a diameter of about 1/2 μ. Since there was

ORNL SAP (Sintered Aluminum Products)
6% Oxide 25,000 X

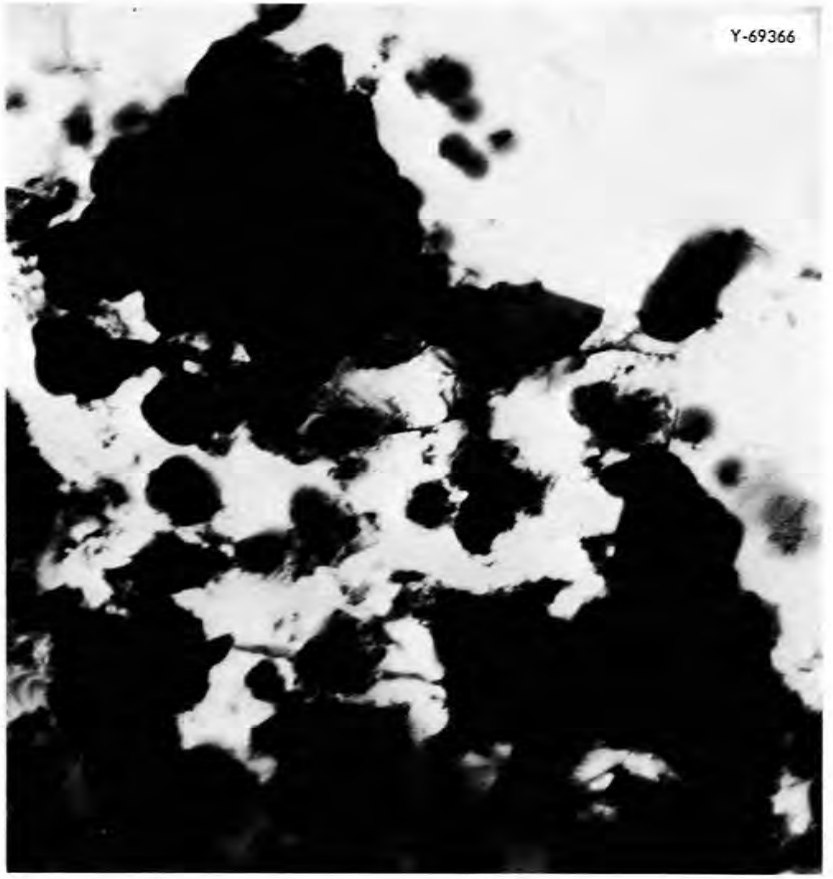

COMMERCIAL SAP ISML 930
7.8% Oxide 25,000 X

COMPARISON OF ORNL SAP AND COMMERCIAL ISML-930

Fig. 6.2. Microstructures of ORNL Sintered Aluminum Products and Commercially Produced SAP.

no evidence of tangled dislocation cells characteristic of the cold-worked state, the flakes had undergone extensive recovery or recrystallization during the ball-milling operation. Since considerable difficulty was encountered in obtaining consistent reliable oxide analysis of SAP materials, chemical analysis is currently not used as a process control. More accurate techniques are being studied.

Nondestructive Testing (R. W. McClung)

The nondestructive testing phase of the program is intended to develop necessary methods, techniques, and equipment to evaluate SAP materials at various stages of fabrication. Thus, it will be beneficial during the material development stages as well as applicable to evaluation of finished products.

At the beginning of the program several small pieces of SAP materials were received from Atomics International. The shapes included billets, pressure tubing, and finned tubing. The preliminary investigations were to determine applicability of existing techniques to these items. Ultrasonic techniques seem to be applicable with a sensitivity range similar to that for wrought aluminum. Figure 6.3 shows an annular discontinuity detected near the surface of a 2-in.-diam billet. This was associated with inhomogeneities such as are shown in Fig. 6.4. Low-voltage radiography[7] was applied to detect discontinuities, low-density areas, and high-density inclusion. Liquid-penetrant techniques are applicable to all shapes, and eddy currents have been investigated for inspection of the finned tubing. Conventional encircling-coil eddy-current practice seems to be applicable and sensitive to linear cracks, inclusions, and voids. Figure 6.5 shows discontinuities detected in finned tubing. Advanced technique development using the phase-sensitive eddy-current instrument[8] is under way for more sensitive detection of flaws and measurement of wall thickness.

---

[7]R. W. McClung, "Techniques for Low-Voltage Radiography," Nondestructive Testing 20(4), 248–53 (1962).

[8]C. V. Dodd, A Solution to Electromagnetic Induction Problems, ORNL-TM-1185 (August 1965).

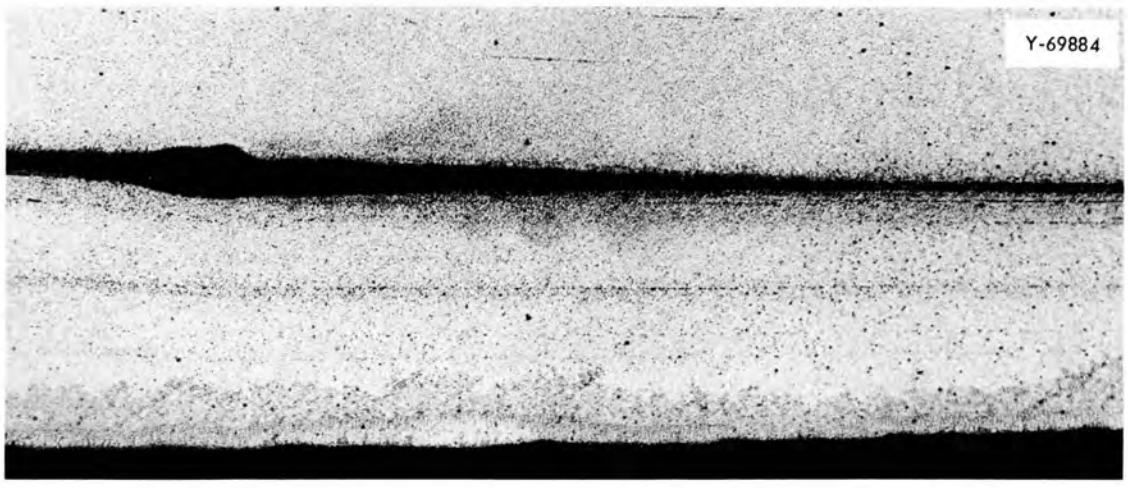

Fig. 6.3. Annular Flaw in a 2-in.-diam SAP Billet. 100×.

Fig. 6.4. Inhomogeneities in a 2-in.-diam SAP Billet.

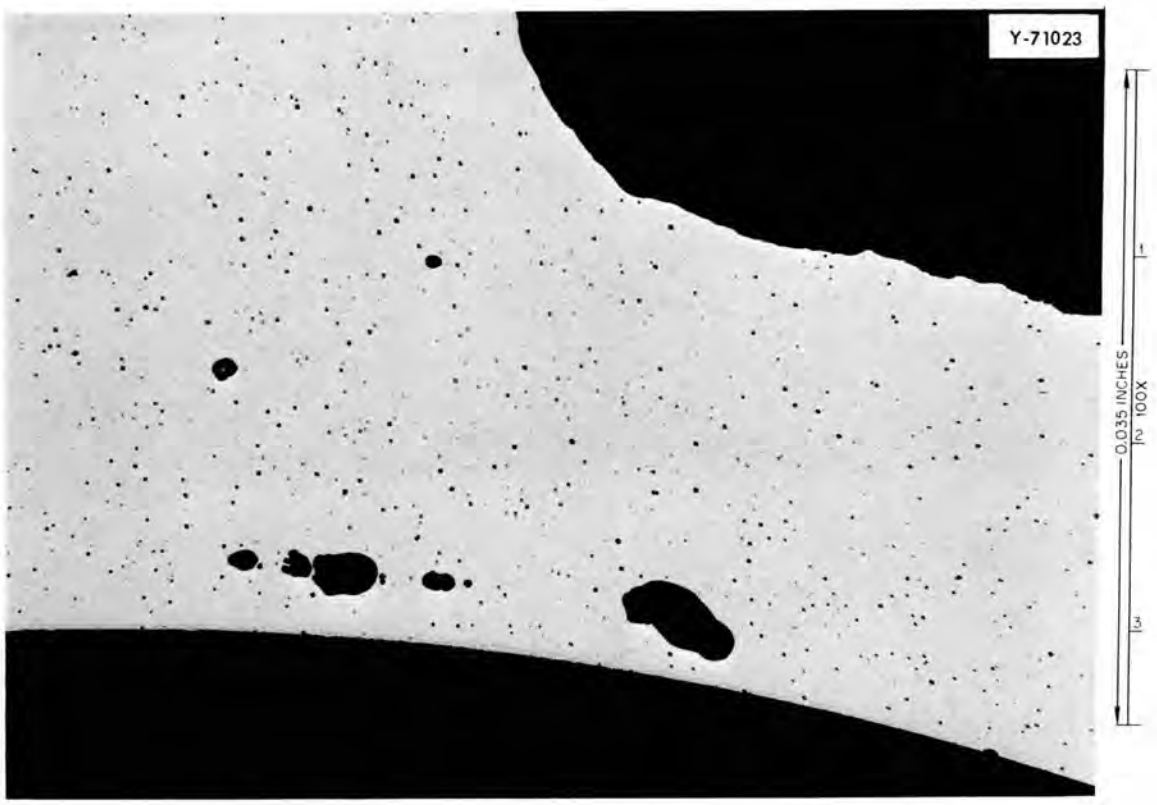

Fig. 6.5. Flaws Detected by Eddy Currents in SAP Finned Tubing.

Since processing of SAP materials has begun at ORNL our emphasis has changed to development of methods of process control. Included among the problem areas are measurement and classification of the submicron particles and determination of the oxide content in both powder and billet forms. We are currently surveying commercial equipment capabilities for particle sizing to determine potential applicability and areas in which work needs to be done. Preliminary work has indicated that eddy currents can measure oxide content in the hot-pressed billets. Figure 6.6 shows the relative electrical resistivity as determined by eddy currents on several samples. Extensive calibration will be required for this technique and differentiation must be made for the response due to density variations.

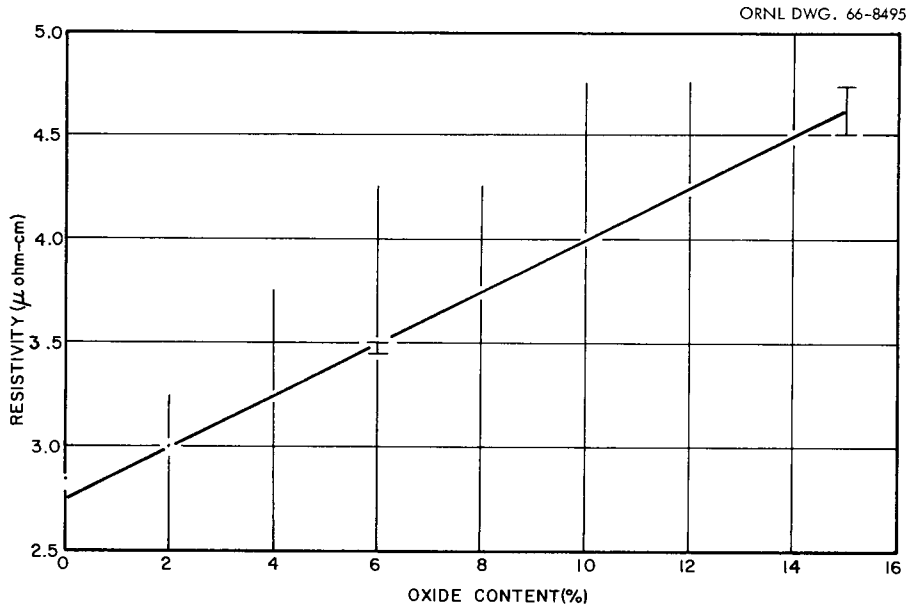

Fig. 6.6. Variation in Electrical Resistivity with Oxide Content in a SAP Billet as Determined by Eddy Currents.

Mechanical Properties Evaluation (D. G. Harman and K. Farrell)

Our mechanical properties investigations regarding the SAP program can be stated as three major efforts. First, we have under way general deformation studies on both commercial and experimental materials. Second, we are evaluating the effects of material and process parameters on the strength properties of our experimental SAP. Third, because of its relative importance, we are pursuing extensive fractographic analysis by replicating and then photographing the fracture surfaces of failed test specimens.

Our general deformation program has led to a better appreciation of the behavior of SAP under various testing conditions. One observation is the effect of extrusion ratio as shown by our own data as well as that of Atomics International.[9] The higher extrusion ratio improves the strength and ductility to some extent. Another important finding has been the strain-rate dependence of mechanical properties at high temperatures. As a matter of fact, much of the relatively large scatter

[9]D. B. Ferry, Effects of Fabrication on the Mechanical Properties of SAP, AI-CE-1032 (Jan. 11, 1966).

in reported SAP data can be attributed to differences in testing conditions. Figure 6.7 shows our data on commercial XAP-001 superimposed on a scatter band obtained from the literature.[10–18] The change in strain rate from 0.2 to 0.002 min^{-1} has a large effect on high-temperature properties and covers a good portion of the scatter band. A strain-rate dependence is not unique to SAP but is significant for many alloy systems, including austenitic stainless steels and nickel-base superalloys.

The strain rate $\dot{\epsilon}$ in SAP is an exponential function of the stress σ: $\dot{\epsilon} = A\,\sigma^n$. This relationship gives a straight line with slope n on log-log coordinates, as shown in Fig. 6.8. The filled symbols represent 450°C data on an experimental 5% oxide material; the filled triangles are tensile data at three strain rates and the filled

---

[10]E. A. Bloch, "Dispersion-Strengthened Aluminum Alloys," Met. Rev. 6(22), 193–239 (1961).

[11]R. J. Towner, Alcoa's APM Alloys, ALCOA Research Laboratories, New Kensington, Pa., Sept. 15, 1960.

[12]E. G. Kendall and W. H. Friske, "Fabrication and Properties of APM Products," Met. Soc. Am. Inst. Mining, Met. Petrol. Engrs., Inst. Metals Div., Spec. Rept. Ser. 10, 39–45 (1960).

[13]D. G. Boxall and S. Mocarski, The Present Status of SAP in the Canadian Organic Cooled Reactor Program, R61CAP30, Canadian General Electric (June 1961) (limited distribution).

[14]D. M. Guy, Alcoa's Aluminum Powder Metallurgy (APM) Alloys, Alcoa Green Letter, ALCOA Research Laboratories, New Kensington, Pa., March 1959 (not released for publication).

[15]W. H. Friske, Interior Report on the Aluminum Powder Metallurgy Product Development Program, NAA-SR-4233 (1960).

[16]N. Hansen, Tensile Properties at Room Temperature and at 400°C of Commercial Sintered Aluminum Products, Risö-96 (December 1964).

[17]Atomics International, SAP Materials Handbook, AI-CE-Memo-24 (Mar. 23, 1966).

[18]D. G. Boxall and J. W. Standish, Mechanical Properties of Dispersion-Strengthened Aluminum Alloys, AECL-1532 (January 1962).

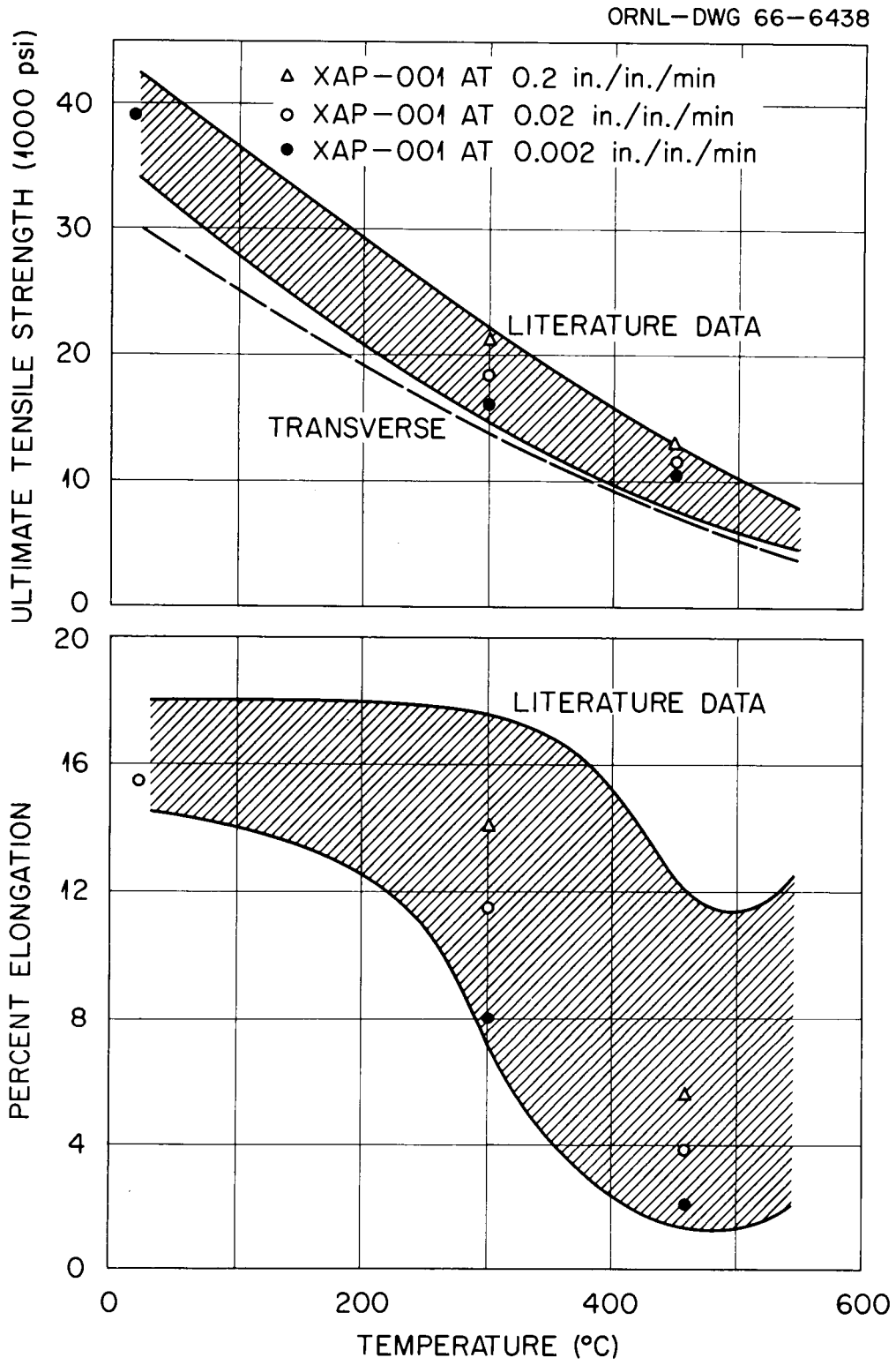

Fig. 6.7. Short-Time Tensile Strength and Ductility of XAP-001.

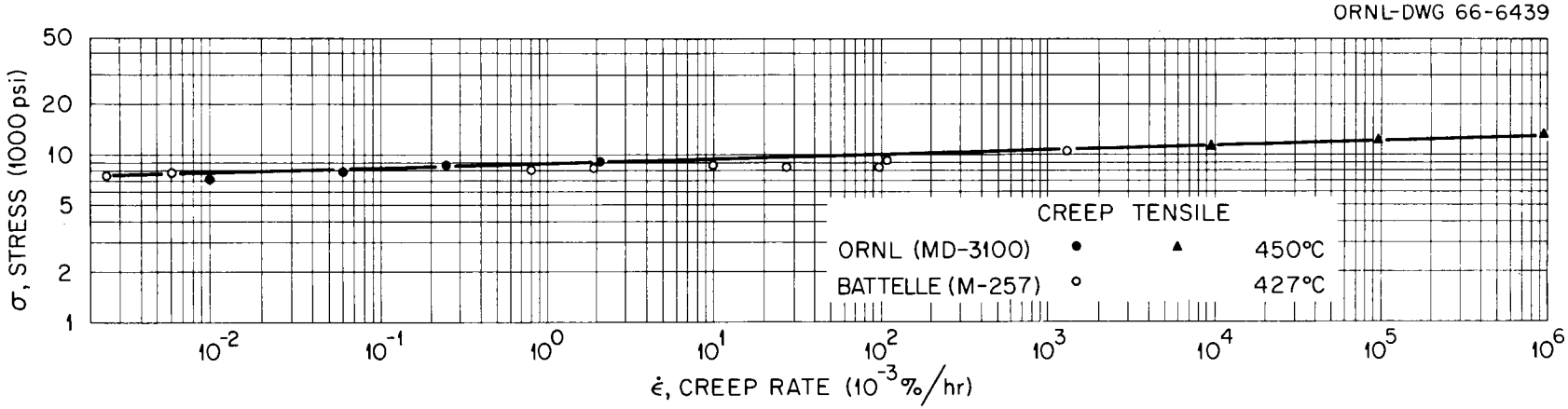

Fig. 6.8. Stress vs Creep Rate for Two Sintered Aluminum Products.

circles are creep rates. The open circles are Battelle data[19] on XAP-001 (previously called M-257) at 427°C. The straight line drawn through the data has a slope of 40. This value of n is unusually high; TD nickel has also shown this high n value.[20]

This very high value for n is significant in both the tensile and creep situations. Any small amount of area change during a tensile test, by internal voiding or tensile necking, gives rise to locally increasing strain rates, which result in curtailed total elongation. Figure 6.9 shows the local neck observed for a high-temperature tensile test.

The high n value affects the creep test by the curtailment of third-stage creep. At the termination of second-stage or linear creep some slight reduction in cross-sectional area has occurred either through actual necking or more likely through internal void formation. Because the load on the specimen is remaining constant this reduction in area increases the stress level. As previously pointed out because of the high n value, only a small increase in stress provides a significant increase in strain rate, which causes immediate rupture via high-strain-rate shear. This type of rupture is shown in Fig. 6.10. Here we see essentially no necking on the portion that failed by the growing and linking of the internal voids, a process commonly called ductile tearing. A good deal of necking is seen on the portion that failed by the high-strain-rate shear.

The observations just described and other observations have led to a procedure for the evaluation of any particular experimental SAP rod with a given powder and fabrication history. Because of the limited amount of material available per SAP rod we are using the small button-head specimen design that has been so successful for our irradiation damage studies. Each specimen requires only 2 in. of rod length. To

---

[19]J. A. Van Echo and S. W. Porembka, Long-Term Creep Rupture of Sintered Aluminum Powder and Zircaloy-2 Alloys, BMI-X-10 113 (Jan. 25, 1965).

[20]L. P. Rice, Metallurgy and Properties of Thoria-Strengthened Nickel, DMIC-210 (Oct. 1, 1965).

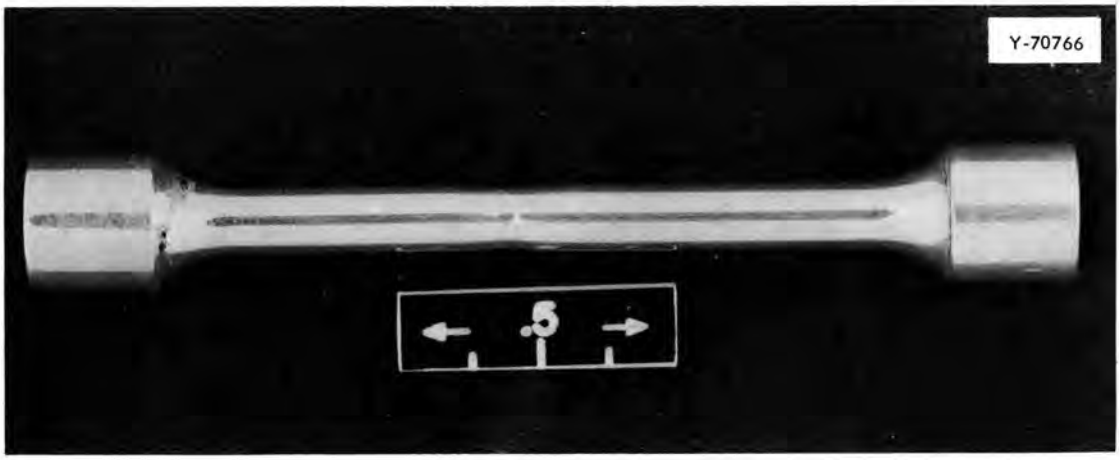

Fig. 6.9. Interrupted 450°C Tensile Test on XAP-001 Showing Local Necking Just Prior to Rupture. Specimen was electropolished before test.

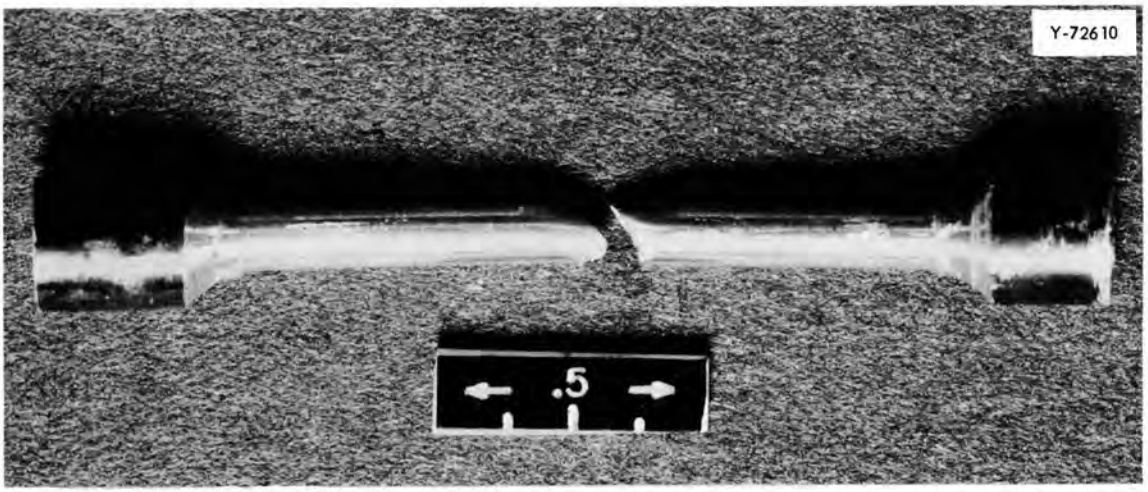

Fig. 6.10. Creep Rupture of XAP-001 at 450°C Showing Local Necking at Shear Lip. No neck is evident on that portion that failed by tearing.

date tensile testing coupled with a modest creep testing schedule has been adequate for the qualitative comparison required. More extensive testing will be added as the field of candidate materials is narrowed. At least four tensile tests are performed on each rod: one tensile test at room temperature for base-line comparison and at least three tensile tests at 450°C covering a wide range of strain rates. This strain rate variation not only provides good tensile data but also allows one to predict the long-time stress-rupture behavior.

This stress-rupture treatment of tensile data is shown in Fig. 6.11. Plotted on log-log coordinates is the applied stress vs the time to rupture. This particular stress-rupture plot is for one of our MD-3100 rods with 5% oxide tested at 450°C. The open circles are the ultimate tensile strength plotted against the total test time, while the filled circles are actual dead-load stress-rupture tests. One can see the good prediction made by the extension of the tensile data. Data like these have been collected on many of the experimental alloys, including all of the powders being considered and with many process variables already being evaluated. Oxide contents have ranged from 1 to 10%. High-temperature—low-strain-rate ductility has ranged from less than 1% total elongation for the higher oxide contents to as high as 17% for the lower oxide contents.

Another very important aspect of SAP behavior is the mode of fracture. Perhaps our most startling finding has been that under all testing conditions, including high-temperature creep, SAP fracture in a very ductile manner. This ductility is confined to a small portion of the specimen and thus provides very little overall extension.

Ductile fracture is generally categorized as separation, tearing, or shear. All three of these modes have been found in SAP. Figure 6.12 shows typical low-temperature and high-temperature fractographs. The actual fracture surfaces of the specimens were replicated with a plastic film and subsequently viewed and photographed in the electron microscope. The very fine-scale low-temperature fractures are in contrast to the coarser high-temperature fractures. We now have very good evidence that these high-temperature voids, which initiate fracture, form very early in the tensile test at strains as low as 0.5% and that fracture

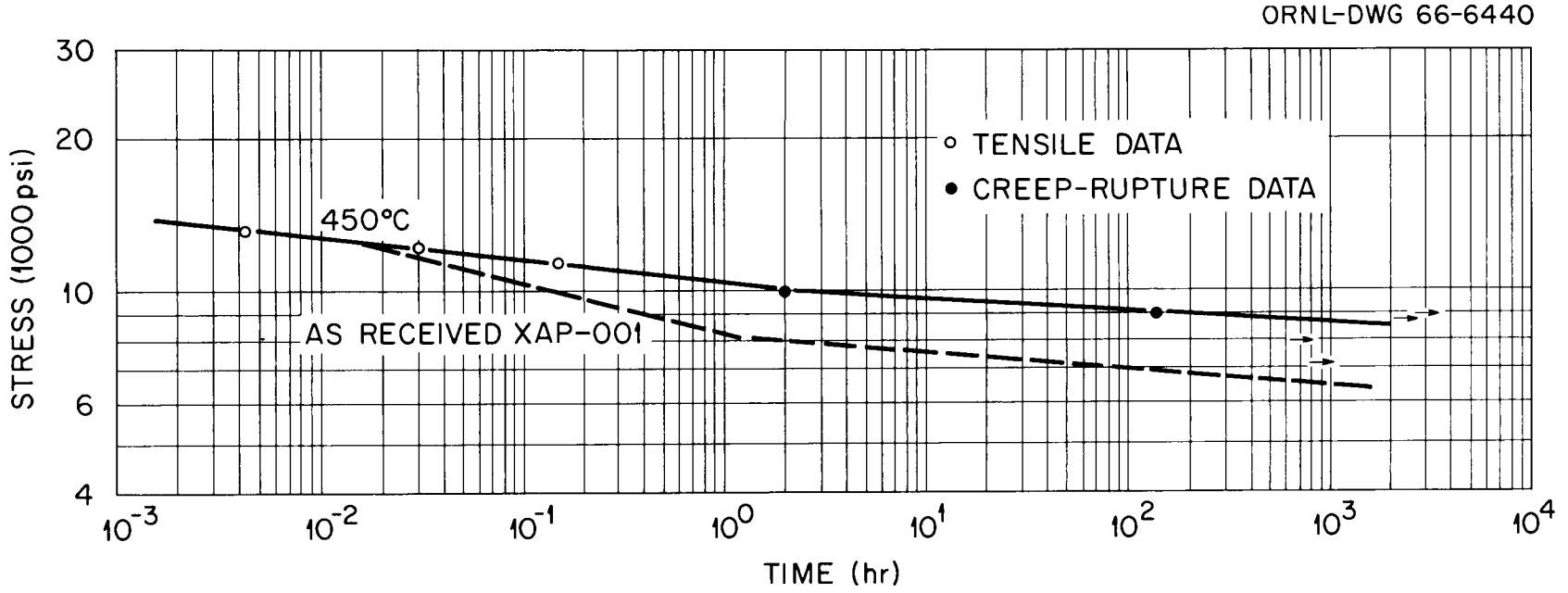

Fig. 6.11. Stress Rupture of SAP 37 (MD-3100) at 450°C.

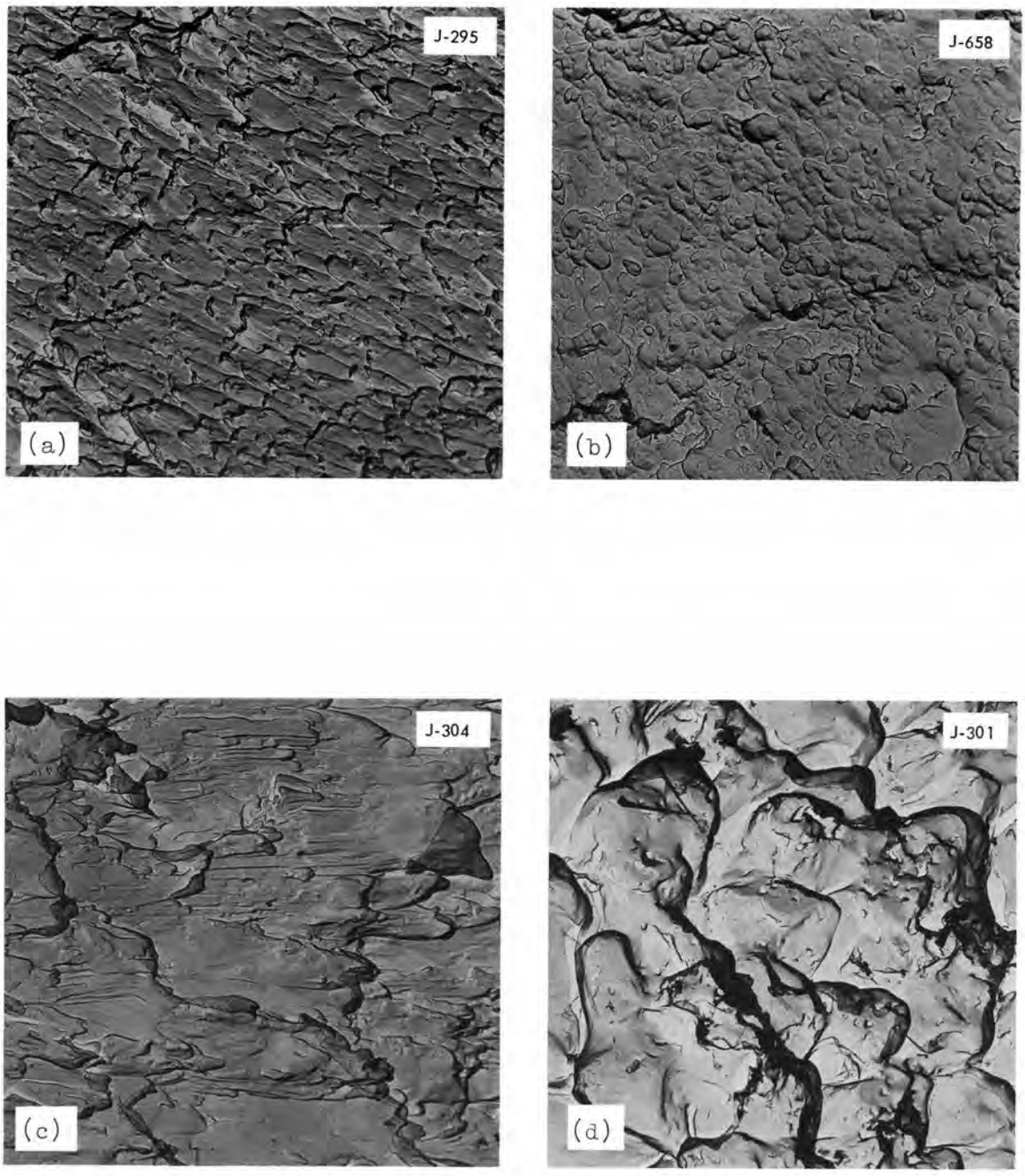

Fig. 6.12. Fracture of Experimental SAP. (a) Room-temperature shear. 6500×. (b) Room-temperature tearing. 6500×. (c) 450°C shear. 8000×. (d) 450°C tearing. 6500×. Replication and fractography by T. A. Nolan, Physics Department, ORGDP.

initiates at the aluminum-Al_2O_3 boundary. The room-temperature shear fractographs are being used routinely to show the oxide distribution within the material. Another technique being used is to anodize the fracture surface for direct replication. Figure 6.13 shows an anodized high-temperature fracture. The platelets of oxide can be seen over the entire surface and are now available for further study, including diffraction analysis and stereophotography.

Another method of fracture analysis that is being used involves conventional microscopy. Examination of tested creep specimens has revealed two types of voids in commercial and experimental SAP. The first type is found only in the gage length near the point of fracture. These voids are rounded, tend to be interconnected parallel to the fracture face, and are connected with the tensile dimples in the fracture process. The second type of void occurs even in the heads of specimens and is elongated in the extrusion direction. Such voids appear on heating alone but grow under an applied load. In some cases, these voids link up to form radial fissures. The relationship between the two types of observations and the fracture process has not been established.

Discussion of Results

The SAP investigation has progressed sufficiently so that we will be able to write detailed specifications for the production of a consistent, economical material within the next year. The material produced by these specifications should be as good as the best presently available from any known commercial vendor. Sufficient data are available to enable us to control the oxide content to within 0.5% Al_2O_3 with any of the three investigated lubricants. The resulting flake can be compacted to greater than 95% of theoretical density by methods involving either hot or cold pressing. Finally, the existing extrusion facilities with standard tooling were sufficient to produce rods up to 1/2 in. in diameter without difficulty.

A large amount of basic information has also resulted from the program. The compositions of the inclusions in the fabricated product

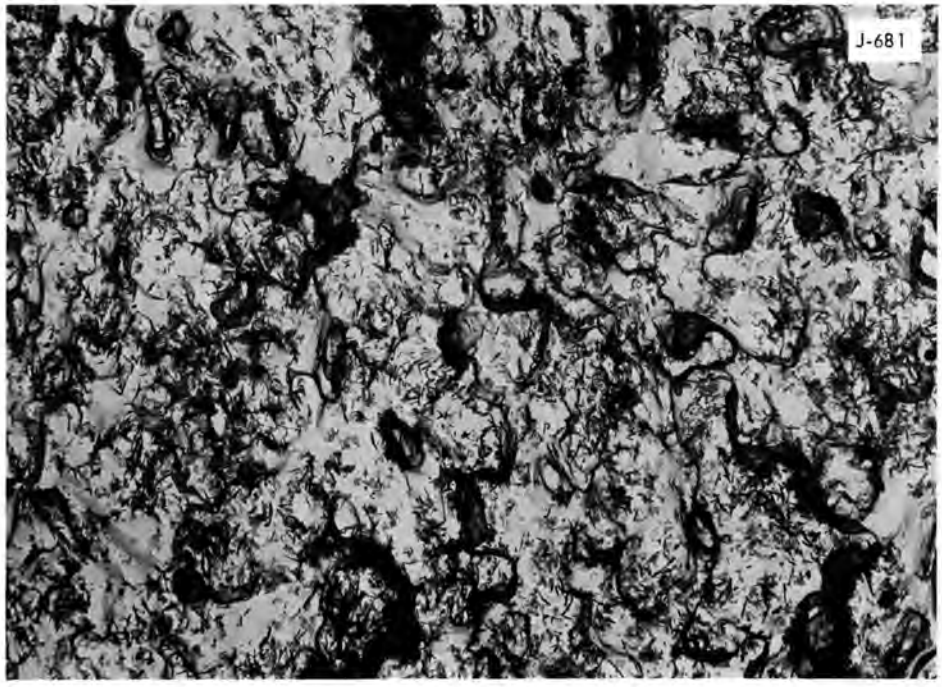

Fig. 6.13. Direct Replication of Anodized Fracture Surface of Experimental SAP Tested at High Temperature. Black needle-shaped particles are oxide platelets viewed on edge. Replication and fractography by T. A. Nolan, Physics Department, ORGDP. 6500×.

have been identified. The atomized powders have been shown to be chill castings of very fine structure. Controlled oxidation of these atomized castings has been difficult because all commercially atomized powder has a very large amount of extremely fine particles that readily convert completely to oxide. These particles, which are less than 1 μ in diameter, occur in all commercial atomized material regardless of nominal size. Finally, we demonstrated that the tensile strength of SAP does not result from the oxide stabilizing a cold-worked structure in aluminum to high temperatures. On the contrary, SAP never possess a cold-worked structure, even the flake coming directly from the mill. The powders always have a highly recovered or recrystallized structure and a very low dislocation density.

[redacted]

PART II

REACTOR CHEMISTRY DIVISION

[redacted]

7. FISSION-GAS RELEASE AND PHYSICAL PROPERTIES OF FUEL MATERIALS DURING IRRADIATION

R. M. Carroll
J. G. Morgan
R. B. Perez[1]
O. Sisman

We are studying the response of fission gas from UO_2 during irradiation in an effort to determine the fundamental mechanism by which the gas migrates and escapes from the fuel. To accomplish this we irradiate carefully selected and characterized specimens in an irradiation facility where the neutron flux and temperature are controlled independently. Fission gas is entrained in a constantly moving stream of sweep gas and carried outside the reactor where it is analyzed by gamma-ray spectrometry.

Based on these studies, we believe that the fission gas is released by a combination trapping and diffusion process in which the trapping is the dominant factor determining the time required for the gas to escape.[2,3] We have formed a defect-trap theory which postulates that defects in the UO_2 structure will trap migrating xenon and krypton atoms.[4] Some defects are naturally present in the UO_2, and others can be formed by irradiation. The irradiation-formed defects start as point defects, which can vanish by annealing but may cluster to form larger defects that will require longer times to anneal.

The mathematical formulation of the defect-trap theory required values of parameters that could not be obtained by steady-state testing methods. Therefore, we are using a dynamic testing method wherein

---

[1]Consultant from the University of Florida.

[2]R. M. Carroll and O. Sisman, Fuels and Materials Development Program Quart. Progr. Rept. June 30, 1965, ORNL-TM-1200, pp. 55–64.

[3]R. M. Carroll, O. Sisman, and R. B. Perez, Fuels and Materials Development Program Quart. Progr. Rept. Sept. 30, 1965, ORNL-TM-1270, pp. 49–59.

[4]R. M. Carroll and O. Sisman, "In-Pile Fission-Gas Release from Single-Crystal UO_2," Nucl. Sci. Eng. 21, 147–58 (1965).

the fission rate or temperature of the UO_2 specimen is oscillated about a selected value.[5] In essence, a slight ripple is imposed upon a steady-state condition and the response of the specimen to the ripple is analyzed by use of perturbation theory.

During this reporting period we have been correlating data and obtaining new parameters necessary for the analysis of data already obtained. The computer programs that had made successful pilot runs did not give good results for the production runs, and new computer programs were necessary before the correct analysis of the data was obtained. We have determined that two correction factors were needed; a correction for the influence of the thermocouple on the measured temperature response of the specimen and a correction for diffusion of fission gas within the sweep gas during the time the gas was moving outside the reactor. An attempt to measure the effect of electrical fields on fission-gas migration was inconclusive but some mysterious and unexpected feedback results occurred that certainly are worth pursuing further.

The oscillation method of testing requires an elaborate irradiation facility supported by precision instrumentation to produce the controlled perturbations. The mass of data resulting from the perturbations requires that the data be taken in a punch tape format and processed by computer techniques. The same equipment can also be used for physical property measurements and a hollow cylinder of UO_2 single crystal is now being irradiated to measure thermal properties and fission-gas release. The specimen and the oscillation methods of thermal conductivity were described previously.[6]

Response of UO_2 to Electrical Potentials

We have speculated that some proportion of the fission gas contained within the specimen was in an ionic state. Also, it is possible that

---

[5]R. M. Carroll and O. Sisman, Fuels and Materials Development Program Quart. Progr. Rept. Dec. 31, 1965, ORNL-TM-1400.

[6]R. M. Carroll, J. G. Morgan, and O. Sisman, Fuels and Materials Development Program Quart. Progr. Rept. Mar. 31, 1966, ORNL-TM-1500, pp. 61–68.

the passage of fission fragments and the decay of fission products could create electrical potentials in the UO_2 specimen which could act as driving forces for the fission-gas release. The simplest way to answer this question was to apply an external electrical potential and see if this affected the fission-gas release.

To this end, one of the three central thermocouples in the axis of the UO_2 single-crystal cylinder was used as an electrode (see Fig. 7.1). The other cylinder was the rhenium foil reflector surrounding the specimen. Neither of these electrodes were grounded although either may have been touching the UO_2 specimen which was also isolated from electrical ground. A ripple-free direct-current power supply was used to generate the potential field across the specimen. It should be noted that the lead wires to the electrode are in the same channel with the thermocouples; therefore, it is necessary to use direct-current voltages to avoid alternating-current pickup by the thermocouples. The voltage supply and the same arrangement of thermocouples had previously been used to power a small resistance heater located in the capsule and,

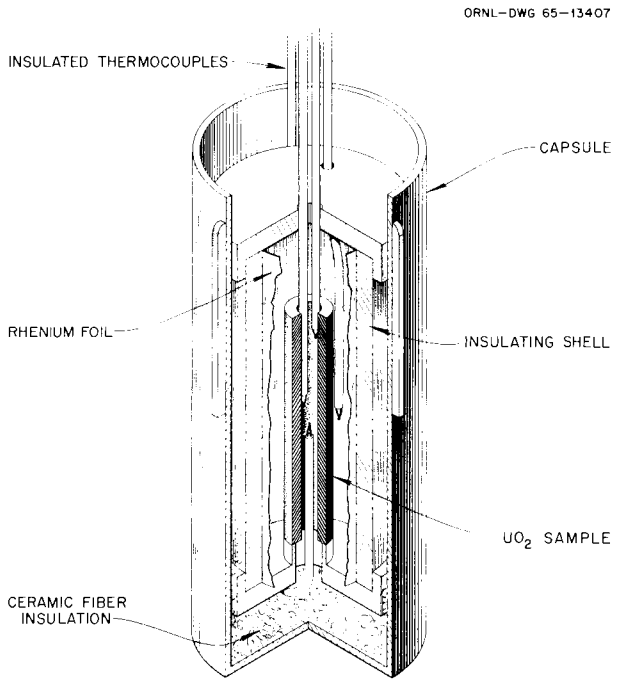

Fig. 7.1. Schematic of Capsule for Thermal Conductivity Experiments.

since no trouble had occurred then, we did not anticipate any thermocouple problems for the potential field experiment.

When a 5-v potential was placed across the fuel, the other two central thermocouples (see Fig. 7.1) immediately registered an emf great enough to drive the recorders off-scale. Since these thermocouples were connected to the reactor safety system, this resulted in a reactor setback. Our immediate reaction was to reduce the voltage of the power supply. However, this did not entirely remove the induced emf on the recorders, and we disconnected the power supply. During the disconnection, the wires leading to the specimen electrodes were accidentally shorted and again the recorders were driven full-scale, resulting in another reactor setback. However, in this case the electrical field had been generated solely by the UO_2 specimen. These results were so interesting that the reactor safety system was temporarily disconnected (under stringent supervision) and a series of in-reactor and bench tests were conducted leading to the following observations.

1. A simple potential applied at the tip of a thermocouple will not be detected. A thermocouple attached to a sensitive recorder can be placed within a charged capacitor or touched to battery terminals without affecting the recorder.

2. A current passing through the thermocouple junction will produce large emf variations.

3. No emf could be detected between the electrodes at the beginning of the test. However, when a voltage was applied to the specimen an emf was induced that remained even when the inducing voltage was removed. In this respect the specimen behaved like a capacitor.

4. When the specimen was charged and the electrode leads shorted to each other and to ground, a current would flow for several hours; the current and driving voltage gradually decreased. A 10-v potential for 30 sec could produce a detectable voltage and current for about 18 hr. When the shorted lead wires were opened, the voltage would increase momentarily much like a battery recovering from a current drain.

From these observations we formed a tentative working hypothesis.

1. When a voltage is applied across the fuel, charges that are present are redistributed. The charge movements produce the emf variations.

2. The UO_2 specimen behaves like a combination mushy capacitor and semiconductor, allowing charges to trickle out over a length of time.

There are a great many unanswered questions concerning the electrical response. Why is an external field necessary to start this operation? At the initial temperature of this test (1365°C) the electrical resistivity of UO_2 is very low. How then can a capacitive effect exist? If the electrodes are collecting charges from ionized gas, then the UO_2 charge should be neutralized rather quickly. We plan to return to this problem and to the effects of the electrical potential on fission-gas release after some of the safety instrument problems have been worked out.

Gas-Mixing Experiment

When fission gas emerges from the UO_2 specimen it is entrained in a constantly moving stream of sweep gas and carried outside the reactor where a continuous gamma-ray analysis is made. Naturally, the fission gas will become mixed into the sweep gas during this movement. The mixing is of little importance during steady-state operation, but during oscillations the resulting fission-gas waves may be altered by the mixing. For example, a high amplitude, square-edged, fission-gas wave lasting only 20 sec may diffuse within the sweep gas until when it is measured it appears to have a near Gaussian distribution of low amplitude lasting perhaps 300 sec.

In the analysis of fission-gas waves it is now apparent that we must know the amount of mixing that occurs so that we can determine the wave train as emitted from the specimen by applying the appropriate corrections to the measured fission-gas release. It is also obvious that the amount of mixing is influenced by the size and shape of the sweep-gas system and by the flow rate of the sweep gas.

Mixing Transfer Function

The fission-gas concentration $C(i\omega,L)$ measured at the detecting station will be given by

$$C(i\omega,L) = H_M(i\omega,L)\ R_T(i\omega) \quad , \tag{1}$$

where

L = the length of the piping,
$H_M(i\omega,L)$ = the mixing transfer function,
$R_T(i\omega)$ = the fission-gas release rate at the sample.

Hence from Eq. (1) the release rate corrected for mixing is

$$R_T(i\omega) = [H_M(i\omega,L)]^{-1}\ C(i\omega,L) \tag{2}$$

in terms of the actually measured fission-gas rate.

The main features of the mixing phenomenon can be understood by the following mathematical model which is the time-dependent version of a "mixing" theory derived by Prados and Scott.[7] The material balance inside the test chamber is

$$\frac{d}{dt} = C_o(t) + (\omega_c + i\omega)\ C_o(t) = R_T(t) \quad , \tag{3}$$

where

ω = frequency of oscillation (radians/sec),
ω_c = characteristic frequency = $\lambda + Q/V_c$ (radians/sec)
$C_o(t)$ = concentration of the fission product in the test chamber (moles/cm^3),

[7] J. W. Prados and J. L. Scott, Models for Fission-Gas Release from Coated Fuel Particles, ORNL-3421 (June 1963).

λ = decay constant (sec^{-1}),

Q = rate of flow of the sweep gas (cm^3/sec),

V_c = test chamber volume,

$R_T(t)$ = release rate of the fission gas at the specimen (moles/sec).

Fourier transformation of Eq. (3) yields, after some straightforward manipulations,

$$C_o(i\omega) = \frac{R_T(i\omega)}{\left(\frac{V_c}{\omega_c}\right)\left(1 + i\,\frac{\omega}{\omega_c}\right)} \quad , \tag{4}$$

where $R_T(i\omega)$ is the Fourier transform of the release rate. Following the Prados and Scott theory, the fission-gas concentration at any point $\underline{z}$ along the piping, $C(z,t)$ is given by

$$\frac{\partial}{\partial t} C(z,t) + \lambda\, C(z,t) = -U\, \frac{\partial}{\partial z} C(z,t) \quad , \tag{5}$$

with the boundary condition

$$C(o,t) = C_o(t) \quad , \tag{6}$$

and U = linear gas velocity in piping (cm/sec).

Again Fourier transformation of the pair of Eqs. (5) and (6) yields

$$C(i\omega,z) = \frac{R_T(i\omega)}{\left(\frac{V_c}{\omega}\right)\left(1 + \frac{i\omega}{\omega_c}\right)}\, e^{-\left(\frac{\lambda+i\omega}{U}\right)z} \quad , \tag{7}$$

where, as expected, Eq. (7) reduces to the result by Prados and Scott at zero frequency. Defining the mixing transfer function as the ratio of the fission-gas output at a given point z to the release rate at the sample one obtains

$$H_M(i\omega,z) \equiv \frac{C(i\omega,z)}{R_T(i\omega)} = \frac{1}{\left(\frac{V_c}{\omega_c}\right)\left(1+\frac{i\omega}{\omega_c}\right)} e^{-\left(\frac{\lambda+i\omega}{U}\right)z} \quad . \tag{8}$$

From Eq. (8) the amplitude $H_M(\omega,z)$ and phase $\textcircled{M}(\omega,z)$ of the mixing transfer function are given respectively by

$$\left|H_M(\omega,z)\right| = \frac{1}{\left(\frac{V_c}{\omega_c}\right)\left[1+\left(\frac{\tau}{\omega_c}\right)^2\right]} e^{-\frac{\lambda}{U}z} \tag{9}$$

and

$$\textcircled{M}(\omega,z) = -\omega\left(\frac{z}{U}+\frac{1}{\omega_c}\right) . \tag{10}$$

The amplitude ratio of two points in the piping (z,z_2) is independent of the frequency ω. The phase shift between those points is given after Eq. (10) as

$$\Delta\textcircled{M}(\omega,z) = \omega\tau_d \quad , \tag{11}$$

where the delay time is

$$\tau_d = \frac{Z_2 - Z_1}{U} \quad . \tag{12}$$

Experimental Method

To measure the mixing-transfer function we constructed a bench test that duplicated the in-reactor portion of the sweep-gas system. Argon was used to simulate the fission gas and a surge of argon was injected into the capsule at the specimen position. The concentration of argon in the helium sweep gas was measured by a thermal-conductivity gas-chromatographic apparatus that expressed the argon concentration as a voltage. The argon was injected as a single surge and the shape of this wave was measured just downstream of the injection point and measured again after it had passed through the entire system.

The voltage expressing the argon concentration was recorded on punch tape readout by a digital clock-voltmeter. Both the original wave and the resultant wave (expressed as wave 1 and wave 2) were recorded. Figure 7.2 is an example of the data. These measurements were made for a variety of sweep-gas flow rates.

A numerical Fourier analysis of the data will be performed to obtain the amplitude and phase shift of the mixing transfer function in the range of frequencies utilized in the fission-gas release experiment.

Preliminary analyses of the data (Fig. 7.3) show that the mixing factor, defined as the length of time an instantaneous pulse of fission gas could be detected after passing through the C-1 experiment, is indeed inversely proportional to the linear gas flow as expected from both intuition and Eq. (12). An inspection of the results from Eqs. (9) and (10) reveals that in order to minimize the mixing effect the flow system has to exhibit high characterictic frequencies, ω_c, and linear flow velocities. However, a compromise must be reached, as too high flow velocities will produce turbulent mixing and carry short-lived isotopes to the detecting station, complicating the counting procedure.

In the preceding model the radial distribution of flow velocities was not accounted for. This feature which arises from the laminar

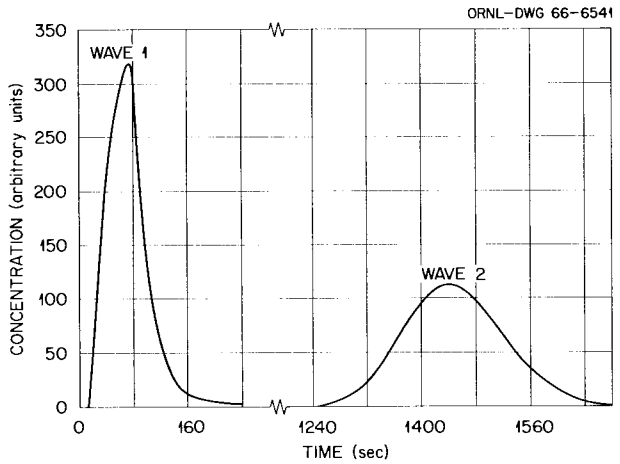

Fig. 7.2. Typical Voltage Waves Resulting from Mixing Argon in Helium Sweep Gas. Flow rate, 1.114 cm^2/sec.

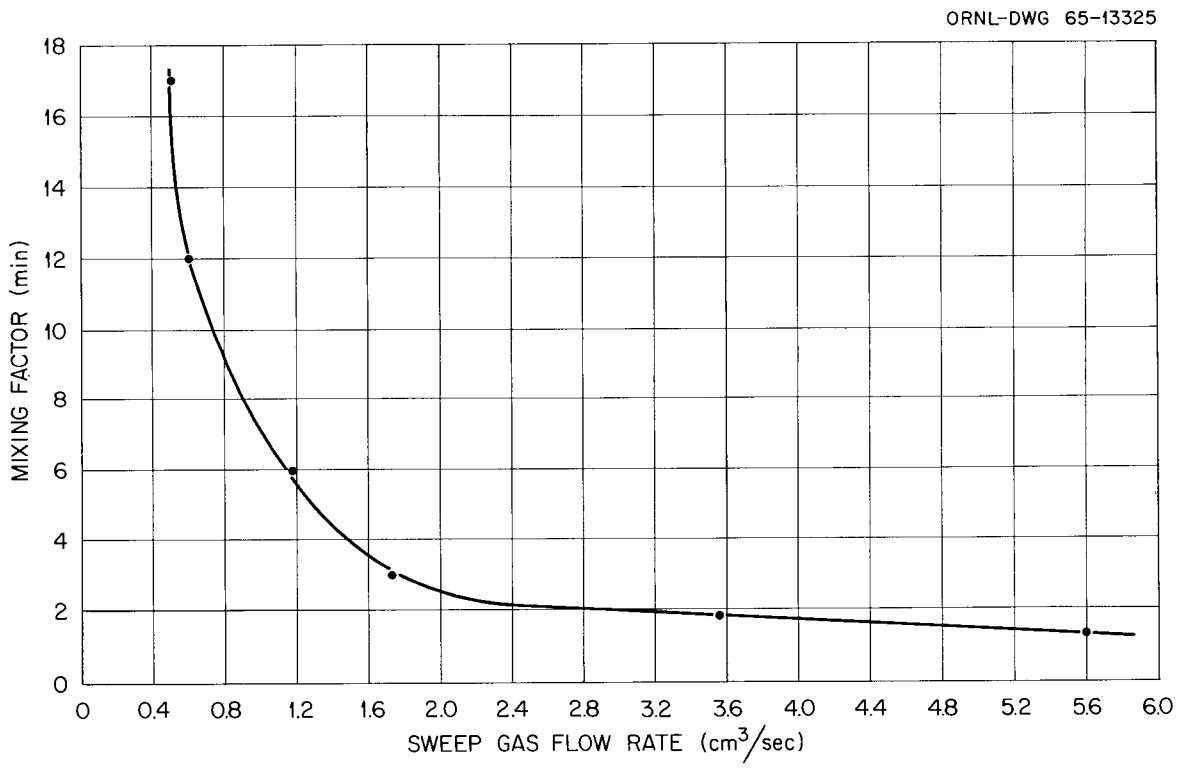

Fig. 7.3. Mixing Factor in C-1 Experiment as a Function of Sweep-Gas Flow Rate.

flow characteristics of the present experimental setup, highly complicates the analysis.[7] However, at the present stage of development our goal is to obtain the suitable empirical correction factors[8] and general information, as the one described above, to optimize the measuring system.

Thermal Conductivity by Oscillation Techniques

The principle of the oscillation technique for measuring thermal conductivity is that when the production of heat in the specimen is changed there is a time delay before the specimen temperature changes. This time delay is a function of the thermal diffusivity of the specimen. A major advantage of the oscillation method is that only the central temperature measurement of the specimen is required.[9]

The heat production of the UO_2 single-crystal specimen (see Fig. 7.1) is oscillated by moving the specimen capsule in a sinusoidal motion in the reactor neutron flux. The fission rate, and thus the heat production within the specimen, responds instantaneously to the change of neutron flux; however, the temperature does not (see Fig. 7.4). If the oscillations are so rapid that the temperature does not have a chance to reach its maximum value, then the amplitude of the temperature oscillations will decrease as the oscillation frequency increases (see Fig. 7.5). The time delay or phase shift between the neutron flux oscillations and the resultant temperature oscillations (see Fig. 7.4) will also change with frequency. The phase shift and amplitude relation of the temperature oscillations of the specimen in comparison to the neutron flux oscillations at various frequencies will both yield data to evaluate the thermal diffusivity of the specimen.

---

[8]There is a difference between the bench test and the actual measurement, in that in the former the gas is not radioactive, hence $\lambda = 0$. However, this turns out to be unimportant as in our case the relations $\lambda/u \ll 1$ and $\lambda \ll \frac{Q}{V_c}$ are satisfied.

[9]R. M. Carroll, J. G. Morgan, and O. Sisman, Fuels and Materials Development Program Quart. Progr. Rept. Mar. 31, 1966, ORNL-TM-1500, pp. 61–68.

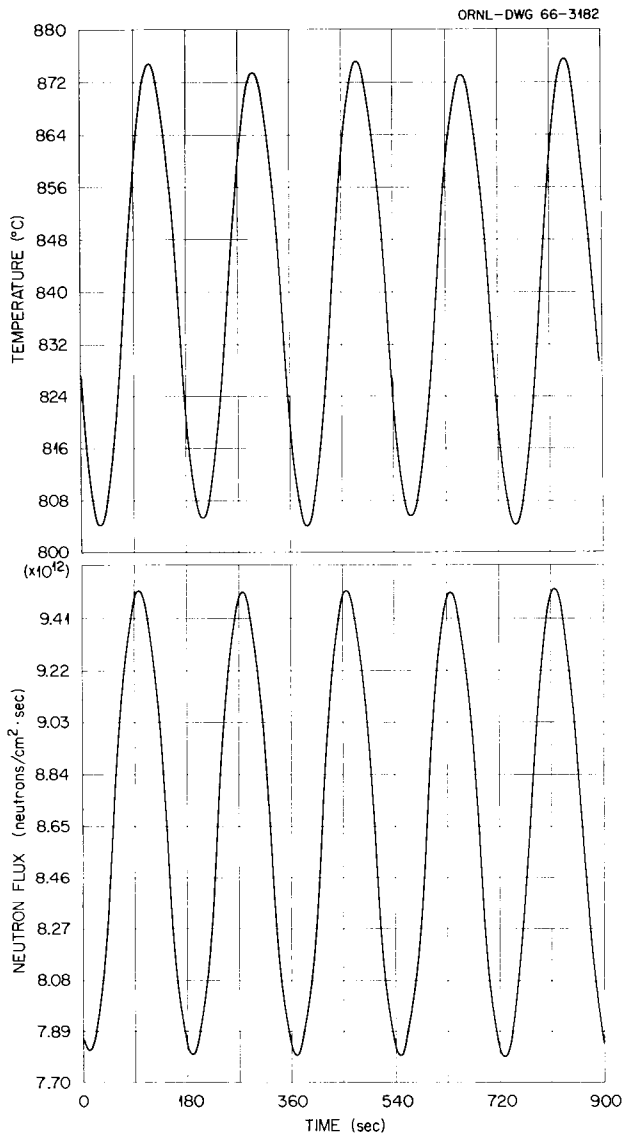

Fig. 7.4. Thermal Conductivity of a UO_2 Single-Crystal Specimen.

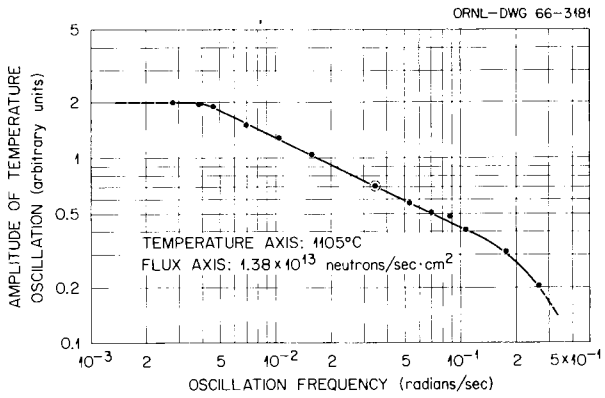

Fig. 7.5. Uranium Dioxide Single-Crystal Temperature Response to Oscillating Fission Rate.

General Theory

A theoretical model has been established under the following assumptions:

(a) The thermal conductivity of the sample does not change when irradiation level and temperature are oscillated slightly about a given level.

(b) End effects are negligible (infinite cylinder approximation).

(c) The heat carried away by the sweeping gas is negligible.

(d) Heat losses by radiation are negligible compared to heat transport by conduction through the helium gap to the walls of the shell.

(e) The heat generation within the sample is spatially uniform.

The hypothesis (a) is invalid in general. However, for small flux and temperature variations about average levels, the thermal conductivity will be mainly a function of the steady-state components of the variables.

In regard to (b) the assumption is valid at the center of the sample and can be checked by performing experiments at various positions in the sample.

Hypotheses (c) and (d) are based on the low heat capacity and high thermal conductivity of the helium gas.

After several standard manipulations of the heat diffusion equations and their associated boundary conditions, one obtains the following expression for the thermal conductivity transfer function at the center of the sample:

$$H_u(i\omega) \equiv \frac{T(i\omega)}{\phi(i\omega)} = H_s(i\omega) + H_u^{\circ}(i\omega) + P_o\left(\frac{1}{1 - i\,\frac{\omega}{\omega_c}}\right) H_s(i\omega) , \qquad (13)$$

where

ω = angular frequency (radians/sec),

$T(i\omega)$ = oscillatory component of the sample temperature (°C),

$\phi(i\omega)$ = oscillatory component of the flux (neutrons cm^{-2} sec^{-1}),

$T_s(i\omega)$ = oscillatory component of the shell temperature (°C),

$H_s(i\omega) = T_s(i\omega)/\phi(i\omega)$ shell temperature transfer function (cm^2 sec °C $neutron^{-1}$),

k = thermal diffusivity (cm^2/sec),

ω_c = characteristic frequency = $\alpha^2 k$ (radians/sec),

and

$$P_o = \frac{2}{(\alpha a)\, J_1(\alpha a)\omega_c} \text{ (seconds)} , \qquad (14)$$

$$H_u^{\circ}(i\omega) = \frac{H_o}{1 - i\,\frac{\omega}{\omega_c}} , \qquad (15)$$

with

$$H_o = P_o\eta \ (cm^2 \text{ sec °C } neutron^{-1}) , \qquad (16)$$

where

$\eta = q\,\Sigma_f/\rho c$ (°C cm^2 $neutron^{-1}$) ,

$q = \frac{cal}{fission}$,

Σ_f = macroscopic fission cross section (fission $neutron^{-1}$ sec^{-1}),

ρ = sample density (g/cm^3),

c = heat capacity (cal $g^{-1}°C^{-1}$),

a = radius of the sample (cm).

The constant α is the lowest root of the transcendental equation

$$\alpha \frac{d}{dr} J_o(\alpha r)\Big|_{r = a} + \frac{C}{K} J_o(\alpha a) = 0 \quad , \tag{17}$$

where

C = conductance of the helium gap (cal cm^{-2} sec^{-1} $°C^{-1}$),

K = thermal conductivity of the sample (cal cm^{-1} sec^{-1} $°C^{-1}$).

Although an analytical expression of the shell temperature transfer function, $H_s(i\omega)$, can be obtained, we have followed the procedure of actually measuring it and introducing this information as a correction factor in Eq. (13). After some straightforward algebra the following results are obtained for the amplitude $[H_u(\omega)]$ and phase shift $\psi_u(\omega)$ of the measured thermal conductivity transfer function

$$|H_u(\omega)| = |H_s(\omega)|\cos(\psi_u - \rho_s)$$

$$+ \left\{ |H_u^{\,o}(\omega)|^2 - |H_s(\omega)|^2 \left[\frac{(P_o\omega)^2}{1 + (\frac{\omega}{\omega_c})^2} + \frac{\tan^2(\psi_u - \rho_s)}{1 + \tan^2(\psi_u - \rho_s)} \right] \right\}^{\frac{1}{2}} , \tag{18}$$

$$\tan[\psi_u(\omega)] = \left\{ \tan \rho_o + P_o\omega \left[\frac{|H_s(\omega)|}{|H_u^{\,o}(\omega)|} \right] \cos(\rho_o + \rho_s) \right\} \left[\frac{1 - \frac{|H_s(\omega)|}{|H_u^{\,o}(\omega)|} \frac{\cos \rho_s}{\cos \psi_u}}{1 - P_o\omega \frac{|H_s(\omega)|}{|H_u^{\,o}(\omega)|} \sin(\rho_o + \rho_s)} \right] \tag{19}$$

where

$$\rho_o = \tan^{-1}\left[\frac{\text{Imaginary } H_u^{\,o}(\omega)}{\text{Real } H_u^{\,o}(\omega)}\right] - \tan^{-1}\left(\frac{\omega}{\omega_c}\right) \tag{20}$$

$$\rho_s = \tan^{-1}\left[\frac{\text{Imaginary } H_s(\omega)}{\text{Real } H_s(\omega)}\right] . \tag{21}$$

It is indeed fortunate that the complicated corrections appearing in Eqs. (18) and (19) turn out to be of a very small magnitude. Inspection of the above result shows that in the low frequency limit the amplitude is well represented by

$$[H_u(\omega)]_o \cong H_s(\omega) + |H_u^{\,o}(\omega)|; \quad [\cos(\psi_u - \rho_s) \cong 1] . \tag{22}$$

This results from the fact that for $\omega \ll 1$ the terms containing $(P_o\omega)^2$ and $\tan^2(\psi_u - \psi_s)$ are vanishingly small. On the other hand for large frequencies $H_s(\omega)$ and $[1 + (\frac{\omega}{\omega_c})^2]$ decrease very fast with frequency. Hence the amplitude of $[H_u(i\omega)]$ for large frequencies is given by

$$|H_u(\omega)|_\infty = |H_u^{\,o}(\omega)| . \tag{23}$$

A similar reasoning yields the following low-frequency limit for the phase shift $\psi_u(\omega)$

$$\tan[\psi_u(\omega)]_o = \tan\rho_o\left[1 - \frac{|H_s(\omega)|}{|H_u^{\,o}(\omega)|}\right] . \tag{24}$$

For high frequencies the behavior of the relation (19) is still complicated and it does not lend itself to any simplified expression.

Analysis of the Data

At the time this report is written the shell transfer function corrections for the phase shift [Eq. (19)] have not yet been performed. Hence we presently shall limit our discussion to the amplitude data.

The gain $G(\omega)$ defined as

$$G(\omega) = 20 \log|H_u(\omega)| \quad \text{decibels} \tag{25}$$

was first corrected for the shell transfer function effects. The correction terms (in decibels) are shown in Table 7.1 as a function of frequency. Next a correction for the thermocouple transfer function was performed.[10] The corrected gain was plotted vs log ω in Fig. 7.6.

[10] "Thermocouples Transfer Function," p. 94 this report.

Table 7.1. Shell Transfer Function Correction

ω (radians/sec)	Δ (dc) (correction in decibels)
5.24×10^{-3}	7.1
1.05×10^{-2}	6.9
1.57×10^{-2}	5.8
2.62×10^{-2}	3.7
3.49×10^{-2}	3.6
5.24×10^{-2}	2.7
1.75×10^{-1}	1.1
2.62×10^{-1}	1.0

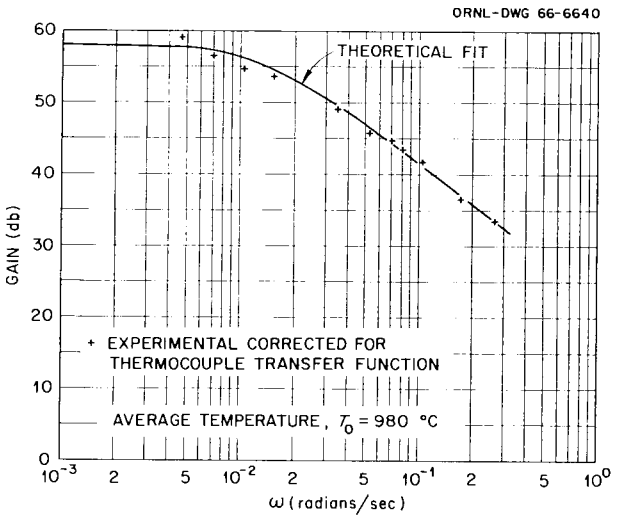

Fig. 7.6. Thermal Conductivity Transfer Function; Amplitude.

After these various corrections have been performed the experimentally determined gain $G(\omega)$ should be described [Eqs. (22) and (23)] by

$$G(\omega) = 20 \log|H_u^{\circ}(\omega)| = 20 \log H_o - 10 \log\left[1 + \left(\frac{\omega}{\omega_c}\right)^2\right] \qquad (26)$$

At very small frequencies $G(\omega)$ is a constant equal to 20 log H_o. For big frequencies $\omega/\omega_c > 1$, one obtains the asymptotic behavior

$$G_\infty(\omega) = -20 \log \frac{\omega}{\omega_c} = 20 \log \omega_c - 20 \log \omega \quad ; \qquad (27)$$

hence $G_\infty(\omega)$ is a linear function of log ω with a slope of 20 20 db/decade. The intersection of the asymptote at zero frequencies and the 20 db/decade asymptote provides a good estimation of the characteristic frequency ω_c. The intersect at zero frequency provides the magnitude 20 log H_o. From these estimates after several easily performed iterations, the experimental data were fit to a function

$$G(\omega) = 58 - 10 \log\left(1 + \frac{\omega}{1.5}\, 10^2\right) \quad \text{(theoretical)} \quad , \qquad (28)$$

where we took

$$20 \log H_o = 58$$

$$\omega_c = 1.5 \times 10^{-2} \text{ (radians/second)} .$$

The theoretical fit we obtained is shown in Fig. 7.6, the line being the theoretical fit to the indicated data points. Good agreement was obtained specially in the high frequency tail of the curve.

Procedure for the Computation of the Thermal Diffusivity, k

The thermal diffusivity k is obtained from the knowledge of the characteristic frequency, ω_c, that is,

$$k = \frac{\omega_c}{\alpha^2} \qquad (cm^2 \text{ sec}^{-1}) . \tag{29}$$

The value of α^2 could be computed from the transcendental Eq. (17); however, this will involve the knowledge of the gap conductance C and iterations of the yet unknown thermal conductivity of the sample. Alternatively, it is much more convenient and accurate to use Eq. (14), rewritten in the form

$$(\alpha a)\, J_1(\alpha a) = \frac{2}{P_o \omega_c} \qquad \text{(dimensionless)} , \tag{30}$$

a transcendental equation which only demands the determination of the zero frequency intersect and the characteristic frequency; both of which are obtained from the transfer amplitude plots.

Preliminary calculations have yielded values of the thermal conductivity, K = (pck) in agreement with various sources of information. However, the final evaluation of the results awaits several reproducibility tests and runs at various flux and temperature levels.

The oscillatory technique presents at least two definite advantages over static methods:

(a) Only one bulk temperature has to be measured accurately.

(b) The method is independent to a large extent of the detailed knowledge of the boundary conditions [Eq. (17)].

At this stage of the work the feasibility of the oscillatory method has been proven. Future work will involve refined measurements under various experimental conditions to determine the thermal conductivity as a function of temperature and irradiation.

Thermocouple Transfer Function

When the UO_2 specimen is oscillated in the neutron flux the temperature response is influenced by the thermal conductivity and specific heat of the specimen. The measured temperature response is also affected by the thermal conductivity and specific heat of the thermocouple used to monitor the temperature. It is therefore necessary to measure the temperature response of the thermocouple and subtract this from the temperature response of the fuel thermocouple combination.

A bench test apparatus was constructed in which a thermocouple was oscillated along the axis of a tube furnace. The length of the thermocouple movement can be adjusted and the frequency of the oscillation can be varied. Since there is a temperature gradient along the axis of the tube furnace and the thermocouple was moved from one temperature zone to another, the temperature response of the in-reactor experiment could be duplicated as to span and axis of temperature oscillation. We assume that the thermocouple movement did not affect the temperature of the tube furnace.

The temperature and movements of the thermocouple were recorded as a function of time, using the same data recording apparatus used in the in-reactor studies. The punched tape data were processed in the same manner as the thermal conductivity data. Analysis of the thermocouple response showed that for oscillation periods longer than 3 min the thermal lag of the thermocouples may be neglected. For

oscillation periods shorter than 3 min the thermocouples did not have time to reach the temperature of the furnace zone and the temperature oscillations were out of phase with the physical motion oscillations. A typical set of these results is shown in Fig. 7.7. This result explains why the amplitude vs frequency curve shown in Fig. 7.5 deviates from a straight line at the higher frequencies. When the bench test data are fully evaluated, they will be used to correct the high frequency response of the UO_2 specimen.

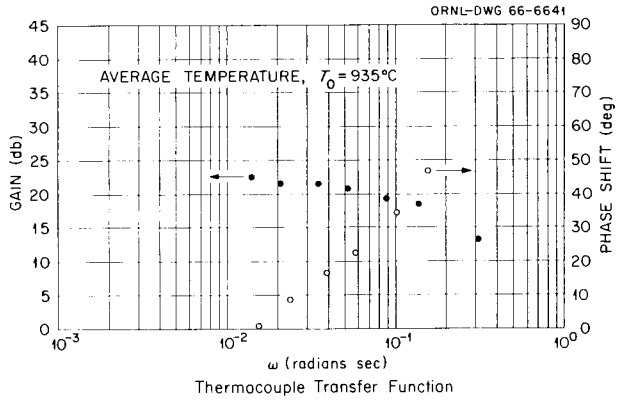

Fig. 7.7. Thermocouple Transfer Function.

Previous reports in this series are:

ORNL-TM-920	Period Ending June 30, 1964
ORNL-TM-960	Period Ending September 30, 1964
ORNL-TM-1000	Period Ending December 31, 1964
ORNL-TM-1100	Period Ending March 31, 1965
ORNL-TM-1200	Period Ending June 30, 1965
ORNL-TM-1270	Period Ending September 30, 1965
ORNL-TM-1400	Period Ending December 31, 1965
ORNL-TM-1500	Period Ending March 31, 1966

INTERNAL DISTRIBUTION

1–3. Central Research Library
4–5. ORNL – Y-12 Technical Library Document Reference Section
6–15. Laboratory Records
16. Laboratory Records, RC
17. ORNL Patent Office
18. G. M. Adamson, Jr.
19. J. C. Banter
20. J. H. Barrett
21. S. E. Beall
22. R. J. Beaver
23. M. Bender
24. R. G. Berggren
25. J. O. Betterton, Jr.
26. D. S. Billington
27. A. L. Boch
28. B. S. Borie
29. G. E. Boyd
30. W. H. Bridges
31. R. B. Briggs
32. W. E. Brundage
33. R. M. Carroll
34. J. V. Cathcart
35. G. W. Clark
36. K. V. Cook
37. J. H. Crawford
38. J. E. Cunningham
39. J. H. DeVan
40. C. V. Dodd
41. J. I. Federer
42. B. E. Foster
43. A. P. Fraas
44. J. H Frye, Jr.
45. R. J. Gray
46. W. R. Grimes
47. H. D. Guberman
48. J. P. Hammond
49. W. O. Harms
50. R. L. Heestand
51–52. M. R. Hill
53. N. E. Hinkle
54. D. O. Hobson
55. H. W. Hoffman
56. H. Inouye
57. T. N. Jones
58. G. W. Keilholtz
59. B. C. Kelley
60. J. A. Lane
61. A. P. Litman
62. A. L. Lotts
63. R. N. Lyon
64. H. G. MacPherson
65. R. E. MacPherson
66. M. M. Martin
67. W. R. Martin
68. R. W. McClung
69. H. E. McCoy, Jr.
70. H. C. McCurdy
71. R. E. McDonald
72. D. L. McElroy
73. C. J. McHargue
74. F. R. McQuilkin
75. A. J. Miller
76. E. C. Miller
77. J. G. Morgan
78. F. H. Neill
79. S. M. Ohr
80. P. Patriarca
81. F. H. Patterson
82. A. M. Perry
83. S. Peterson
84. M. L. Picklesimer
85. R. E. Reed
86. P. L. Rittenhouse
87. W. C. Robinson
88. M. W. Rosenthal
89. G. Samuels
90. A. W. Savolainen
91. J. L. Scott
92. O. Sisman
93. G. M. Slaughter
94. G. P. Smith, Jr.
95. N. K. Smith
96. S. D. Snyder
97. I. Spiewak
98. J. T. Stanley
99. W. J. Stelzman
100. J. O. Stiegler
101. D. B. Trauger
102. R. P. Tucker
103. J. T. Venard
104. G. M. Watson
105. M. S. Wechsler
106. A. M. Weinberg
107. J. R. Weir, Jr.
108. W. J. Werner
109. G. D. Whitman
110. J. M. Williams
111. R. O. Williams
112. J. C. Wilson

113. H. L. Yakel, Jr.
114. F. W. Young, Jr.
115. C. S. Yust

EXTERNAL DISTRIBUTION

116–119. F. W. Albaugh, Battelle, PNL
120. R. J. Allio, Westinghouse Atomic Power Division
121. R. D. Baker, Los Alamos Scientific Laboratory
122. L. Brewer, University of California, Berkeley
123. V. P. Calkins, GE, NMPO
124. W. Cashin, Knolls Atomic Power Laboratory
125. S. Christopher, Combustion Engineering, Inc.
126–127. D. F. Cope, AEC, Oak Ridge Operations
128. G. K. Dicker, Division of Reactor Development, AEC, Washington
129. E. A. Evans, GE, Vallecitos
130. W. C. Francis, Phillips Petroleum Company
131. R. G. Grove, Mound Laboratory
132. D. H. Gurinsky, BNL
133. A. N. Holden, GE, APED
134–136. J. S. Kane, University of California, Livermore
137. J. H. Kittel, ANL
138. E. J. Kreih, Westinghouse, Bettis Atomic Power Laboratory
139. W. L. Larsen, Iowa State University, Ames Laboratory
140. J. J. Lombardo, NASA, Lewis Research Center
141. J. H. MacMillan, Babcock and Wilcox Company
142. R. E. Pahler, Division of Reactor Development, AEC, Washington
143. S. Paprocki, BMI
144. D. Ragone, GA
145. Division of Research and Development, AEC, ORO
146. H. Kato, U.S. Department of the Interior, Bureau of Mines
147. R. Van Tyne, Illinois Institute of Technology Research Institute
148. F. C. Schwenk, Division of Reactor Development, AEC, Washington
149–150. J. M. Simmons, Division of Reactor Development, AEC, Washington
151. L. E. Steele, Naval Research Laboratory
152. R. H. Steele, Division of Reactor Development, AEC, Washington
153. W. F. Sheely, Division of Research, AEC, Washington
154. A. Strasser, United Nuclear Corporation
155. W. R. Voigt, Division of Reactor Development, AEC, Washington
156. C. E. Weber, Atomics International
157. G. W. Wensch, Division of Reactor Development, AEC, Washington
158. M. J. Whitman, Division of Reactor Development, AEC, Washington
159–173. Division of Technical Information Extension